**Joana Isabel Faustino Martins**

Bachelor of Science in Biomedical Engineering

# Brain Plasticity associated with Predictive Masking and Glaucoma

Dissertation submitted in partial fulfillment
of the requirements for the degree of

Master of Science in
**Biomedical Engineering**

Adviser: Frans W. Cornelissen, Professor, University Medical Center Groningen

Co-adviser: Ricardo Vigário, Auxiliar Professor, NOVA University of Lisbon

Examination Committee

Chairperson: Prof. Dr. Carla Maria Quintão Pereira
Raporteur: Prof. Dr. Maria João Gomes Trindade Caseiro
Member: Prof. Dr. Ricardo Nuno Pereira Verga e Afonso Vigário

FACULDADE DE CIÊNCIAS E TECNOLOGIA
UNIVERSIDADE NOVA DE LISBOA

**September, 2019**

**Brain Plasticity associated with Predictive Masking and Glaucoma**



This document was created using the (pdf)LaTeX processor, based in the "novathesis" template[1], developed at the Dep. Informática of FCT-NOVA [2].
[1] https://github.com/joaomlourenco/novathesis [2] http://www.di.fct.unl.pt

*Para os meus avós Hermínia e Francisco*

# Acknowledgements

First and foremost, I would like to thank the institution that was my second home during the last five years, FCT-NOVA. In particular to Prof. Dr. Carla Quintão, coordinator of the master in Biomedical Engineering, for the excellent work and devotion to raising teaching conditions, as well as giving response and voice to the students.

To my adviser Prof. Dr. Frans Cornelissen for the opportunity to have worked on such a fascinating project. Thank you for the trust, availability, motivation and appreciation to my work during our meetings.

To that person who was my cornerstone during this first introduction to the scientific research world, Joana Carvalho. Thank you for the contagious passion for science but most of all, for the long hours of work side by side, the moments of joy as well as those of greater frustration. You were an exceptional guide, and I think I am allowed to say that we made a good team. This thesis reflects everything you have taught me.

The work of scientific research is teamwork. In this sense, I would like to thank Azzurra Invernizzi for sharing your knowledge with me and believing in my potential. To my dear colleague Alessandro Grillini for his wise advice, not only academic but also personal. To Shereif Haykal, Rijul Soans, Hinke Halbertsma and Birte Gestefeld for the sympathy and welcoming me to the group.

To my co-adviser Prof. Dr. Ricardo Vigário for allowing me to pursued and develop my thesis project abroad.

My journey at FCT-NOVA started in a somewhat turbulent way. Life has taught me to always look to the bright side, even in the most unpleasant situations. Words will never be enough to thank all the support and affection I had received by the time when no one knew me well. To all my college friends, I am forever grateful that you made me feel that I belonged to something when I saw my world crumble. In particular, I would like to thank a group of people that I want to take with me outside the doors of this institution: Beatriz Costa, Ana Sousa, Ana Pinheiro, Joana Inácio, Inês Dias, João Narciso, Bruno Meireles, Sara Santos, Maria Inês Correia, Miguel Santos and João Tavares.

At last, to the four people in my life that I want to make the most proud of me. To my mother, for never letting me give up and always being there for me. To my father, who always supports my decisions even if they imply being physically away from him. To my aunt, my second mother, for striving to see me happy. And to my sister, my reference, for the friendship and for teaching me what it means to be a great woman.

# Abstract

Glaucoma is a disease resulting from damage at the optic nerve, the "highway" through which visual information travels from the retina towards the visual brain. Such lesion deprives the visual cortex of the regular input, causing interruptions within the visual field – scotoma. However, even when such lesions occur, perception remains stable as the human visual system perceptually masks the insult with the visual features of nearby regions of the visual field. To unravel the neural mechanisms by which this remarkable capacity occurs in glaucomatous individuals, we used functional magnetic resonance imaging (fMRI) and neural modelling to track changes in cortical population receptive fields (pRFs). We found that visual neurons from early visual areas (V1-3) expanded their pRFs both inside and at the vicinity of the lesion. V1 pRFs also shifted their preferred central position towards the outside of the scotoma. By doing so, neural populations were able to process information from spared visual field, consistent with the notion of predictive masking. In contrast, well-sighted observers did not show similar patterns of neural activity in response to the introduction of an artificial scotoma (AS). Our findings provide evidence of enduring cortical reorganization underlying the predictive spatial masking of scotomas in glaucoma, meeting the contemporary view that early visual areas of the adult human brain retain plastic mechanisms. Furthermore, the involvement of the brain suggests that glaucoma pathogenesis goes beyond the eye.

**Keywords:** glaucoma, masking, population receptive field, reorganization, fMRI

# Resumo

O Glaucoma resulta de uma lesão ao nível do nervo ótico, a "estrada" através da qual a informação visual viaja da retina em direção ao cérebro. Tal dano priva o córtex visual do input esperado o que, por sua vez, gera interrupções no campo visual – escotomas. No entanto, mesmo quando essas lesões ocorrem, a capacidade de percepção visual permanece estável uma vez que, o sistem visual humano tem a capacidade de mascarar a lacuna de informação com as características do campo visual circundante. De forma a desmistificar os mecanismos neuronais através dos quais esta capacidade notável ocorre em indíviduos diagnosticados com glaucoma, utilizou-se ressonância magnética functional (fMRI) e modelagem neuronal de forma a investigar alterações nas populações de campos receptivos corticais (pRFs). Observou-se que os neurónios visuais alocados nas áreas visuais primárias (V1-3) expandiram os seus pRFs tanto dentro, com nas proximidades do escotoma. Adicionalmente, os pRFs correspondentes à área V1 reconfiguraram sua posição espacial, deslocando o seu centro para o exterior da lesão. Desta forma, as populações neuronais foram capazes de processar informação de regiões intactas do campo visual, o que está de acordo com a noção de mascaramento preditivo. Em contraste, observadores com visão normal (ou corrigida para normal) não revelaram tais padrões de atividade neuronal aquando da visualização de um estímulo com um escotoma artificial sobreposto. Os resultados acima mencionados fornecem evidências de uma reorganização cortical duradoura subjacente ao mascaramento preditivo de escotomas na doença do glaucoma, atendendo à visão contemporânea de que as áreas visuais primárias do cérebro humano retêm plasticidade. Além disso, o envolvimento do cérebro sugere que a patogénese do glaucoma não se limita aos efeitos oculares.

**Palavras-chave:** glaucoma, mascaramento preditivo visual, campo receptivo populacional, reorganização cortical, fMRI

# Contents

# List of Figures

# List of Tables

# Acronyms

**AC** Anterior Commissure.

**AS** Artificial Scotoma.

**BOLD** Blood-oxygen-level-dependent.

**CSF** Cerebrospinal Fluid.

**DWI** Diffusion Weighted Imaging.

**EV** Explained Variance.

**FDT** Frequency Doubling Perimetry.

**FF** Full Field.

**fMRI** functional Magnetic Resonance Imaging.

**FOV** Field-of-view.

**GLM** General Linear Model.

**GM** Gray Matter.

**HFA** Humphrey Field Analiser.

**HRF** Hemodynamic Response Function.

**HTG** High-Tension Glaucoma.

**IOP** Intraocular Pressure.

**LCR** Luminance-contrast defined retinotopy.

**LGN** Lateral Geniculate Nucleus.

**LPZ** Lesion Projection Zone.

**LTI** Linear Time-Invariant.

**MCMC** Markov Chain Monte Carlo.

**MD** Mean Deviation.

**MP** Micro Probing.

**MR** Magnetic Resonance.

**MRI** Magnetic Resonance Imaging.

**NCDF** Normal Cumulative Distribution Function.

**NCT** Non-contact Tonometry.

**NTG** Normal-Tension Glaucoma.

**OCT** Optical Coherence Tomography.

**ON** Optic Nerve.

**ONH** Optic Nerve Head.

**PACG** Primary Angle-Closure Glaucoma.

**PC** Posterior Commissure.

**PM** Predictive Masking.

**POAG** Primary Open-Angle Glaucoma.

**pRF** Population Receptive Field.

**RF** Receptive Field.

**RGC** Retinal Ganglion Cell.

**RNFL** Retinal Nerve Fiber Layer.

**ROI** Region-of-interest.

**RPE** Retinal Pigment Epithelium.

**RSS** Residual Sum of Squares.

**SD** Standard Deviation.

**SNR** Signal-to-noise ratio.

**SPZ** Scotoma Projection Zone.

**TE** Echo Time.

**TR** Repetition Time.

**TWR** Traveling Wave Retinotopy.

**VA** Visual Acuity.

**VF** Visual Field.

**WM** White Matter.

Chapter 1

# Introduction

Glaucoma is one of the leading causes of blindness worldwide that is predicted to affect 112 million people by the year 2040 [1]. Described as a collection of neurodegenerative diseases, glaucoma is caused by an initial loss of retinal ganglion cells (RGCs) accompanied by the progressive damage of the optic nerve. This results in regions of deprived visual input - scotomas - within the visual field of the affected eye. Although glaucoma is traditionally considered an eye disease, there is increasing evidence that its neurodegenerative effects are not restricted to the retina and optic nerve, instead spreading along the entire length of the visual pathway towards the brain [2–5].

Even though glaucoma may cause irreversible blindness, it can be prevented if diagnosed early. Nevertheless, the disease frequently goes unnoticed as individuals with scotoma often do not realize that such damage exists until an objective ophthalmic test is performed. This is because predictive masking (PM), also referred to as filling-in, occurs at the scotoma whereby the visual cortex predicts and interpolates the missing visual features, such as color, brightness, texture, and motion, of the incomplete scene [6]. Despite its scientific and clinical relevance, the underlying neuronal mechanisms of PM are still ill-understood.

Previous studies that probe PM and examination of the neural impact of retinal lesions have shown that the brain reorganizes through re-scaling and displacement of the receptive fields towards spared regions of the visual field [7–10]. The receptive field (RF) of a visual neuron refers to the portion of the visual field that is most effective at driving the neuron's response. Estimating the RF of visual neurons is therefore of great importance in the investigation of how the visual brain responds to a damage in the visual system. Since recently, there is a debate about whether the 'ectopic' RFs - altered in position and/or size - should actually be interpreted as evidence of cortical reorganization because the same changes also occur following simulated (artificial) scotomas [11–13].

Hence the changes in the RFs will have an impact in the functional organization of the visual cortex. A common way to assess the correspondence between visually selective neurons and their RFs in visual space is to systematically stimulate certain parts of the visual field while monitoring the neuronal stimulus-evoked responses with functional magnetic resonance imaging (fMRI) [14–16]. This is called visual field mapping because due to the retinotopic organization of the visual cortex (i.e. nearby visual neurons respond to nearby locations in the visual field) it is possible to unravel a number of different visual field maps. Nowadays, with the urge of neurocomputational models, such as population receptive field (pRF) [17], it is possible to use visual field mapping data to estimate properties of the RFs of visual neurons which is useful when it comes to investigating cortical reorganization.

The plasticity (reorganization) of the visual cortex during PM has not been studied in particular. Adding to this, despite the large number of studies about cortical reorganization using fMRI visual field mapping methods, most of them have addressed central visual disorders. In glaucoma, visual field loss starts peripherally and so the mechanisms of spatial reorganization might be different from those where central vision degenerates, given that peripheral and central vision are distinctly processed in the cortex [18].

Based on the above statements, in the present study, we sought to determine the neuronal mechanism underlying the PM of scotomas in glaucoma. We hypothesize that there is a reorganization of the visual cortex, evident from an enlargement of the RFs surrounding the scotomas, and a shift towards the edges of the scotoma. To test our hypothesis, we used fMRI in combination with biologically inspired neural population receptive modeling (pRF) to track changes in RFs' properties of a glaucoma population. Moreover, we delineated visual field coverage maps from the pRF characteristics and based on a novel methodology to depict the visual field defects. We contrasted the results with those of healthy well-sighted controls in whom the lesions of the glaucoma visual system were mimicked through introduction of an artificial scotoma (AS) into their visual field.

## 1.1 Outline of the thesis

This thesis is organized in 11 chapters. The present one serves to reveal and explain the underlying research question, as what is hypothesized to be found and the means to address it.

In chapter 2 there is an overview of the human visual system, from the very beginning of visual processing in the eye to the complexity of the visual areas in the brain.

Chapter 3 includes a description of a standard visual field, as well the defects to the visual field arising from damage to the optic nerve in the case of the disease in focus – Glaucoma. A description of glaucoma pathophysiology is additionally presented.

Following the theme of chapter 3, in chapter 4 it is described the effects of visual field defects in the brain, including mechanisms of neuroplasticity and the perceptual

phenomenon of PM.

Chapter 5 reveals the principles of fMRI, in particular the haemodynamics that underly neuronal activity following stimulation. As this thesis revolves around evaluating visual field maps in the human brain, chapter 6 reveals a brief introduction of the technique used to do so by means of a combination of fMRI and visual stimulation: the pRF approach.

We also reviewed the literature on pRF changes in ophthalmic and neurologic diseases (chapter 7), to give an insight into the current state of pRF as a way to reveal cortical reorganization.

Chapter 8 includes the methods that were used to determine the organization of the visual cortex of the participants of the study. In chapter 9 and 10, the results are gathered together and discussed, respectively.

At last, chapter 11 presents the main findings and limitations of this study. Additionally, it includes some suggestions for future work and improvements.

A supplementary material chapter is presented at the end of the document which contains a group of results not shown in the main results chapter. The principles underlying Magnetic Resonance Imaging (MRI) as well as a resume about the General Linear Model (GLM) are included as annexes due to their relevance to the understanding of the methodology used in this thesis.

Chapter 2

# Human Visual System

Sight underlies the ability to understand the world and to navigate within the surrounding environment. As one looks around, the eyes are continually absorbing light rays that are essential to the visual process. The light travels deep into the eyeballs towards the back of each of them where its energy is transformed into electrical impulses. These impulses are carried on to the visual cortex, along neuronal pathways, where they are ultimately processed and unified into a single image.

The eye together with the conducting paths, that carry the visual information, and the visual receiving brain areas form a compact unit – the visual system.

## 2.1 The Eye

The eye consists of a complex sensory organ that plays a fundamental role in visual perception, one of the essential human senses.

Visual information enters the eye through the cornea, the transparent front "window" of the eye, that due to its curvature enables most of the eye's focusing power. The cornea is anteriorly nourished with oxygen by tears and posteriorly bathed by a clear liquid called aqueous humor, which sustains the shape of the eyeball [19].

The cornea's refractive power bends the light rays enabling them to freely pass through the pupil, a hole allocated in the center of the iris. The iris controls the pupil size by contracting and expanding, hence, defining the level of illumination onto the retina.

Once through the gate of the pupil, the visual information reaches the lens where the remainder focusing ability is provided helping the eye to see sharply both near and far, a phenomenon called *accommodation* [20]. The lens focuses the light through the vitreous humor, a gel-like substance that fills the space between the lens and the retina, forming an upside-down image which is projected onto the retina [19].

The retina is a complex nervous tissue that covers two-thirds of the back of the eyeball [19]. By converting the light signals into electrical impulses, the retina represents the starting-point of the visual pathways.

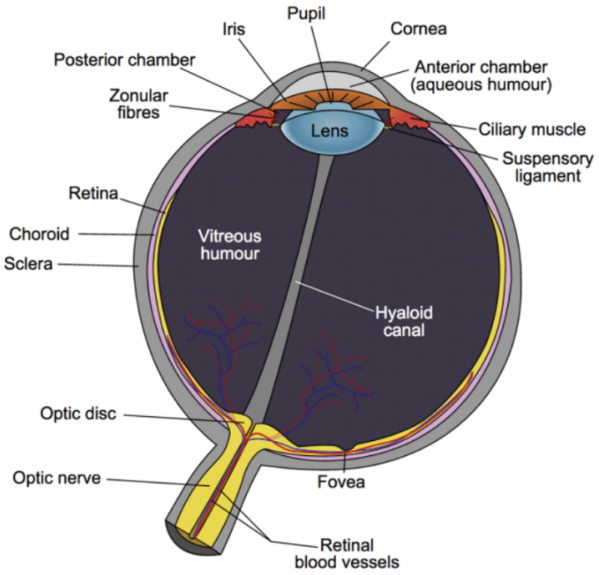


Figure 2.1: **Schematic anatomy of the eye.** Reprinted from [21].

## 2.2 Neuronal Pathways

The visual processing starts in the retina. Anatomically the retina is composed of ten layers. However, these ten layers are commonly grouped into four main ones (Figure 2.2A): (1) the retinal pigment epithelium (RPE), the outermost layer above which are (2) the photoreceptors; which convert light into a neuronal (electric) signal and transmit it to (3) the bipolar cells which, in turn, are connected to the innermost layer of neurons, (4) the RGCs [22].

The RPE is a darkly pigmented layer that is not responsive to radiant energy and therefore plays no role in encoding visual information. It captures the photons which escape absorption by the photoreceptive layer. This is essential to prevent light scattering behind the retina necessary to high-contrast image [19].

By the time light reaches the photoreceptive layer, as the photopigment molecules of the photoreceptors react to light stimulus, it is absorbed and converted into electrical signals through a process known as *phototransduction*.

There are two kinds of photoreceptors, rods, and cones, that differ regarding structure, by their distinctive shapes, but mostly in function by their sensitivity to specific light wavelengths. Rods are the foundation of scotopic vision, i.e., vision at low luminance levels. On the other hand, cones mediate daytime vision, medium to high luminance levels, providing color perception and high spatial acuity. The cones are grouped into three

types depending on the wavelength sensitivity they react to: long (red light), medium (green light), or short (blue light) [19].

Rods and cones are not uniformly distributed throughout the retina as shown in Figure 2.2B. The highest density of cones is situated in the central part of the retina, known as the fovea. Thereby, the fovea encompasses a high-resolution zone, mediating detailed vision. Away from the fovea, cone density decreases sharply. The amount of rods increases, and finally declines in the most peripheral part of the retina [20].

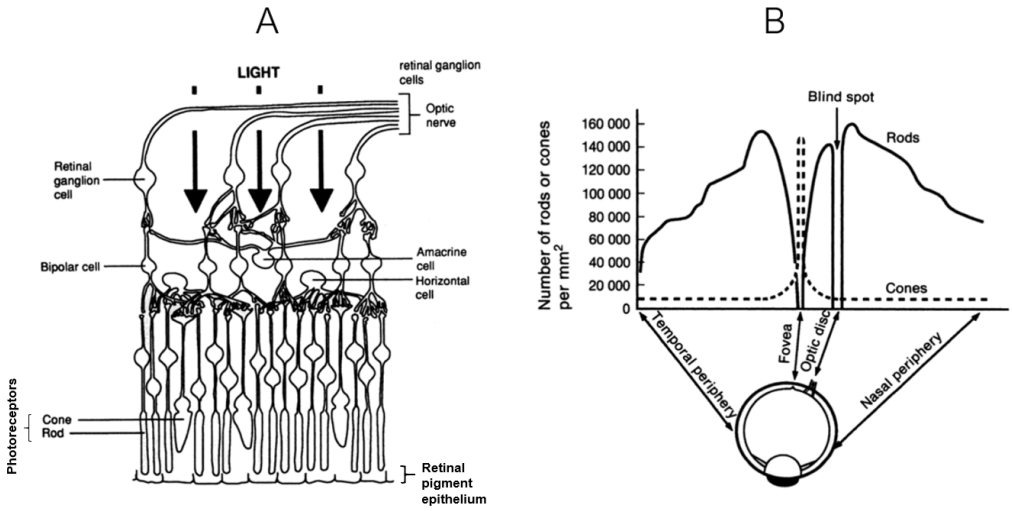


Figure 2.2: **Diagram of the organization of the retina and distribution of photoreceptors. (A)** The different types of cells and the variety of interconnections in the retina. The retina is vertically organized from the photoreceptors, on the top edge of the figure, to bipolar cells to retinal ganglion cells, on the lower edge. The vertical pathway of light is also mediated by horizontal organized cells, at the photoreceptor-bipolar synaptic layer, and amacrine cells, at the bipolar-ganglion cell synaptic layer. **(B)** The fovea contains the highest density of cones whereas in the peripheral retina rods predominate over cones. Note that are no receptors in the blind spot. Adapted from [20].

The electrical signals resulting from phototransduction set the beginning of the *vertical pathway*, a feedforward chain of synapses through the neuronal layers of the retina [20]. The electrical signals travel from the photoreceptors, via the bipolar cells to the RGCs. In addition, horizontal and amacrine cells transmit information from a neuron in one layer to adjacent neurons in the same layer (Figure 2.2A).

There are distinct forms of RGCs. They are commonly classified into two broad categories based on their anatomical features, functions, and projections onto the lateral geniculate nucleus (LGN) in the thalamus: the parvocellular and magnocellular RGCs [23]. Parvocellular RGCs, or P-cells, are the most prevalent type (approximately 80% of the RGCs). Characterized by small cellular bodies, they concern with detail and are involved in processes such as object recognition and form representation [23]. As a group, these cells form the often called *parvocellular pathway* as they project to the parvocellular layers of the LGN. Magnocellular RGCs, or M-cells, make up approximately 10% of

the RGCs and project to the magnocellular layers of the LGN, all together they form the so-called *magnocellular pathway* [23]. With larger cell bodies and dendritic arbors compared to P-cells, M-cells operate quickly, however, with a lack of detail, dealing with the processing of object localisation and motion.

The axons of RGCs come together to form the optic nerve, which serves as a highway for the signals to reach the visual areas of the brain [20]. The expansion of the optic nerve fibers is called retinal nerve fiber layer (RNFL). The optic nerve leaves the eye at the optic disc, a location also called the *blind spot*, due to a complete absence of photoreceptors (Figure 2.2B). Note that we are not consciously aware of this "blind spot", as a result of PM (discussed in detail further in this thesis) [24].

The nerves from both eyes join to form the optic chiasm. At the optic chiasm, axons from RGCs from the nasal side of the retina cross over allowing each hemisphere of the brain to receive information from the opposite side of the visual scene. Information from the right visual field travels through the left optic tract towards the left hemisphere while information from the left visual field travels through the right optic tract towards the right hemisphere (Figure 2.3A) [20]. Each optic tract terminates in the LGN.

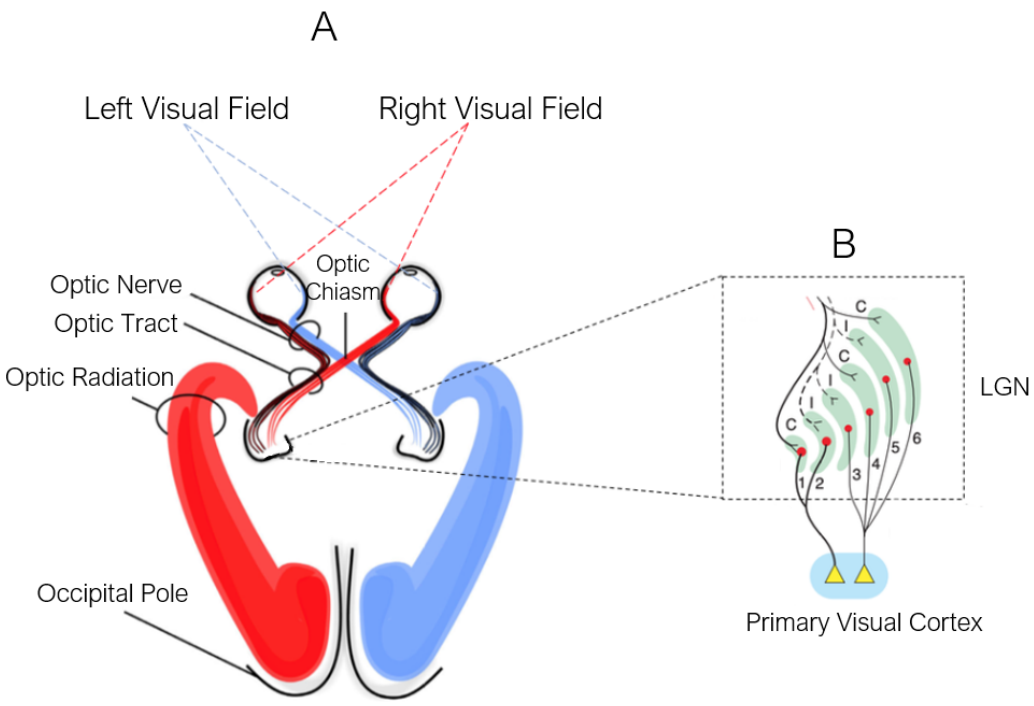


Figure 2.3: **Schematic drawing of the human optic pathway. (A)** The path of the visual information from the eyes towards the visual cortex through the right- (red) and left-hemispheric (blue) fiber pathways. **(B)** Right LGN projection to the right primary visual cortex. The LGN is made up of 6 layers. P-cells project to layers 3-6 whereas M-cells project to layers 1 and 2. The ipsilateral (I) and contralateral (C) project to alternate layers. Adapted from [25].

The LGN consists of a folded sheet of neurons cluster into six layers. The two inner layers (1 and 2) receive input from the M-cells, and the four outer remaining layers (3-6)

receive input from the P-cells. Thus, information splits into two streams: the magnocellular pathway and the parvocellular pathway. The 'magno' subdivision carries signals for motion detection, depth and flick whereas the 'parvo' subdivision deals with color vision, texture, shape and fine detail. The separation of the visual field information is conserved. Input from the ipsilateral eye terminates in layers 2, 3, and 5, and information from the contralateral eye in layers 1, 4 and 6 (Figure 2.3B) [26].

Although 'magno' and 'parvo' pathways are often described as parallel, that is only an approximation as there is actually interaction between them. This interaction allows various visual features (e.g., color, depth, form and motion) to be linked, resulting in unified visual percept. One way this linkage might be accomplished is through cells that are tuned to more than one feature [26].

After the LGN, the visual information travels through the optic radiations that ultimately project onto the visual cortex. Here, the information is integrated and processed to create an image to be perceived.

## 2.3 The Visual Cortex

### 2.3.1 Functional Areas in the Visual Cortex

The visual cortex is the ultimate stage of the visual system where the visual information is processed, and thus a synthesized image is generated. In humans, the visual cortex occupies approximately 20% of the cerebral cortex [27] and includes the entire occipital lobe (at the back of the skull), extending significantly into the temporal and parietal lobes (Figure 2.4A). It comprises 4-6 billion neurons [28].

Visual neurons are tuned to different features of the visual scene, such as color, motion, orientation, texture, shape, and depth. All these features are analyzed in parallel by separate specialized areas. Distinct cortical areas involved in visual processing have been identified in the macaque monkey [29]. With the evolution of non-invasive neuroimaging techniques, particularly fMRI, several visual areas have been recognised in the human as well [27].

V1 is the first visual area to allocate the visual input from the retino-geniculate (i.e., retina to LGN) pathway, reason why it is also known as the "primary visual cortex". Additionally, it is where the information from both eyes is first combined. Area V1 lies posteriorly in the occipital lobe and concentrates within the calcarine sulcus, which can be found on the medial surface of both hemispheres (Figure 2.4A). The intrinsic circuitry of V1 is organized into a layered structure. In Figure 2.4B a cross section of V1 shows six major layers. The principal input comes from both already mentioned 'magno' and 'parvo' pathways (section 2.2) and is allocated by layer 4. From there the visual information is processed over a complex and specific sequence of interlaminar connections. Briefly, the most superficial layers (1, 2 and 3) receive information from layer 4 and then send the outputs to higher-order areas, whereas layers 5 and 6 project onto non cortical areas, such

as the LGN and the superior colliculus (a structure in the midbrain), respectively. [26]. Information processing up to the V1 is conventionally termed as lower-level processing, responding to simple properties such as orientation and spatial frequency. Beyond V1, increasingly complex features are processed sequentially by higher visual areas.

Information from V1 towards the rest of the brain flows along two main streams each serving a different function in visual information processing: the ventral and the dorsal stream (Figure 2.4A). Along these two streams size, latency, and complexity of the receptive fields increase. The ventral stream, or "what" pathway, is associated with object perception and recognition. Damage to this stream produces impairments on object discrimination tasks. In contrast, the dorsal stream, or "where" pathway, concerns with object localization, spatial awareness, and movement detection. Damage to this stream does impair performance on visuospatial tasks. V1 projects the ventral stream to the temporal lobes and the dorsal stream to the parietal lobes (Figure 2.4A) [26].

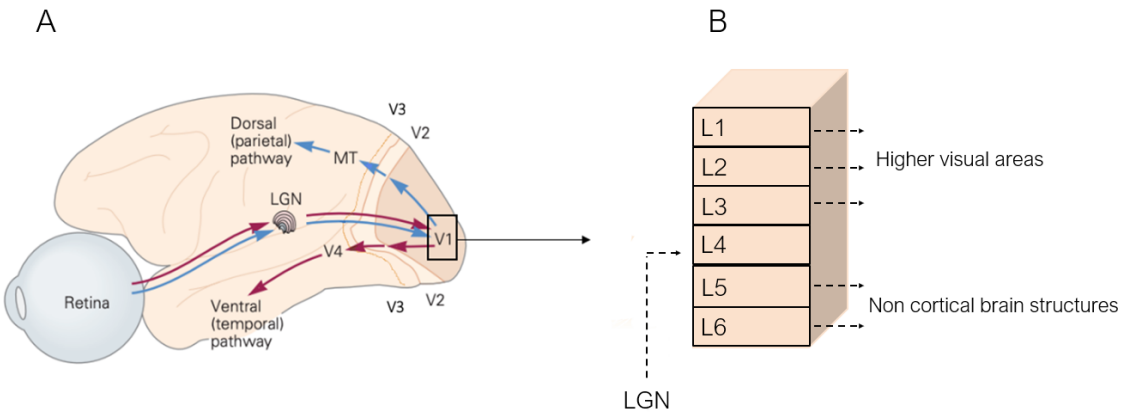


Figure 2.4: **The arrangement of visual processing framework. (A)** Information spill out of the retina to the primary visual cortex through the LGN. After the information arrives at V1, visual processing proceeds in two distinct pathways: dorsal pathway (blue) and ventral pathway (red). **(B)** V1 is segregated into six major layers The outputs are sent to higher cortical areas, back to the LGN and other subcortical nuclei. Adapted from [26].

The dorsal pathway flows from V1 and first to its adjacent visual area V2. V2, similarly to V1, responds to simple features such as orientation, spatial frequency, and color, but is also modulated by attention and more complex patterns. Then, visual information is received by area V3 and subsequently by V5 (or MT, middle temporal area) that are believed to be sensitive to visual motion and stereoscopic depth [30]. On the other hand, the ventral pathway flows into V1 to V2, V3 and lastly to V4 (Figure 2.4A).

It has been suggested that the ventral and dorsal stream can be traced back to the two principal cytological subdivisions of the RGCs: the parvocellular and magnocellular pathway. In fact, the 'parvo' pathway, with information about color and shape, would seem ideal for the 'what' pathway. Likewise, once dealing with motion information, the 'magno' pathway would seem to be the obvious candidate for the 'where' pathway. There's evidence, however, that both dorsal and ventral streams communicate, receiving input

from both 'magno' and 'parvo' pathways [31]. As an approximation the dorsal pathway is said to be magno-dominated and the ventral pathway to be parvo-dominated [32].

### 2.3.2 Retinotopic Organization of the Visual Cortex

Shaped by evolutionary and developmental constraints, the anatomical circuitry of the human sensory cortices follows the topographic organization of their corresponding sensory surfaces. In the case of the visual system, the mapping of the observed image onto the cortex results from the gathering of the RFs of individual neurons. A fundamental characteristic of the visual cortex is its ability to preserve the image's spatial relationships formed in the retina, i.e., nearby portions of the visual field are processed by neighbouring visual neurons [33] (Figure 2.5). Hence, visual areas are said to follow a retinotopic organization.

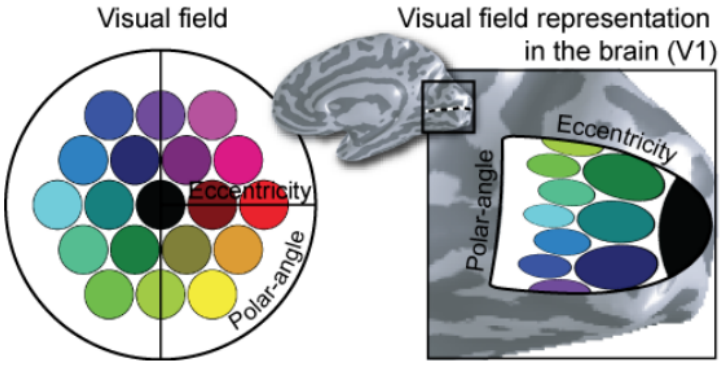


Figure 2.5: **Visual field representation in the primary visual cortex (V1).** The polar-coordinates axes, eccentricity and polar angle, are identified on the visual field on the left panel. The black circle corresponds to the centre of the visual field (fovea). On the right panel the left visual field is represented on a zoom-in figure of the calcarine sulcus, where V1 falls in, of an unfolded cortical representation. Note that there is more cortical area devoted to the representation of the central part compared to more peripheral regions of the visual field - cortical magnification [34]. Reprinted from [35]

The human visual pathways map the visual image from cartesian coordinates in the visual field to polar coordinates in cortex. As one moves along the cortical surface from a posterior to an anterior position in the visual cortex, the representation of the visual field smoothly shifts from the center (fovea) to the periphery (Figure 2.5). This is called *eccentricity*. RFs size is known to vary with eccentricity [26]. The fovea, where the resolution is highest, encompasses the smallest RFs. RFs become progressively larger with distance from the fovea. Along with eccentricity, to identify a unique location in visual space there is another dimension needed - the *polar angle*(Figure 2.5).

The type of representation illustrated by the previously described polar dimensions can be found in various visual areas, namely V1, V2, and V3, that as a group forms the

so-called early visual cortex (or early visual areas). The underlying research on this thesis focused on these three areas.

Per hemisphere, the topographic organization of V1 accommodates the representation of half of the visual field (a hemifield) with a contiguous polar angle and eccentricity (Figure 2.5). A larger portion of cortex is dedicated to the fovea than to the periphery - cortical magnification (Figure 2.5) [34]. This phenomenon is the reason why we see sharper in the fovea than in the periphery. The nearby visual field maps V2 and V3 cluster around V1, sustaining parallel eccentricity representations. However, in contrast to V1, these maps are discontinuous resulting in split-hemifield representations, i.e., quarterfinals, characterized by reversals in polar angle gradients. This happens because the information from the upper and lower visual fields is divided over dorsal and ventral sections. Thus, V2 and V3 are subdivided into V2v and V3v for ventral, and V2d and V3d for dorsal. For each map, the representation of the lower visual field comes up on the dorsal surface while the upper visual field is represented on the ventral surface. Other extrastriate visual areas are organized similarly [27].

Chapter 3

# Visual Field Defects

## 3.1 The Normal Visual Field

The visual field consists of the area of visual space in which objects are visible when the gaze is directed on a central fixation point. The visual field can be measured in terms of degrees from the center (eccentricity). With a healthy eye, a person should be able to see approximately 100º temporally (toward the ear), 60º superiorly (above) and nasally (towards the nose), and 75º inferiorly (below) from the center. The visual fields of both eyes overlap at the nasal side to form the binocular visual field which extends horizontally for 200º and vertically for 135º, with a non-overlapping 30º area temporally in each eye [36].

Central vision - part of vision that spans the macula - corresponds to the innermost 18º of the visual field, that is, up to an eccentricity of 9º. The center of the macula, the fovea, corresponds approximately to the central 2º (1º eccentricity). The remaining area of the visual field outside the central is referred to as peripheral vision.

Eccentricity has a dramatic influence on visual acuity. Once the highest density of cones concentrates in the fovea, the central vision is where a clearer and more detailed visual image can be provided. Accordingly, as the visual scene falls in the peripheral field of view visual acuity decreases gradually with the increase of eccentricity [15]. For this reason, when exploring an environment, one fixates the object of interest in order to get the maximal information.

As mentioned previously in section 2.2, everybody has a natural absolute scotoma in both eyes, the blind spot. The blind spot is due to a lack of photoreceptors in the location where the axons of the RGCs leave the retina to form the optic nerve. It lies in the paracentral visual field, typically located 15º temporal to the fixation point and 1-2º inferior to the fovea, with an area of about 6-8º [36]. The blind-spot remains unnoticed

due to the contribution of the visual brain in filling-in the gap. Depression or absence of vision anywhere else within the visual field is abnormal.

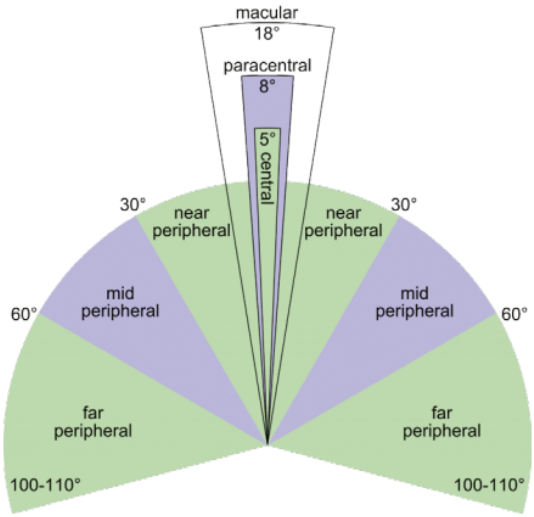


Figure 3.1: **The normal visual field.** The human field of view (FOV) for both eyes. Far, mid-, near peripheral vision, macular, paracentral and central (foveal) vision are represented and their respective limits in terms of degrees. Reprinted from [37].

## 3.2 Glaucoma

After cataract, glaucoma is the second leading cause of vision loss worldwide, typically affecting individuals over the age of 40 [1]. Glaucoma is associated with the occurrence of retinal visual field defects - area of the visual space characterized by a loss of visual acuity, surrounded by a field of spared or relatively well-preserved vision.

Glaucoma consists of a group of optic neuropathies characterized by progressive loss of RGCs, thinning of the RNFL and excavation of the optic nerve head (ONH) that together lead to a gradual increase of visual impairment [38]. Hence, when left untreated glaucoma may result in irreversible blindness.

Glaucoma is commonly classified into two broad categories: primary open-angle glaucoma (POAG) and primary angle-closure glaucoma (PACG) (Figure 3.2). All the subjects in the glaucoma group who participated in this study were afflicted with POAG[1].

POAG and PACG can be distinguished regarding the anatomic configuration of the aqueous humour outflow pathway. The aqueous humour is produced by the ciliary body and further drained by the trabecular meshwork into the venous system through a canal (Schlemm's canal). In both types, obstruction of the drainage canals occurs preventing the

[1] POAG is the most common form of glaucoma and includes two types: high-tension and normal-tension glaucoma. In the former the damage to the optic nerve is associated with IOP values out of normal range (>21 mmHg) whereas in latter such lesion occurs without an abnormal increase in IOP (<21 mmHg).

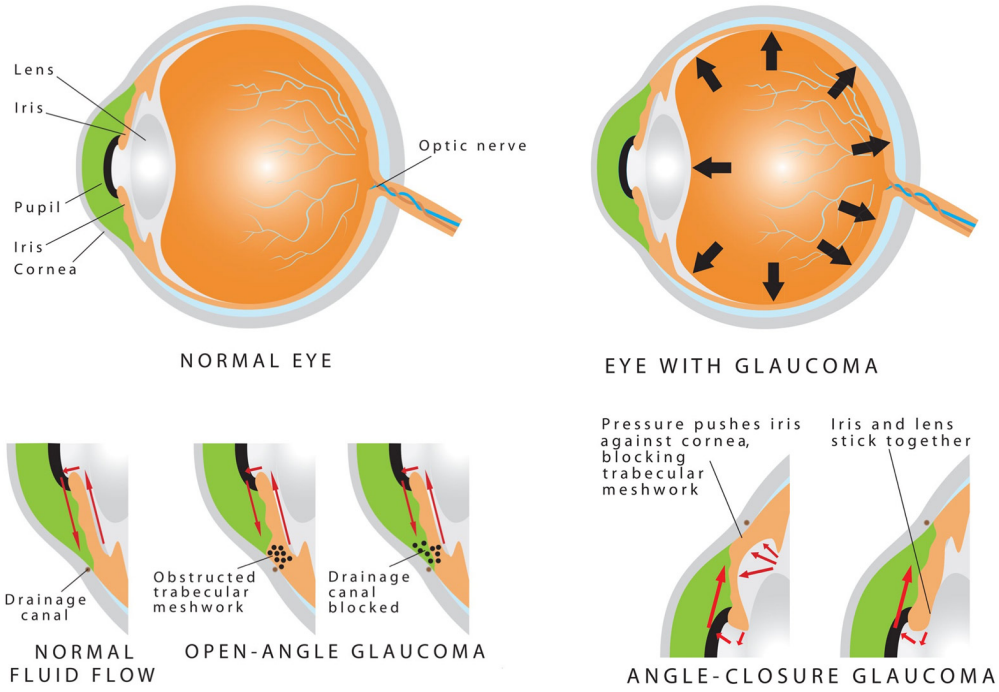


Figure 3.2: **Ocular damage in primary POAG and PACG.** Reprinted from [39].

flow of the fluid. This leads to an increase of intraocular pressure (IOP) which damages the RGCs and consequently the optic nerve. While in POAG the trabecular meshwork flow pathway is blocked internally, in PACG this obstruction is done by the iris during pupil dilatation (Figure 3.2) [40].

The rise in IOP features a progressive loss of RGCs. Additionally, with elevated IOP, the lamina cribrosa (a collagenous structure that is part of the ONH) is displaced, resulting in a phenomenon called cupping. Cupping consists of a characteristic deformation and remodeling of the ONH which results in disruption at the level of axonal transport to and from the LGN [18]. The changes in the appearance of the ONH are the most critical aspects for diagnosis and can be identified during an appropriate ophthalmologic examination of the eye (The ophthalmological screening tests performed for this thesis are mentioned and further described in section 8.2).

The miscommunication between the retina and the cortical visual brain caused by the atrophy of the ONH, culminates in visual field defects. The loss of vision begins in the mid-periphery and progresses until only a central or peripheral island of vision remains (Figure 3.3).

Based on the above statements is easy to grasp that elevated IOP is a known risk factor, presenting a strong relation with glaucoma pathology. For instance, lowering IOP is the only available treatment for glaucoma nowadays, although new therapies targeting neuroprotection of RGCs and axonal regeneration are under development [38]. However IOP is not the only factor playing a role in Glaucoma. While some patients continue to lose vision, after the IOP be stabilized at normal levels, there is a substantial number of

people with elevated IOP that never develop glaucoma. This suggests that factors, such as impaired microcirculation, excitotoxicity, and oxidative stress contribute to the disease pathogenesis and progression [18].

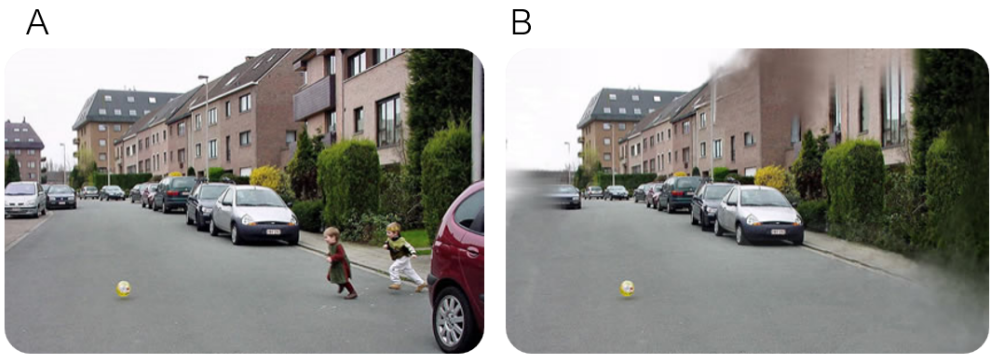


Figure 3.3: **Healthy versus glaucomatous vision. (A)** Subject view with normal vision. **(B)** Subject view with glaucoma. Adapted from [41].

As previously mentioned, RGCs neurodegeneration[2] plays a key role in glaucoma pathogenesis as it progressively leads to visual field damage. Therefore, glaucoma is traditionally considered an eye disease. Mounting evidence over the last decade, however, suggest that abnormalities in glaucoma spread along the entire length of the visual pathway, rather than limiting their effects to RGCs [3–5, 42–44]. This opens the discussion on whether glaucoma pathogenesis should be extended to brain level. A number of neuroimaging studies have been reporting brain changes in glaucomatous patients, from structure - changes in both the grey and white matter (e.g. increase or decrease) -, to connectivity and to functional responses [42, 45–47]. Yet the mechanisms underlying these changes have been extensively debated. The main question relies on the timing, i.e., whether brain changes precede or follow the eye disease.

The most parsimonious explanation seems to be that brain involvement in glaucoma is a consequence of pre-geniculate (i.e., retina and ON) damage propagation through anterograde transsynaptic degeneration[3] [43, 48]. Nevertheless, the occurrence of retrograde transsynaptic degeneration[4] have also been demonstrated, for instance, by changes found in nonvisual loci (e.g., corpus callosum and hippocampus) [43, 49] which suggest another explanation for the source of the changes rather than an indirect consequence of the ocular damage and the subsequent loss of visual input. These findings might be indicative of the brain playing a part as an independent component in glaucoma.

[2]Progressive loss of neural structure and function that ultimately results in cell death. Neurodegenerative diseases comprehend a heterogeneous group as each of them exhibits a characteristic profire of regional cell death. Also called transsynaptic degeneration.

[3]Neurodegeneration caused by loss of input. It occurs “downstream”, that means an injured presynaptic neuron causes damage to a postsynaptic neuron (e.g. distal axon terminal).

[4]Neurodegeneration occurring “upstream”. Injury at axonal level spreads back towards the proximal cell body (e.g. presynaptic neuron).

Chapter 4

# Visual Field Defects and The Brain

When visual field defects occur in both eyes, due to the retinotopic organization of the visual cortex, a certain part of the brain no longer receives stimulation. How that section of the brain further behaves is highly controversial. One might expect the silencing of the cortical area. However, functional reorganization, as a manifestation of plasticity, has been pointed out as a possible consequence for the absence of visual input.

## 4.1 Brain Plasticity

Brain plasticity, or neuroplasticity, refers to the ability of the nervous system to adapt its neuronal circuitry in response to environmental changes [50]. Despite the fact that neuroplasticity is thought to be greatest during the early stages of development (childhood), it seems to be retained throughout a lifespan, even if in a smaller degree [50, 51]. Neuroplasticity has been studied in the past decades, counting on studies in a variety of mammalian species, including humans.

The changes in neuronal architecture yielded by plasticity can be seen at different scales, ranging from synaptic activity and neuronal pathways - *synaptic plasticity* - as a result of learning, to cortical maps topography in response to bodily injury, often referred to as *cortical remapping* [52]. The scope of this thesis only covers the latter.

Deactivation or altered pattern of activation triggers the brain to adapt to the new condition. In the visual system, a visual defect associated to optic nerve damage causes brain deafferentation from the retina. This is usually followed by neurodegeneration. However, when sufficient input from neighbouring sources is still available, visual neurons are capable of acquiring new RFs by establishing new connections or by modifying the effectiveness of existing ones, leading to reorganization of the cortical representations, the basis for cortical remapping. For instance, it is widely hypothesized that after retinal

damage, neurons within V1 lesion projection zone (LPZ) (i.e., visual lesion or scotoma transformed into cortical coordinates) can still be stimulated by shifting their RFs from the blind toward intact portions of the visual field [53–55]. This 'ectopic' RFs will change V1's map. Recalling the retinotopic organization of the visual maps, as nearby neurons have RFs at nearby locations in the visual field when neurons shift their RF, the retinotopic map will change accordingly. Moreover, remapping hypothesis is also supported by the increase of RFs' size which enables the RFs to reach spared visual field and thus, become responsive to stimuli [11, 56].

Remapping as a plasticity phenomenon has been called into question [11, 57]. It is suggested that the responsiveness of neurons within the LPZ is a result of the unmasking of existing feedback signals from higher cortical areas into V1 rather than remapping.

## 4.2 Predictive Masking

When the information extracted from the visual scene is incomplete, as an attempt to compensate for gaps in perception, the visual system has the ability to predict and interpolate the missing features that are not made available to the cortex. This means that a set of neurons is activated in such a way that a visual stimulus is perceived as arising from a location in the visual field where there is actually no visual input. But how does this actually happen?

PM, or filling-in, is a heterogeneous phenomenon that takes place in different forms on a daily basis, while one observes the surrounding environment. It not only occurs when objects fall behind the blind-spot (figure 4.1), but also when an object is occluded by another, or when one stares steadily for a long time at an image with missing patches of "texture" [58]. The mechanisms underlying the various forms of PM are still not totally clear. Regarding literature, there are two broad proposed models that aim to explain such perceptual phenomenon. First, the symbolic or cognitive theory states that PM is a passive process, the structures from the visual system simply ignore the lack of information and label the region to be completed with the same visual features as the surround [59]. This mechanism is shortly described as "more of the same" [58]. On the other hand, some studies propose that the phenomenon is not a result of simply ignoring a section within the visual field, instead it relies on active neuronal activity. This second model, termed as "isomorphic model", assumes that PM is mediated by lateral propagation of neural signals, with the spread of activation across the retinotopic map of the visual cortex from the border to the interior of filled-in surface [60]. PM might be alternatively explained by the occurrence of passive cortical remapping, in a way that the receptive fields from the region corresponding to the scotoma or blind-spot are displaced towards the surrounding region representing the scotoma or blind-spot [54].

Activation of early visual areas (V1-V3) is suggested to be involved in representation of filled-in regions of an image. For instance, previous fMRI experiments [61, 62] showed clear activation of the early visual cortex when subjects were asked to perform

an attention task that consisted of following a filling-in stimulus presented at different places of the visual field. The same stimulus was presented when attention was not controlled. Interestingly, both V1 and V2 showed activation regardless of where the subject attended. These findings are indicative of automatic PM of activity at early stages of cortical processing.

PM occurs not only in normal conditions but also in disease. Comparably to our unawareness of the blind-spot, due to this remarkable phenomenon patients with retinal and cortical damage can remain unconscious of their defects [30].

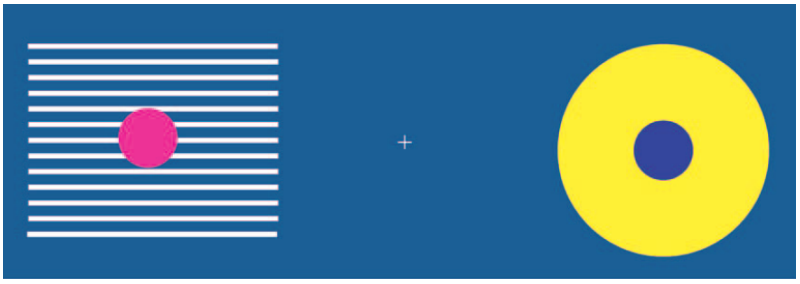

Figure 4.1: **Filling-in at the blind-spot.** The absence of photoreceptors at the location where the optic nerve leaves the eye results in a blind area in the retina: the blind-spot. To find the blind-spot in your eye, fixate the gaze on the cross at the centre and cover your left eye. Then slowly move towards the image, still staring at the cross. At a certain distance (about 15 cm) the smaller blue circle on the right will disappear. The image falls now on the blind-spot. At the same time, a large yellow disk is seen. By covering the right eye and the left eye's gaze fixed on the middle cross, the uniform horizontal grading on the right can be seen even though the middle part of the stripes falls inside the blind spot. This is called perceptual 'completion' and is due to the pattern filling-in on the left eye's blind-spot. Reprinted from [6].

Chapter 5

# Functional Magnetic Resonance Imaging

The emergence of fMRI in the early 1990s had a real impact on the scientific world, leading the method to become the current mainstay of neuroimaging in cognitive neuroscience. Since the first carried fMRI study, the number of papers that mention the technique has grown exponentially [95]. The explosion of interest around fMRI lies on its non-invasive nature of measuring and mapping brain activity done with a very good spatial resolution and relatively good temporal resolution.

## 5.1 The BOLD Signal

In response to stimuli neurons become active in given areas of the brain. This increase in brain activity elicits a need for oxygen and glucose consumption which is overcompensated by an increase in regional cerebral blood flow. The local mismatch between oxygen demand and oxygenated blood flow induces changes in the ratio between oxyhemoglobin (hemoglobin bound to oxygen) and deoxyhemoglobin (hemoglobin without bound oxygen). Oxyhemoglobin and deoxyhemoglobin have different magnetic properties, which result in different magnetic resonance (MR) signals (see annex I for information about MRI principles). While oxyhemoglobin behaves as a diamagnetic substance, i.e., exhibits a weak repulsion from a magnetic field, deoxygenated hemoglobin is paramagnetic, which means it causes disruption in the magnetic field. These differences in magnetic susceptibility will be reflected in an image, allowing us to distinguish active regions (presumably with high oxygen consumption) from inactive regions of the brain. Areas assigned with high concentration of oxyhemoglobin produce a higher signal compared to the one that emerges from areas with lower oxygen levels [63]. The dependence of the recorded signal from blood oxygenation sets the basis of the technique and is the reason why it is often referred to as blood-oxygen-level-dependent (BOLD) imaging.

The regional BOLD signal that results from presentation to sensory space of a given stimulus follows a stereotypical shape referred to as the *hemodynamic response* (Figure 5.1). The hemodynamic response can last up to 20 seconds and is characterized by a small *initial dip*, followed by a *peak*, and lastly a variable *post stimulus undershoot*. There is a temporal delay to peak of approximately 5s after stimulus processing represented by an initial dip which results from an increase in deoxyhemoglobin concentration. This is then replaced by the positive dominant peak that constitutes the bulk of the BOLD response. Throughout this stage, blood flow increases to immediate metabolic needs. As result, ratio between oxy- and deoxyhemoglobin rises proportionally to the underlying neuronal activity, leading to an increase of the MR signal. If the neuronal activity is extended over time, the peak may extend to a plateau. After stimulus cessation, since the needs of neuronal activity are met, the MR signal drops, slowly returning to baseline level and, eventually, underpasses it. This is called the undershoot effect and derives from the venous bed capacity that tends to cause a normalization of the regional blood volume faster than the changes in blood flow, leading to relatively high deoxyhemoglobin concentration [64].

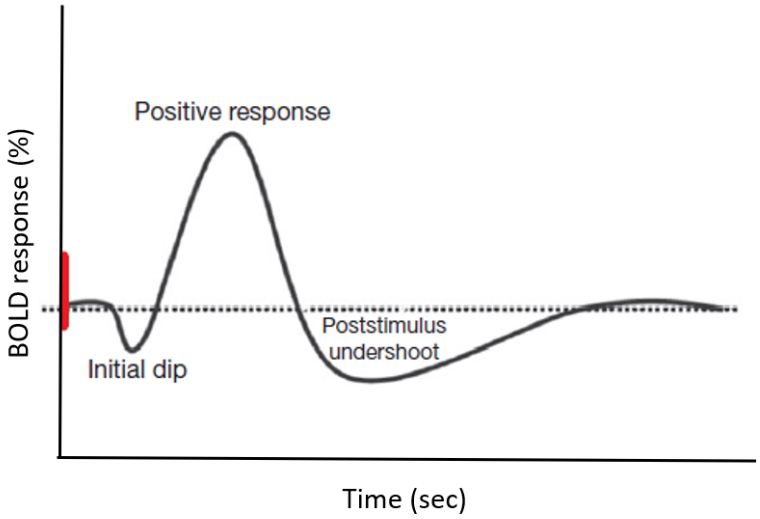


Figure 5.1: **Illustration of a hemodynamic response evoked by neuronal activity in response to a hypothetical brief stimulus (red bar).** The hemodynamic response follows a stereotypical shape that consists of initial dip, positive response (peak), and poststimulus undershoot. Adapted from [64].

The interpretation of the BOLD response is still a topic of active research because it can not be seen as a reflection of neuronal activity. Instead, it must be considered as an indirect measure of neuronal activity through the changes in local oxygenated blood ratios [63].

The hemodynamic response is often treated as a linear time-invariant (LTI) system [65, 66]. Linearity means that the neural response and the BOLD response are scaled by

the same factor. The meaning of linearity is also associated to additivity which means that if there is knowledge what the response is for two separate events, and they both occur close in time, the resulting signal would be the sum of the independent signals. Time invariant means that if an event is shifted by $t$ seconds, the BOLD response is expected to shift by the same amount.

Chapter 6

# Visual Field Mapping

In the field of visual neuroscience, fMRI combined with computational methodologies has been used to respond to the need to identify information that goes beyond detecting the presence or absence of a fMRI signal [67]. The existing techniques take advantage of the retinotopic organization of visual input to measure visual field maps regarding the two orthogonal dimensions needed to identify a specific location in visual space: eccentricity and polar angle (section 2.3.2).

One of the most powerful fMRI techniques to map the visual field is the traveling wave retinotopy (TWR) (also called phase-encoded mapping), illustrated in figure 6.1 [68]. Since its urge in the mid 1990s it has been considered the gold standard for visual field mapping. The TWR allows the estimation of the location in the visual field that maximally excite each fMRI voxel. This is done by using two types of periodic stimuli, expanding/contracting rings and (counter-)clockwise rotating wedges, designed to map each voxel's prefered eccentricity and polar angle respectively. These stimuli are typically comprised to a set of high-contrast flickering checkerboard patterns which are known from literature to evoke robust neuronal response within V1 of humans [68] and to elicit a BOLD signal modulation on the order of 1%-3% [69]. The name of the technique comes from a resulting traveling wave of cortical activity upon stimulation that travels from one side of the visual field map to the other along iso-angle or iso-eccentricity lines. As a result, the peak modulation alternates periodically across the cortical surface and, thus, the delay can be measured by the phase of the underlying neuronal activity. This phase indicates the most effective stimulus eccentricity and polar angle to fire neurons comprised in that region of the cortex.

Regardless of the potential of TWR to uncover visual field maps in the human brain (approximately sixteen maps have been identified thus far), because of the method's reliance on the periodicity of the stimulation sequence, it is only suitable for activating

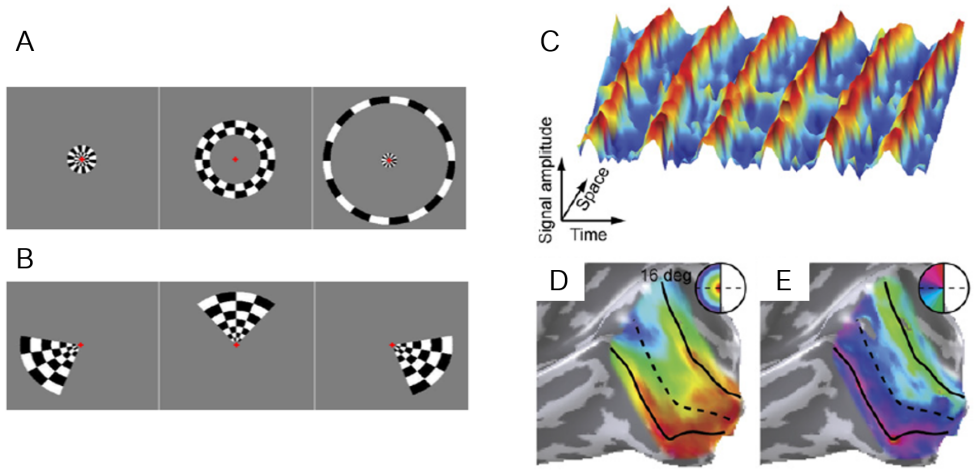


Figure 6.1: **Traveling Wave Retinotopy.** Traveling wave stimuli typically consist of a set of high contrast checkerboard patterns that move smoothly and periodically across the visual field through a range of eccentricities (expanding/contracting ring) **(A)** or polar angles (clockwise rotating wedge) **(B)**. The time, or phase, of the peak modulation smoothly varies across the cortical surface **(C)**. In this example six stimulus repetitions are represented. An expanded view of the cortical surface near the calcarine sulcus is overlaid with a color map representing the response phase at each location for both eccentricity **(D)**, elicited by the ring stimuli, and polar angle **(E)**, derived by the wedge in the stimuli sequence. Adapted from [27].

retinotopically-organized areas (early visual cortex). Hence, TWR has limitations when measuring higher order visual field maps with large RFs [27]. Once these limitations became clear, Dumoulin and Wandell decided to improve visual field mapping techniques by developing a model-based approach that extends the notion of RF [17]. As each typical fMRI voxel (3 mm isotropic) cluster the responses of about 3 million neurons and each neuron responds to a preferred location on visual field (RF), based on visual field maps retinotopic organization the RFs within one voxel are expected to present similar characteristics. Therefore, the ensemble of the RFs of all neurons also create a RF, the "population receptive field" (pRF). Unlike TWR approach, the new method provides an estimate of the location and size of the neuronal pRF. Additionally, the pRF approach does not require distinct phase-encoded stimuli, the standard ring and wedge, to infer eccentricity and polar angle. Instead, the orthogonal dimensions can be measured by using a single non-periodic stimuli, a drifting bar (Figure 6.2), cutting down the total number of scans per subject. The underlying goal of this methodology is to test which of a wide range of pRF models best predicts the BOLD signal for each voxel (Figure 6.2). The pRF is modeled as a simple two-dimensional Gaussian defined by three parameters: $x_0$, $y_0$, and, $\sigma$ . The two spatial coordinates ($x_0$, $y_0$) assign the pRF center position in the visual field whereas the Gaussian standard deviation ($\sigma$) refers to the pRF size. The latter parameter is of great relevance in the context of visual cortical plasticity, as will be

discussed in more detail further in this thesis. For each voxel, after an extensive database of pRF parameters candidates is created, the method calculates a predicted BOLD signal as result of the overlap between the stimulus information at each time point and the model pRF. The outcome is then convolved with a hemodynamic response function (HRF), to account for the delay in hemodynamic response. Following this, the goodness of fit of the model to explain the actual BOLD response is estimated according to each voxel's activity over time. This is done until the pRF parameters that best minimize the difference between the prediction and the measured data are found.

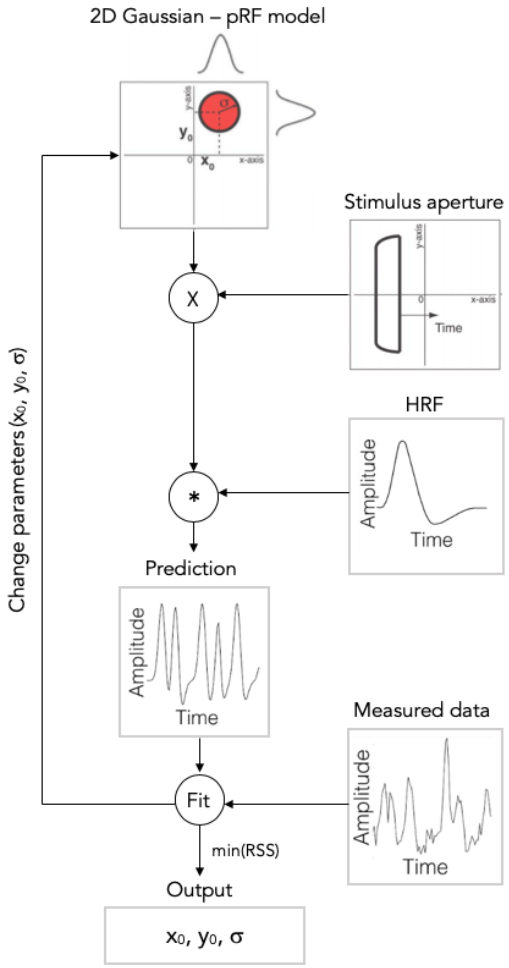


Figure 6.2: **The population receptive field (pRF) modeling pipeline.** Voxel wise the method models the pRF as a two-dimensional Gaussian described by position in visual field ($x_0$,$y_0$) and size ($\sigma$ of the Gaussian). By overlapping the pRF model with the stimulus aperture (moving bar), a voxel's activation response is predicted. Then, the predicted BOLD signal is estimated as a result of the convolution between the pRF activation response with a hemodynamic response function (HRF), to account with the hemodynamic response delay. Ultimately, by determining the error between the prediction and the actual measured data, the best fitting model for each cortical location can be estimated. Adapted from [17].

Chapter 7

# Population Receptive Field (pRF) Changes in Opthalmic and Neurologic Diseases: State-of-the-Art

Over the last two decades, visual field mapping has been extensively used to infer neuronal reorganization resulting from visual field defects or neuro-ophthalmologic diseases. Because of its focus on the analysis of individual participants and the relative amount of detail provided, the pRF model seems ideal to study questions on neuroplasticity – at least in theory. In developmental disorders, studies have consistently reported marked changes that far exceed those observed in health. However, in the adult brain, there is a long-lasting controversy surrounding observations that pRFs can change. The question is whether altered pRF parameters are a reflection of cortical reorganization or whether such changes may be explained by the same dynamics present in the neural circuitry of healthy individuals.

A long tradition of invasive animal neurophysiological studies that aimed to elucidate how RFs and cortical visual organization are altered lodged arguments that are important for how pRF changes may follow disorder-induced retinal lesions. Through experimentally induced damage to the retina of adult mammals, Gilbert and Wiesel reported remarkable changes in V1 RFs [9]. Namely, neurons with RFs near the edge of the lesion increased the RF size whereas neurons with RFs inside the insult reconfigured their position towards portions of spared retina. The authors claimed the findings as a result of reorganization of the RFs properties due to synaptic changes intrinsic to the cortex. However, this conclusion was contended by others [57] who argued that changes in RF properties do not require to be explained by cortical reorganization. Alternatively, the presence of activity in deprived visual cortex reported previously may be the result of gain adjustments that reduce feedforward information or a downregulation of inhibition.

In human studies, stimulus manipulations to mimic blind regions – e.g. by removing the stimulus at a given position [11, 70] or by diminishing light to simulate scotopic vision [71] (when only rods operate) - have been a powerful tool to investigate the effects of such visual deficits in pRF measurements. Reduced signal amplitudes, shifted pRFs and scaled pRF sizes in the vicinity of the simulated lesion site have been often observed as a result of these simulations. As so, the differences in pRF properties arising from simulation of lesions in healthy adults support and extend the notion that changes in neuronal populations are not unique identifiers of cortical reorganization.

In healthy adults, the resulting retinotopic maps are stable over time [72]. Hence, it would appear that changes in maps or population properties should be a good indication for the presence of neuroplasticity. In a study conducted by Baseler and collaborators in individuals diagnosed with macular degeneration (MD) - an ocular disease characterized by a visual blind spot (scotoma) in central vision - pRF properties were measured in the foveal region of the patients [11]. It was found that the pRFs of voxels representing both the scotomatic area and neighboring regions are displaced and changed in size. However, well-sighted controls in whom a central scotoma was simulated shared the same pattern of results. This finding challenged the notion of electrophysiological studies that changes in RFs are evidence of cortical reorganization. Hence, the authors argued for a lack of neuroplasticity in patients with MD. Barton and Brewer also found comparable shifts in pRF position and scaling of pRF size in their experiment that used scotopic illumination levels to examine the "rod scotoma"in the central visual field [71]. Others further confirmed the observation of altered pRFs in healthy individuals in the vicinity of a simulated scotoma [73, 74]. This implies that observed differences in pRF properties in patients relative to controls may simply reflect normal responses to a lack in visual input rather than a reorganization of the visual cortex.

In the case of congenital visual pathway abnormalities that affect the optic nerve crossing at the chiasm, e.g. achiasm, albinism and hemi-hydranencephaly, each hemisphere receives input from the ipsi- and contralateral visual hemifield. In other words, each hemisphere grossly represents both left and right visual hemifields. Accordingly, several studies revealed overlapping visual fields and bilateral vertical symmetric pRF representations [75–77]. Such evidences surpass the realm of typical cortical reorganization. Nevertheless, no changes in pRF sizes and other properties of visual pathways have been found, thus it is speculated that visual functions is preserved in these pathologies by reorganization of intracortical connections rather than by large-scale reorganization of the visual cortex.

Given that visual neuroplasticity is greatest during early stages of development (childhood), the characterization of the pRF properties has special relevance to test, *in vivo*, the presence of atypical properties of the visual cortex during development and plasticity. Changes in pRF size have been reported in a series of studies on developmental disorders, such as amblyopia, commonly referred to as the lazy eye, characterized by a reduction in

visual acuity of one eye. Clavagnier and colleagues measured enlarged pRF sizes in primary visual areas (V1-V3) in the cortical projection from the amblyopic eye as compared to the fellow eye. They ruled out the contribution of eye movements for the increase in pRF size by measuring the fixation stability in both eyes. Consequently, the authors attributed the changes to a possible loss of neural resolution or neural disorganization [78].

Schwarzkopf and colleagues reported that individuals with autism spectrum disorder have larger pRFs in the extrastriate cortex but not V1 and V3, as compared to controls. They suggested extrastriate cortical hyperexcitability or differential attentional deployment as likely explanations for the abnormal cortical organization [79].

Anderson and colleagues found smaller pRF sizes in the early visual cortex of individuals with schizophrenia compared to controls, using a specific pRF model that takes into account the center surround structure of the RFs [80]. They proposed that the imbalance between cortical excitation and inhibition could change the pRF-center surround configuration and thereby explain the visual field defects perceived by schizophrenic individuals.

Papanikolaou and collaborators measured pRF properties in 5 individuals with partial or complete quadrantic visual field loss resulting from V1 injury. They compared the results with healthy controls with deprived of visual stimulation in one quadrant. The authors alleged that these patients retained a limited degree of plasticity in V1 manifested by a small shift in pRF centers toward the border of the scotoma and a slight increase of pRF size near the edge of the lesion, as well as in the contralesional hemisphere [70].

Lesion-induced plasticity of the visual cortex is widely associated to reorganization of the retinotopic maps which has been motivating a series of laboratories to improve techniques to assess the topography of visual cortex. The pRF modeling approach has been applied with at least some degree of success to reveal neuroplastic changes at the level of the visual cortex, especially in the context of diseases acquired during early windows of brain development. Regarding the adult brain, despite evidence of changes in pRF properties, as these have been found in healthy people, it is still speculated whether 'ectopic' RFs reflect a neuroplastic mechanism or the unmasking of pre-existing cortico-cortical connections.

Chapter 8

# Materials and Methods

## 8.1 Study Design and Population

Twenty individuals with POAG (10 males; average age: 70; age-range: 55-85) were recruited at the University Medical Center Groningen, Groningen. Six age-matched participants (4 males; average age: 62.5; age-range: 53-71) were included in the study as controls for the POAG group. All control participants had normal or corrected-to-normal vision. The initial goal was to have the same (or approximate) number of participants in each group. Difficulties in the recruitment stage of healthy participants did not make this possible.

Prior to MRI scanning, participants signed an informed consent form. Experimental protocols were approved by the University Medical Center Groningen, Medical Ethical Committee and conducted in accordance with the Declaration of Helsinki.

The inclusion and exclusion criteria underlying participants recruitment are listed as follows:

**Inclusion Criteria**

General Inclusion Criteria:

- Signed informed consent;
- Aged 18 years or older.

Group-dependent Criteria:

The group-specific inclusion criteria, i.e. for healthy controls and glaucomatous participants, are given in table 8.1.

Table 8.1: **Summary of group-dependent inclusion criteria.** Although glaucomatous patients appear differentiated according to the disease stage, due to its relevance for other studies' purposes, in this thesis we did not treat them separately. IOP, intraocular pressure; VF, visual field; MD, mean deviation; OCT, optical coherence tomography.

| Group | Description | IOP | VF | OCT | Family History |
|---|---|---|---|---|---|
| HP | Healthy Participants | =<21 mmHg[b] | No VF defect | Normal | Negative regarding glaucoma |
| GS | Glaucoma Suspects[a] | >21 mmHg | No VF defect | Abnormal | - |
| MP | Mild POAG Patients | >21 mmHg | Defects due to glaucoma | Abnormal | - |
| SP | Severe POAG Patients | >21 mmHg | Defects due to glaucoma | Abnormal | - |

[a] GS are defined as subjects with an intact VF and at least 2 out of 3 abnormal from the following aspects: IOP, OCT and family history criteria. [b] Value of IOP above 21 mmHg is indicative of glaucoma [81].

**Exclusion Criteria**

General Exclusion Criteria:

- Psychiatric disorder, current and/or past;
- MR- incompatible implants;
- Claustrophobia;
- Non-MRI safe tattoos;
- Use of recreational drugs or medications which may influence neurodegenerative progression.

Exclusion criteria specific to the Glaucoma group:

- Non-glaucoma related neurological symptoms, current and/or past;
- Non-glaucomatous visual field loss;
- Myopes (beyond -3 D) and hyperopes (> +3 D);
- Refusal to be informed in the event of the discovery of an ophthalmic or neurological abnormality - not related to glaucoma.

Exclusion criteria specific to the healthy participant group:

- Neurological symptoms, current and/or past;
- VA < 0.8;
- Any visual field loss;
- IOP > 21mmHg;
- Positive family history of glaucoma;
- Refusal to be informed in the event of the discovery of an ophthalmic or neurological abnormality.

Healthy participants underwent ophthalmic screening prior to participation in the main experiments. This information was also acquired from the patients with ophthalmic information older than six months. Following inclusion, participants took part in the MRI experiments where anatomical and functional data were acquired. Figure 8.1 shows a flow diagram of the study.

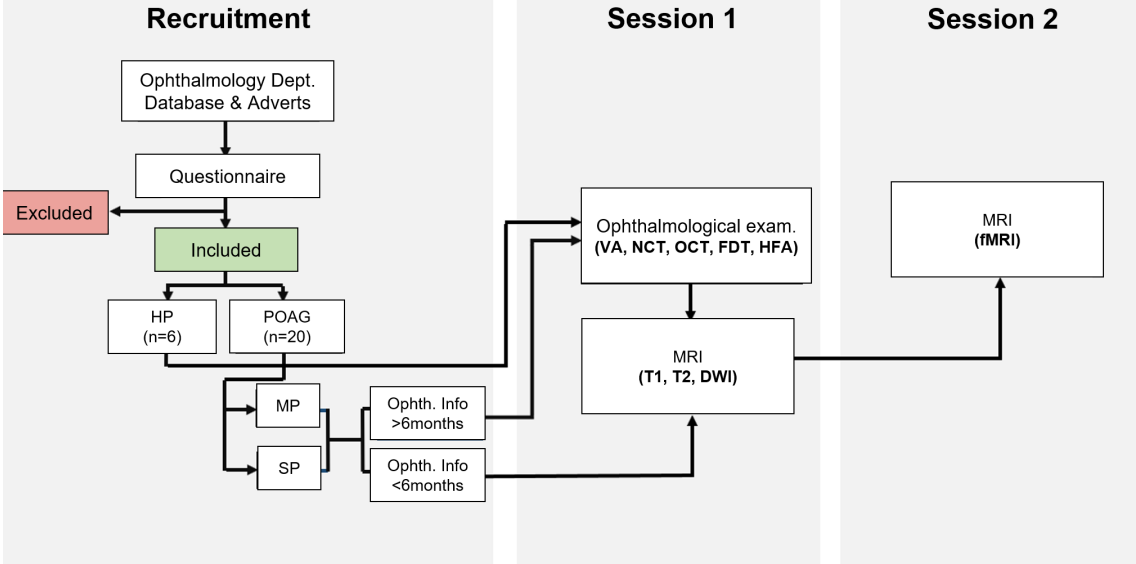


Figure 8.1: **Flow diagram of the study.** VA, Visual acuity; NCT, non-contact Tonometry; OCT, optical coherence tomography; FDT, frequency Doubling Perimetry; HFA, humphrey field analyser; DWI, diffusion weighted imaging

## 8.2 Ophthalmological Screening

Nowadays there are several ophthalmological evaluations that can be performed in order to assess the visual field and quantify its abnormalities. The subjects of this study underwent the following examinations:

**Visual Acuity (VA)**

Assessed using a standardized letter chart. Subjects are asked to read the smallest print on the chart.

**Non-contact Tonometry (NCT)**

A gentle puff of air directed to the corneal surface of the eye is used to measure the IOP of the subject, without any mechanical contact with the eye. Increased IOP (>21 mmHg) [81] is indicative of a possible presence of glaucoma.

**Optical Coherence Tomography (OCT)**

An evaluation of the thickness of the subject's retina is made, taking two images: one of the fovea and one of the ONH (Figure 8.2C). Thinning of the retina is indicative of the possible presence of glaucoma.

**Perimetry**

Perimetry consists of a quantitative examination of the visual acuity throughout the entire visual field. All perimeters measure sensitivity to stimuli at different locations which allows the mapping of visual sensitivity along the visual field. Sensitivity is then expressed as a deviation measure from the norm within the age group of the subject. An area assigned with sensitivities significantly below the considered normal value may be indicative of a visual field defect. In this study perimetry was performed using the following perimeters:

- **Frequency Doubling Perimetry (FDT):** visual fields are assessed for blind spots using the C20-1 Frequency Doubling Perimetry test (Carl Zeiss Meditec, Dublin, California, USA). Weak flickering sinusoidal gratings are presented to different locations in the visual field. Subjects are asked to press a button if they see the stimulus. The sensitivity map of each eye is represented in greyscale (Figure 8.2A) where lighter regions correspond to higher visual sensitivity whereas darker regions reflect lower sensitivity.

- **Humphrey Field Analyser (HFA):** HFA (Carl Zeiss Meditec, Dublin, California, USA) is an instrument for the automated evaluation of the visual field, pointed as the second generation of perimetry as its performance provided enhancements to the diagnostic capabilities of FDT. During the examination, the subject is asked to cover one eye, and to fixate the other on a central light located in the middle of the inside of a sphere. Small flashes of light of varying intensities are presented at various locations throughout the sphere and thus, the visual field. Alike FDT, the subject is requested to react to flash by pushing a button. The printout values of each tested point are expressed in decibels (dB) in the sensitivity plot (Figure 8.2B). HFA can measure sensitivities extending from 0 dB to 50 dB. Higher values mean the subject was able to see a more attenuated light and thus has more visual sensitivity at that location than the aged-matched normal average. If the subject is unable to see the stimulus at a given location it is assigned with a negative number, that means a decreased contrast sensitivity from normal. The visual field is also represented in a grayscale plot (Figure 8.2B). Generally, each decrease of -3dB is associated with a halving of the contrast sensitivity. Accordingly, visual field regions associated with values from about -13 dB downwards are marked in black and considered scotomatic.

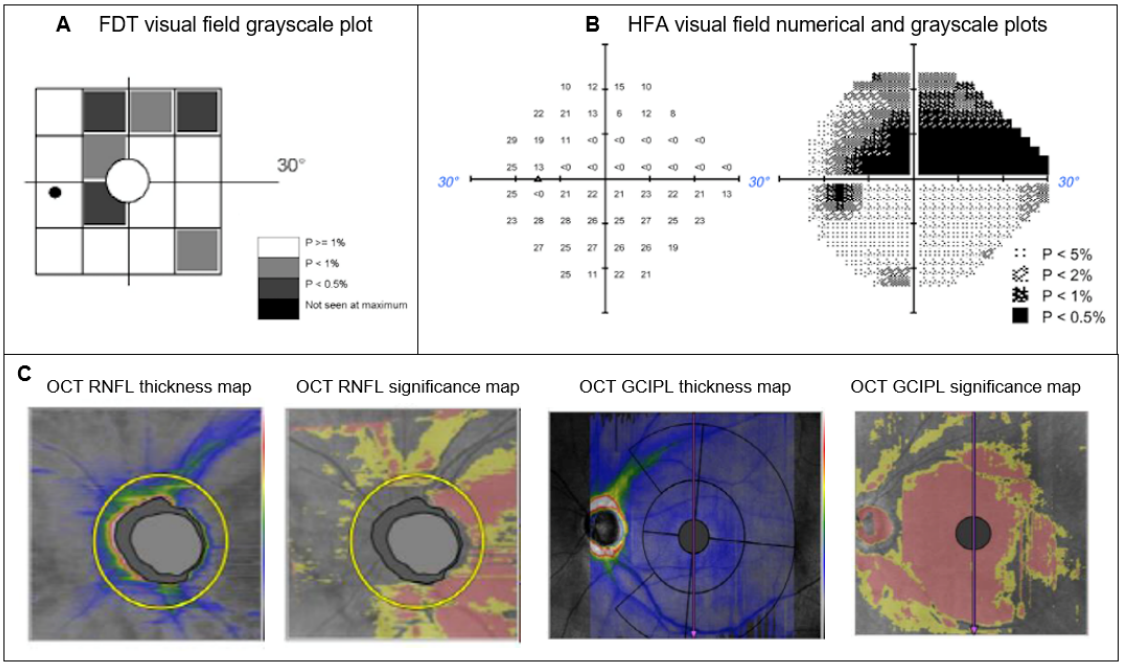


Figure 8.2: **Examples of ophthalmic evaluations' outcomes. (A)** The visual field grayscale plot of the left eye from FDA testing is presented. The screening test begins by presenting stimuli at a contrast level that 99% of healthy age-matched subjects would be expected to perceive. If the stimulus is detected, the target positions of the visual field are labeled with P>=1% and are not retested. For the unseen sections of the visual field, another stimuli is presented which would be expected to be seen by 99.5% of the healthy age-matched subjects. If it is seen, the locations is labeled with P<1%. If missed, the target is presented with a stimulus at maximum contrast (100%) and labeled with P<0.5% if seen or with "not seen at maximum" if not perceived. **(B)** The HFA output plots of threshold sensitivity (left panel) and grayscale codification (right panel) of the left eye of a subject are shown. The threshold sensitivity plot which consists of the numeric values of sensitivity of each point of the visual field tested (in dB). Negative values (<0) suggest a decreased in sensitivity to the presented stimulus below normal range. The grayscale plot is a symbolic representation of the numeric scale. It illustrates sensitivity values closer to 0 dB with black and and those closer to 50 dB with white. The statistical display (located below the grayscale plot) demonstrates the percentage of the normal population who measure below the patient's value at a specific retinal point. **(C)** The warmer color on the OCT RNFL thickness maps represent a thicker RNFL whereas cooler colors represent a thinner RNFL. The OCT RNFL significance maps are constructed with reference to data collected from healthy subjects. Red and yellow areas represent measurements below the 99th and 95th percentile ranges, respectively. OCT ganglion cell inner plexiform layer (GCIPL) thickness maps and significance maps are colour coded similarly to the RNFL ones.

## 8.3 Visual Stimulation

### 8.3.1 Stimulus Presentation

Computer-generated stimuli were presented on an MR compatible display screen (BOLDscreen 24 LCD; Cambridge Research Systems, Cambridge, UK). The screen was located at the head-end of the MRI scanner. Participants viewed the screen through a tilted mirror attached to the head coil. Distance from the participant's eyes to the display (measured through the mirror) was 120 cm. Screen size was 22×14 degrees. In this configuration, the maximum stimulus radius was 7 degrees of visual angle. Visual stimuli were created using MATLAB (Mathworks, Natick, MA, USA) and the Psychtoolbox [82, 83].

### 8.3.2 Stimulus Description

The presented visual field mapping stimuli differed between the glaucomatous and the control population. For glaucomatous participants visual field mapping was performed using luminance contrast retinotopy (LCR). In addition to LCR, LCR with artificial scotoma superimposed (LCR AS) was used in the control group.

#### 8.3.2.1 Luminance-contrast defined retinotopy (LCR)

LCR consists on a high-contrast luminance checkerboard drifting bar on a gray background [17] (Figure 8.3A). The black and white checks rows drifted in opposite directions along the orientation of the aperture. Bar apertures were displayed at four different orientations, i.e. horizontal, vertical, and two diagonals, in two opposing motion directions each, giving a total of eight configurations within a given scan (Figure 8.3C). The bar moved across the screen in 16 evenly spaced steps each lasting 1 TR and its contrast, width and spatial frequency were 100%, 1.75 and 0.5 cycles per degree, respectively. Periods of mean luminance (zero contrast) field were also included after each pass and a half and lasted for 12s. The mean luminance blocks avoid systematic underestimation of the pRF size [17].

#### 8.3.2.2 Luminance-contrast defined retinotopy with artificial scotoma superimposed (LCR AS)

To control for the effect that neuronal responses may result from differences in the perceived visual stimulus rather than plasticity we designed LCR AS (Figure 8.3B). Here, each aged-matched control was assigned to a glaucoma patient. This pairing was done based on demographic parameters such as age and gender. LCR AS consisted on the LCR stimulus with an AS (total or partial reduction in contrast) superimposed. Per aged-matched control the AS was designed to mimic the contrast sensitivity of the glaucoma patient assigned to it. In particular, the AS consisted on an alpha transparency contrast

layer defined using the HFA (section 8.2) sensitivity values of the respective glaucoma patient.

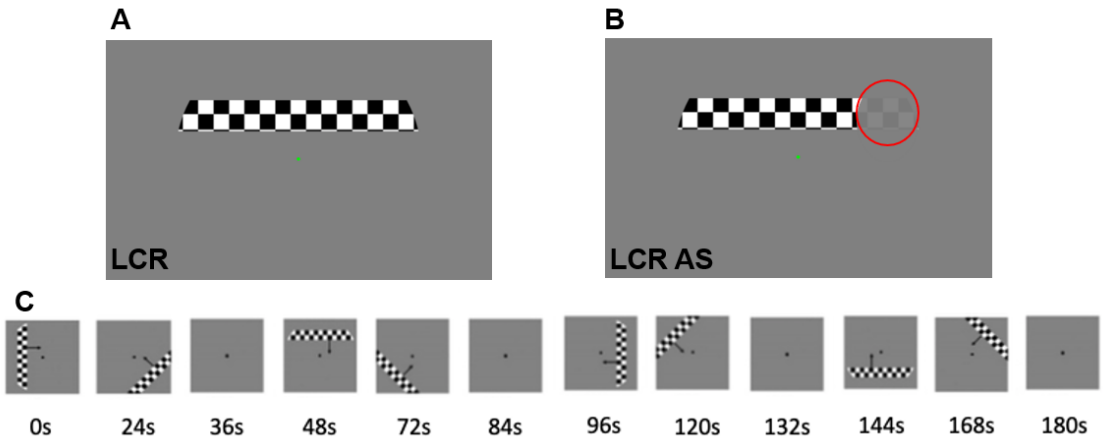


Figure 8.3: **Example of the stimuli used to obtain pRF parameter estimates. (A)** LCR stimulus. **(B)** LCR AS stimulus. For visualization purpose the AS is outlined with a red line. This red line was not presented to the participants. **(C)** Stimulus schematic. Bar apertures are presented at 4 different orientations in two opposing directions (eight configurations in total) Four mean luminance periods of 12s duration were inserted in between each two configurations. These mean luminance blocks are needed to obtain accurate estimations of large pRF sizes [17]. The black arrows indicate the aperture's motion direction and were not present during the experiment. Even though the LCR stimulus is depicted, for the LCR AS one the temporal and motion sequence across the visual field was the same.

#### 8.3.2.3 Scotoma Localizer

Low spatial frequency localizers scans were used to obtain the locations of the Scotoma Projection Zone (SPZ). The localizer stimuli consisted of alternating blocks of 12 seconds containing the following: baseline, stimulating the scotoma location only and background stimulation. The scotoma and background content was a spatially band passed filtered dynamic white noise at a frequency of 0 to 2 cpd. A total of 18 blocks were presented in pseudo-randomized order. Participants were instructed to fixate on the fixation cross and perform the attentional task.

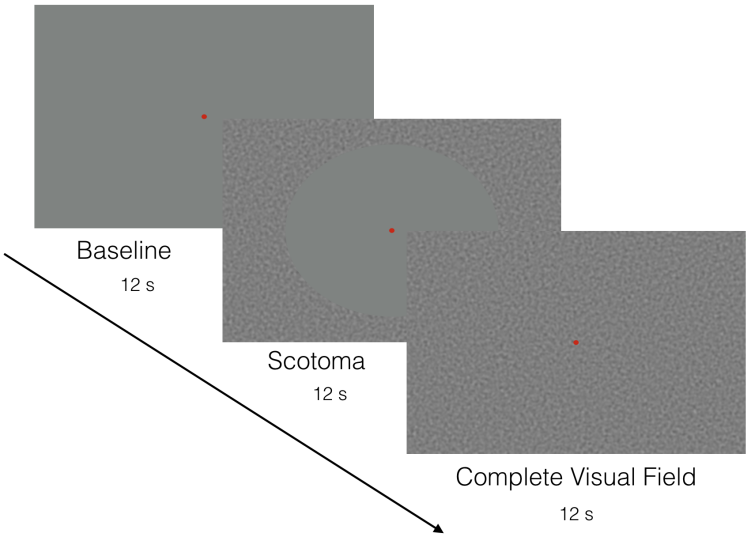


Figure 8.4: **Example of the stimuli used to obtain SPZ location.** Scotoma and background stimulation using low frequency localizers scans (0 to 2 cpd).

## 8.4 Magnetic Resonance Imaging

### 8.4.1 Scanning

Scanning was carried out on a 3-Tesla Siemens Prisma MR-scanner using an 64-channel receiving SENSE head coil at the Department of Radiology of the University Medical Center Groningen. Foam padding was used for a balance between comfort and reduction of head motion. Four MRI modalities were acquired for each participant: T1w, T2w, Diffusion Weighted Imaging (DWI) and EPI T2*w. Given that the present study aims to evaluate the occurrence of functional reorganization in the visual cortex in response to stimulation, T1w and EPI T2*w images were used.

A T1w (voxel size, $1mm^3$; matrix size, $256 \times 256 \times 256$) scan covering the whole-brain was recorded to chart each participant's cortical anatomy using a magnetization-prepared rapid acquisition of gradient echo sequence (MPRAGE). For functional data acquisition, gradient recalled echo pulse sequences were used to measure T2* BOLD data (TR, 1500 ms; TE, 30 ms; voxel size, $3mm^3$; flip angle 80º; field of view, $84 \times 84 \times 24$). Images were read out using standard EPI sequence. Additionally, a T1w anatomical data set with the same orientation and in-plane resolution as the functional images was acquired for co-registration purposes.

### 8.4.2 Experimental Procedure

Each participant completed two MRI sessions of approximately 1.5h. In the first session the anatomical scan was acquired whereas the second session consisted of the visual field mapping and scotoma localizer experiments. The experimental procedure of the second

session differed between the two groups, i.e., glaucoma and control group, and it is described in the following paragraphs.

#### 8.4.2.1 Glaucoma

For the glaucoma group the second (f)MRI session included the retinotopy and scotoma localizer experiments (table 8.2). Both retinotopy and scotoma localizer experiments were performed first binocularly and secondly monocularly. For the latter the non-dominant eye was stimulated. The retinotopy experiment comprised 9 runs in total, 6 binocular and 3 monocular. One scotoma localizer was performed for each experiment configuration (binocular and monocular). Each run consisted of 136 functional images. During retinotopy experiment scanning, participants were required to perform an attentional task in which they had to fixate a centered dot and to report color changes between red and green via button press. Similarly, while the scotoma localizer stimuli was being displayed, participants were asked to stare at the center of the cross and to press a button each time the cross color changed from black to white or the reverse.

Table 8.2: **MRI protocol for the glaucoma participants.** The complete protocol comprises acquisition of T2w, DWI, EPI T2* resting state and EPI T2* motion localizer images, as well. However, these images are out of the scope of this thesis.

| ***Protocol Glaucoma*** | | | **Number of runs** | **Durantion per run (seconds)** |
|---|---|---|---|---|
| **Structural data acquisition**<br>T1w images | | | 1 | 540 |
| **Functional data acquisition**<br>EPI T2* images | Visual field mapping | LCR binocular | 6 | 204 |
| | | LCR monocular | 3 | 204 |
| | Scotoma localizer | binocular | 1 | 204 |
| | | monocular | 1 | 204 |

#### 8.4.2.2 Aged-matched Controls

In the second (f)MRI session of each healthy participant, the LCR, LCR AS and scotoma localizer experiments were performed (table 8.3). During all the experiments the participants had both eyes open. For both LCR and LCR AS 4 runs were performed. Two scotoma localizers were acquired, one with and another without the AS superimposed to the stimulus. The same fixation tasks as those of glaucoma group were asked.

For both the retinotopic scans (LCR and LCR AS) and scotoma localizer scans a single run consisted of 136 functional images.

Table 8.3: **MRI protocol for the control participants.** The complete protocol comprises acquisition of T2w, DWI, EPI T2* resting state and EPI T2* motion localizer images, as well. However, these images are out of the scope of this thesis.

| ***Protocol Controls*** | | | **Number of runs** | **Durantion per run (seconds)** |
|---|---|---|---|---|
| **Structural data acquisition** T1w images | | | 1 | 540 |
| **Functional data acquisition** EPI T2* images | Visual field mapping | LCR binocular | 4 | 204 |
| | | LCR AS binocular | 4 | 204 |
| | Scotoma localizer | binocular | 1 | 204 |
| | | binocular w/ AS | 1 | 204 |

## 8.5 Data Preprocessing

The raw MRI data from the scanner require a number of preprocessing operations prior to analysis. These operations are meant to either detect and correct for potential artifacts, caused either by the scanner itself or the scanned subject, or to prepare the data for later processing steps.

The main toolbox used for preprocessing and analysis of the fMRI data is the vistasoft software package developed in MATLAB (MathWorks, Natrick, MA) at Stanford University (available at http://white.stanford.edu/software). This software provides the mrVista program and supplementary processing tools. In mrVista, the acquired (f)MRI data were imported, visualized and analyzed.

### 8.5.1 Preprocessing of Anatomical Images

The high-quality T1w structural volumes acquired are of extreme importance as they serve as the spatial reference for the functional applications. All of this data is recorded in the radiological convention or Left-Anterior-Superior orientation (LAS) and is converted to the neurological convention, i.e. Right-Anterior-Superior (RAS) orientation. The orientation of the neurological orientation is the same as the Talairach template coordinate system (or 'atlas') which uses anatomical landmarks of the brain that enable comparison between subjects [84].

Firstly the T1w volumes were realigned to anterior-commissure-posterior-commissure-space (shortly AC-PC space). To perform this realignment, the AC and PC coordinates in the anatomy of each subject were manually set (Figure 8.5). The AC is the origin of the Talairach coordinate system (position 0,0,0) and consists of a white matter tract anterior to the thalamus connecting the two hemispheres. A reference point to the AC point is the PC point which is a few centimeters posterior to the AC and looks like a small fiber tract connecting the cerebellum with the thalamus. The voxel-sizes were then re-sampled to $1mm$ isotropic resolution.

The next preprocessing step consisted on segmenting the brain tissue into gray matter

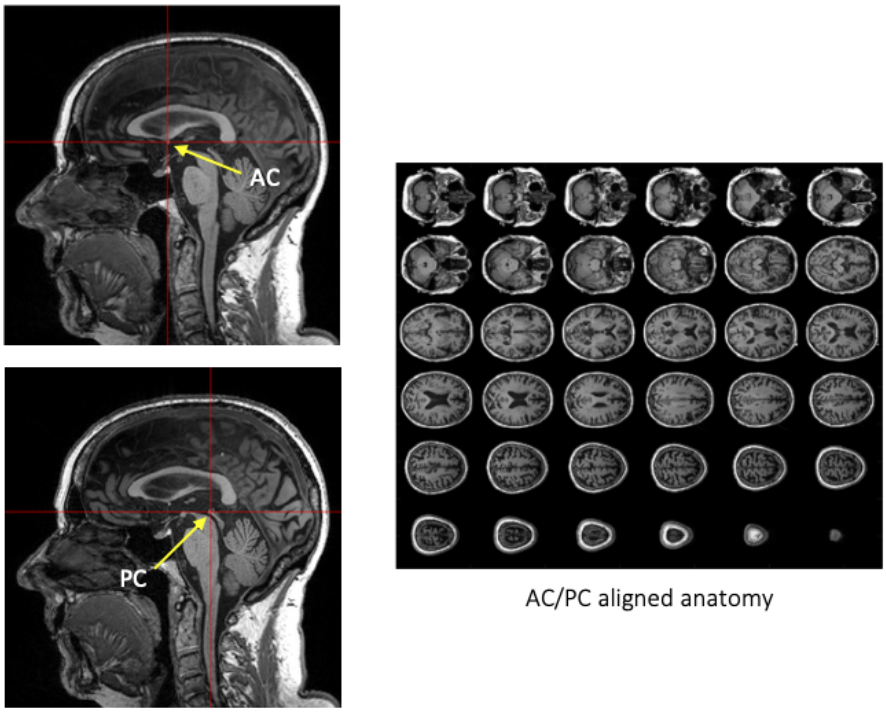


Figure 8.5: **Example of AC/PC alignment.** The left panels point to the location of the AC (top) and PC (bottom) landmarks in the anatomical scan. The right panel shows a variety of the volume's axial slices rotated into AC/PC space.

(GM), white matter (WM) and cerebrospinal fluid (CSF). T1w images already differentiate the mentioned types of tissues by representing them with different intensities which, might suggests that one could simply choose threshold values to identify each component. However, segmentation procedures are not that straightforward. Indeed, to get an accurate brain segmentation is challenging due to three main factors. First, MRI images are noisy which implies that even if the mean intensity of GM labeled voxels is different from the mean intensity assigned to WM labeled voxels, the distribution of their values may overlap. Second, voxels might contain a mixture of different tissue types in varying proportion (*partial volume effect*) which results in voxels with wide range of intensity values and hence classifying those voxels becomes troublesome. There may be non uniformities across the image field of view, such that WM intensity in one region may be closer to that of GM in other region than to that of WM in that other region. Therefore, it is very difficult to label voxels only based on their intensities.

The anatomical image in the AC/PC space was automatically segmented using FreeSurfer [85]. This auto-segmentation algorithm takes the brain image volume and performs, in the first place, motion correction, non-uniform intensity normalization for intensity inhomogeneity correction and removal of non-brain tissues. Once the correction operations are done, the individual cortex surfaces are extracted and registered to surface-based anatomical atlases. This registration procedure is robust to anatomical variability.

Each atlas contains probabilistic information of tissue class automatically estimated from a manually labeled training set. Therefore, by combining the data from the image with the probabilistic atlases, a neuroanatomical label is assigned to each voxel (e.g., if one voxel is in a location that is strongly expected to be GM, the voxel is classified as GM component).

Although FreeSurfer is able to generate a good segmentation, one should always check the result. Thus, hand-edited segmentation was performed in ITK-SNAP [86] to minimize errors, with special attention to the occipital pole (where the visual cortex is located). Manual corrections were conducted in case of thin layers of GM, WM tissues connected and/or unlabelled WM.

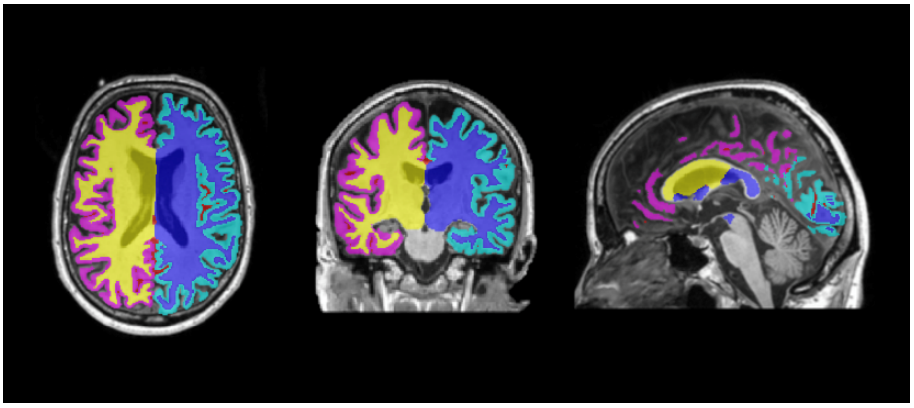

Figure 8.6: **Example of segmented GM and WM of an axial (left), coronal (middle) and sagittal (right) brain slices.** GM and WM is color coded differently regarding the hemisphere. In the left hemisphere GM is represented in pink whereas WM is displayed in yellow. In the right hemisphere GM is represented in light blue whereas WM is displayed in dark blue.

Creating flattened representations of the cortical surface is useful for visualization and analysis of functional activity. For this end, the last step of anatomical preprocessing consisted on the reconstruction of the cortical surface at the GM/WM boundary of the T1w image using *recon-all* (FreeSurfer) and its rendering as a smooth three-dimensional surface, also called mesh (Figure 8.7) [87] to enhance the clarity and visibility of stimulus responses. The latter was done in mrMesh tool (mrVista).

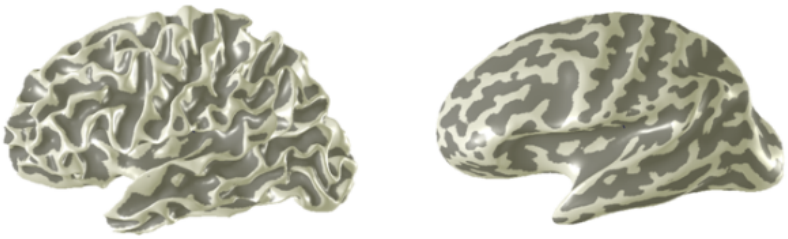

Figure 8.7: **Example of a three-dimensional surface constructed using mrMesh.** The right panel shows a rendering of the reconstructed cortical surface and the left panel shows an inflated version of the same surface. The latter resulted from a smooth level of 1.0 and 210 iterations. Darker gray areas represent sulci (i.e., the grooves) and lighter gray areas represent gyri (i.e., the folds).

### 8.5.2 Preprocessing of Functional Images

The BOLD time-series were detrended with a discrete cosine transform filter with cutoff frequency of $0.001Hz$ to remove baseline drifts, after which they were converted to percent signal change (i.e., $\%\Delta = 100 \cdot [x/\text{mean}(x) - 1]$). The first eight functional images of each run were discarded to avoid start-up magnetization transients.

Head movements resulting from involuntary drift, e.g swallowing and breathing, often referred to as *bulk motion*, may affect activity maps. To minimize this, head movement artifacts both between and within functional scans were corrected. mrVista uses a mutual information motion correction algorithm [88] that performs a rigid-body alignment from each frame within one scan to a reference frame, in order to estimate the relative displacement. The scans with motion artifacts greater than 1 voxel (1 mm isotropic) were discarded. The motion-corrected functional scans where then averaged together to increase the signal-to-noise ratio (SNR).

When it comes to fMRI studies one of the most crucial steps that determines the reliability of the data analysis is the alignment of the functional session to the anatomical reference volume. Given that the collected T1w in-planes have the same FOV as the functional images and the in-planes have higher resolution (1 mm isotropic), aligning these anatomical slices to the reference anatomical volume allows the same transformations to be applied to the functional images. Hence, the functional data is coregistered to the anatomical volume [88]. In mrVista this was performed using rxAlign. In brief, the goal is to obtain an in-plane as close as possible to a prescribed slice of the anatomical volume (Figure 8.8). This is achieved by manually adjusting controls that allow operations such as changing the exhibited slice from the volume, flip the slice in the 3 different planes (axial, sagittal and coronal), rotate and translate it. Subsequently, an automatic algorithm [88] was employed which aims to fine tune the alignment. After an acceptable alignment have been reached, the functional data was interpolated to the segmented anatomical

volume. The described procedure was implemented for every subject and condition.

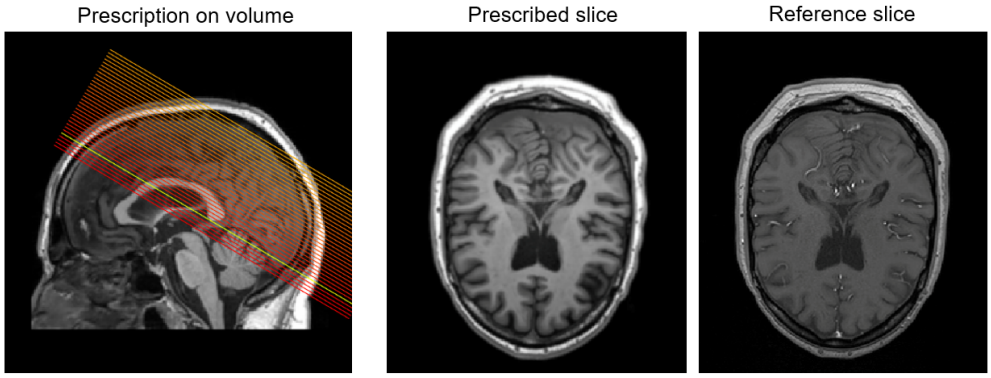


Figure 8.8: **The result of the alignment of the inplane anatomy to the full volume.** The left figure, labelled prescription volume, shows the volume anatomy with a slice prescription overlaid on it (red lines). The middle figure, or prescribed slice, represents how an T1w in-plane is expected to look like given the slice prescription. The in-plane displayed corresponds to the yellow line in the prescription volume figure. Finally, the figure on the right - reference slice - shows the T1w in-plane from the collected data.

## 8.6 Data Analysis

### 8.6.1 Population Receptive Field Mapping

For both used stimuli (LCR and LCR AS) (section 8.3.2), pRF analysis [17] was performed on the functional data using the mrVista Matlab toolbox.

In this thesis, the pRF method, briefly described in chaper 6, was used to map the visual cortex of every subject in each condition. Each cortical position's time-series was predicted using the conventional pRF model - a 2D circular symmetric Gaussian, $g(x,y)$, defined by three parameters, $x_0$, $y_0$ and, $\sigma$,

$$g(x,y) = \exp - \left( \frac{(x-x_0)^2 + (y-y_0)^2}{2\sigma^2} \right) \tag{8.1}$$

where $(x_0, y_0)$ is the center and $\sigma$ is the Gaussian spread (standard deviation) which also represents the size of the pRF. All the parameter units are in degrees of visual angle (°) and stimulus-referred.

The next step consisted on defining the stimulus, $s(x,y,t)$. It was assumed that all parts of the pattern (checkerboard) within the aperture (bar) contribute equally to the fMRI response. This assumption can be made because from literature it is known that fMRI responses to these kinds of stimuli are dominated by contrast edges and, since the checks within the aperture are continuously moving, contrast edges are present throughout the aperture [15]. Thus, the stimulus is defined as a binary indicator function that marks the stimulus position in the visual field over time. To analyse the functional responses to stimuli, two stimulus models were used: one that assumed the presence of the scotoma

- AS model - and one that did not - full field (FF) model (Figure 8.9). LCR was analysed with the FF model whereas LCR AS was analysed with both FF and AS model.

With the pRF model and the stimulus defined, the predicted pRF response was calculated. Because both pRF and stimulus are defined in the common units of visual space, the first step towards predicting the fMRI time series was to combine the position of the pRF in the visual field with the stimulus positions over time. This was done by calculating the overlap, $r(t)$, for each Gaussian

$$r(t) = \sum_{x,y} s(x,y,t)g(x,y) \tag{8.2}$$

The predicted time-series, $p(t)$, was then obtained from the convolution of the pRF response, $r(t)$, with a model of the HRF, $h(t)$ (see Equation 8.3, * denotes convolution). The SPM's canonical difference of gammas was used for the HRF model of each subject.

$$p(t) = r(t) * h(t) \tag{8.3}$$

Assuming a linear relationship between the hemodynamic response and the BOLD activation, a scaling factor $\beta$ was assigned to $p(t)$. $\beta$ accounts for the unknown units of the measured fMRI signal, $y(t)$, and was calculated using the general linear model (GLM) approach (see annexx II) described by the following equation:

$$y(t) = p(t)\beta + e \tag{8.4}$$

where $e$ is the measurement noise.

The optimal pRF parameters were found by minimizing the RSS between the prediction, $p(t)$, and the actual data, $y(t)$.

$$\text{RSS} = \sum_{t} (y(t) - p(t)\beta)^2 \tag{8.5}$$

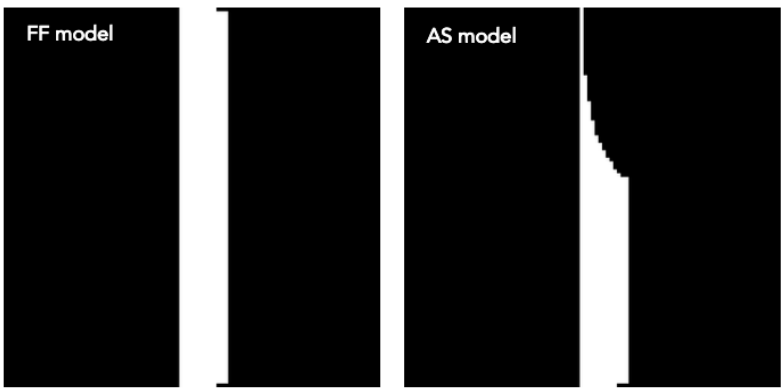


Figure 8.9: **The full field (FF) (left) and artificial scotoma (AS) (right) model used in the pRF analysis.**

### 8.6.2 Regions-of-Interest Definition

V1, V2 and V3 were defined as regions of interest (ROIs) for each subject using the conventional pRF model. Using the model's location parameters $(x_0, y_0)$, values for the polar angle, $\theta$, and eccentricity, $\rho$, can be calculated as follows

$$\theta = \tan^{-1}\left(\frac{y_0}{x_0}\right) \tag{8.6}$$

$$\rho = \sqrt{x_0^2 + y_0^2} \tag{8.7}$$

Eccentricity and polar angle maps were thus projected onto an inflated cortical surface of each hemisphere [87]. The visual areas were then manually delineated from the polar angle maps based on the phase reversal that characterizes the boundaries between adjacent visual areas (see section 2.3.2 and figure 8.10).

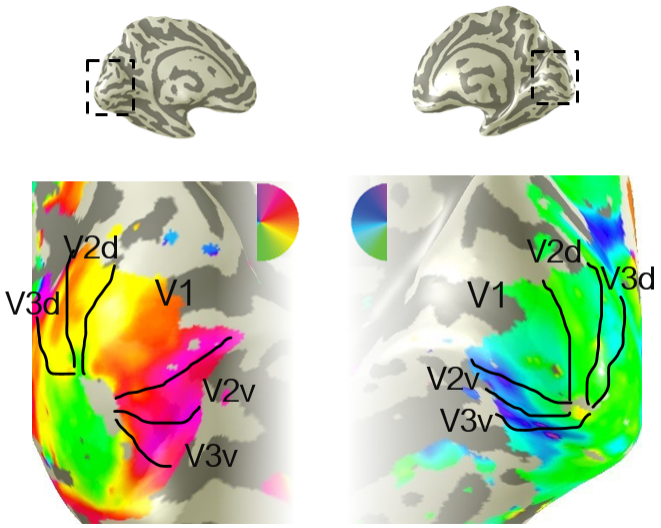


Figure 8.10: **Visualization of polar angle estimates on left and right cortical hemispheres and definition of ROIs.** The dashed black squares on the top panels indicate the occipital region enlarged in the bottom panels. Visual areas V1, V2 and V3 are defined based on the polar angle reversals that define the maps. These reversals are known to establish the boundaries between visual areas [27].

### 8.6.3 Visual Field Coverage Map

Being the main goal of this study to investigate the neuronal mechanisms that underlie PM of the scotomas which, in turn, are present in the visual field, it is also interesting to map the neural stimulus-evoked responses back onto visual space. To this end, we derived visual field coverage maps from the pRF obtained parameters. Additionally, due to limitations in the pRF approach, we used a more recent methodology to upgrade our results.

#### 8.6.3.1 pRF-based Visual Field Coverage Map

As described in the section 8.6.1, the pRF parameters are derived from modeling the responses of each voxel. Therefore, a visual field coverage map can be estimated by projecting the pRF responses obtained for the ROIs onto the visual field. This was done for area V1 of each subject and condition. Each coverage plot shows the sampling density of the visual cortex. Only pRF estimates with a variance explained equal or higher to 0.15 were included in the analysis. Across area V1 of each hemisphere, the pRF models (2D Gaussians; see equation 8.1), weighted by their respective variance explained were summed. By weighting the model by its variance explained (8.11A) we take into account the responsiveness of the neuronal populations within a voxel and we reduce effect of pRFs resulting from noise signals. A V1 visual field coverage plot was then created for each individual observer that combined pRFs estimates for the left and right hemispheres. This resulted from the averaging the hemispheres' sum of estimates in the ROI (Figure 8.11B-D). The described procedure is given by the following equation ($*$ denotes convolution)

$$pRF = \frac{\sum_{k}^{m}\sum_{j}^{n}(pRF_{kj} * V_{kj})}{m} \tag{8.8}$$

where $pRF$ represents the clustering of all models from both hemispheres, $pRF_{kj}$ is the model of the $j$-th voxel ($j = 1,...,n$) in the $k$-th hemisphere ($k = 1,...,m$) and, $V_{kj}$ its associated explained variance.

Locations in the visual field with higher sampling density are expressed in shades of yellow, while areas processed by a lower sampling density of pRFs is displayed in blue. However, one can note in figure 8.11D that the highest sampling density roughly lies on the centre of the visual field. This is a consequence of the cortical magnification (see section 2.3.2). To correct for this general tendency and be able to more straightforwardly recognize differences in pRFs distributions between observers, the sum of the several pRFs within the ROI was divided by the sum of the pRFs without being weighted by explained variance. An example of a resulting map is displayed in figure 8.11E. This procedure was done for the other ROIs (V2 and V3) however, as the resulting maps did not differ significantly from the one from V1, only the latter was considered for analysis purposes.

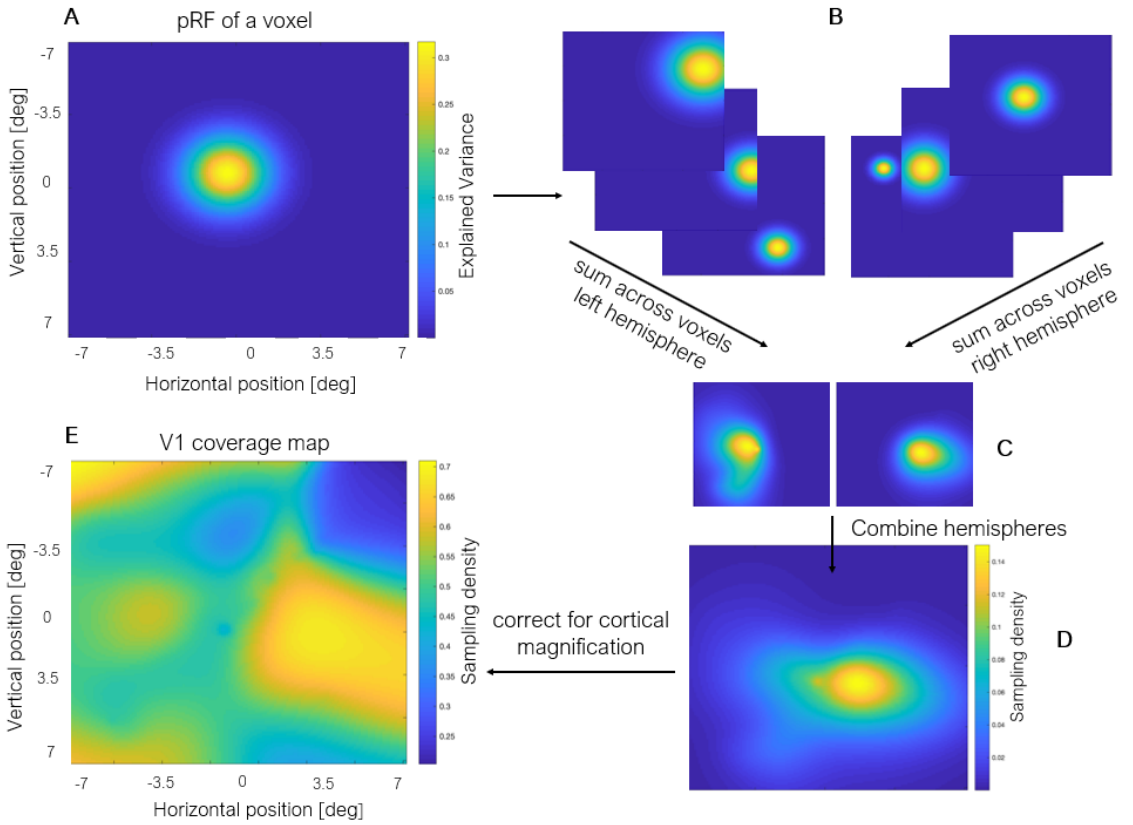


Figure 8.11: **pRF-based V1 coverage map framework. (A)** pRF model (2D Gaussian) weighted by explained variance of a voxel within V1. **(B-C)** The resulting pRFs were summed across voxels per hemisphere and then combined to produce a representation of the visual field in the primary visual cortex **(D)**. **(E)** To correct for the cortical magnification phenomenon - higher sampling density processing central visual field - the weighted summed pRFs within the ROI was divided by the unweighted sum of the same pRFs. Only voxels for which the pRF explained at least 15% of the time-series variance were included in the analysis.

#### 8.6.3.2 Micro-probing-based Visual Field Coverage Map

The pRF method is a well-established technique for deriving the location and size of the region in the visual field that elicits a BOLD response from a voxel. However, because of fMRI limited spatial resolution, it only assesses the central tendency of all neuronal populations within the voxel. Additionally, the method requires making a priori assumptions about spatial and temporal properties of the pRF which limits the ability to reveal atypical pRF features and subpopulations. Having this in mind, advanced approaches, such as Micro-Probing (MP) [89], have been developed to overcome the pRF drawbacks and thus, enhance our understanding of visual processing and cortical organization.

The MP enables more fined-grained properties of neuronal populations and subpopulations to be captured by a voxel. By means of a "microprobe" it samples every location

within the visual field. Like the pRF models, each of these microprobes sample the aggregate response of neuronal subpopulations, but they do so with much higher resolution. As a result, for each voxel, a probe map is generated (figure 8.12A) that represents the density and explained variance for all probes.

Each probe was modeled as a 2D gaussian defined by three parameters,$\hat{x}$, $\hat{y}$, $\sigma$,

$$probe = \exp - \left( \frac{(x-\hat{x})^2 + (y-\hat{y})^2}{-2\sigma^2} \right) \tag{8.9}$$

where $(\hat{x}, \hat{y})$ is the center and $\sigma$ the spread of the Gaussian. The latter is set to a narrow constant value (0.01 degrees). All three parameters are in units of visual angle (degrees).

The center of the probe $(\hat{x}, \hat{y})$ was defined using 2 latent variables, $l_\rho$ and $l_\theta$, that represent the radius and angle of the pRF center, respectively. The probe position of a RF in polar coordinates is given by:

$$\rho = r * NCDF(l_\rho, 0, 1) \tag{8.10}$$

$$\theta = 2\pi * NCDF(l_\theta, 0, 1) - \pi \tag{8.11}$$

where $r$ is the radius of the stimulates visual field, in degrees, and $NCDF$ corresponds to the normal cumulative distribution density function (* denotes convolution).

In order to incorporate *a priori* biological information about the distribution of the probes across the visual field, each of the latent variables, $l_\rho$ and $l_\rho$, was assigned to a prior probability distribution, or simply *prior*. As done in previous work [90], these priors were defined as normal distributions, $N(0,1)$. Having $\rho$ and $\theta$, the probe position was then converted back to cartesian coordinates through the following couple of equations

$$x = \rho * \cos\theta \tag{8.12}$$

$$y = \rho * \sin\theta \tag{8.13}$$

The aim of the MP is to probe every position in stimulus space. To do so, MP uses the iterative Markov Chain Monte Carlo (MCMC) procedure to speed up the process and hence reduce computation time. According to this procedure, the next position of the probe $(i+1)$ was pseudo-randomly selected. At each iteration, a probe position, in polar coordinates $(\rho, \theta)$, was fitted. The probe fitting procedure used is based on the pRF approach [17] (Figure 8.12C). First, the predicted response of the voxel, $p(t)$, was obtained from the overlap between the probe and the stimulus at each point in time, $s(x, y, t)$:

$$p(t) = \sum_{x,y} s(x, y, t) probe(x, y) \tag{8.14}$$

Following this, we convolved $p(t)$ with an HRF to account for the delay in the hemodynamic response. Finally, assuming a linear model of the fMRI response, we determined the error at each time point, $e_t$ between the prediction and the actual data using a least square fit.

Then we calculated the likelihood, $l_t$, associated to $e_t$. By assuming that $e_t$ is evenly distributed, one can estimate the mean, $\hat{\mu}$, and standard deviation, $\hat{\sigma}$. Therefore, with these two estimates we calculated the total likelihood, $L_t$, which accounts for the contributions of the priors of $\rho$ and $\theta$.

$$l_t = \log(N(-|e_t|, \hat{\mu}, \hat{\sigma}), \rho, \theta) \tag{8.15}$$

$$L_t = \sum_t (l_t) + \log(prior_\theta) + \log(prior_\rho) \tag{8.16}$$

The likelihood of the current iteration was compared to that of the last accepted iteration. For this analysis, the acceptance ratio, $A_r$, was computed and then compared to the *accept* value, i.e. probability of random acceptance. The accept was defined as a normal distribution, $N(0,1)$. In case the $A_r$ was superior to the accept, the latent values were updated. Based on the new $l_\rho$ and $l_\theta$ a new probe was defined and thus a new iteration started.

$$A_r = \exp(L_{tcurrent} - L_{tlastaccepted}) \tag{8.17}$$

Once the iterative procedure was over, a probe map was obtained for every voxel within area V1. Each of these maps consists of the projection onto the visual field of all the probes, weighted by explained variance, captured by a voxel. The probe map was then converted into a heat map. Similarly to the pRF-based approach described in the previous section, the heat map of all voxels were clustered and averaged across hemispheres. As a result, a coverage map of V1 was generated.

As the probe maps were already weighted by explained variance, unlike what was done in the pRF-based approach, we corrected for cortical magnification phenomenon by dividing each participant's coverage map by the average coverage map of the control participants in unmasked condition.

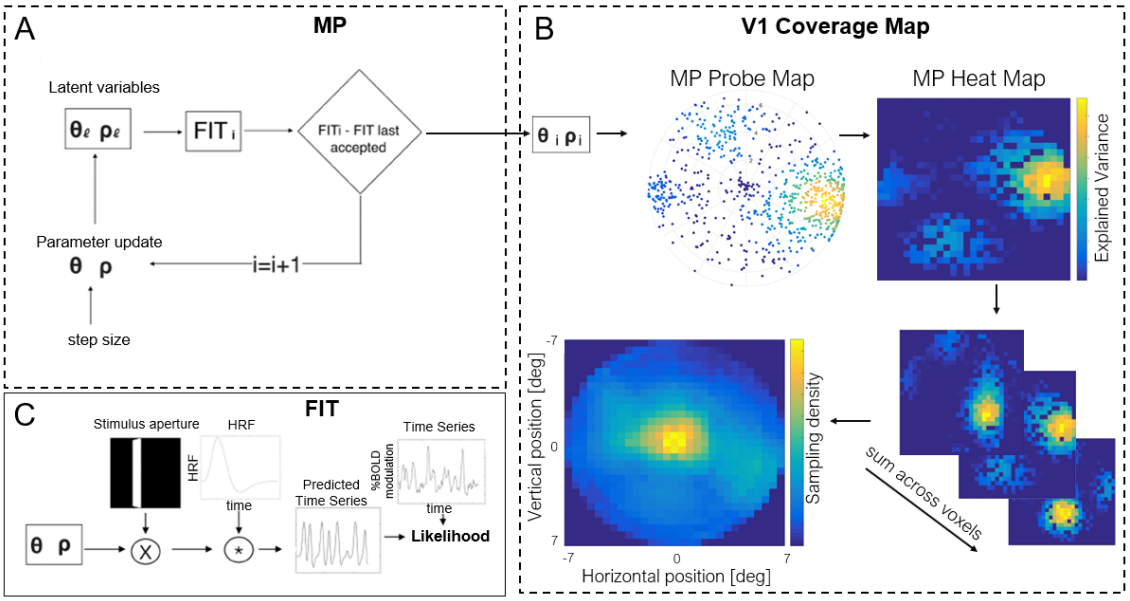


Figure 8.12: **Overview of microprobing-based coverage map framework. (A)** MP: creation of a probe map. **(B)** V1 Coverage Map: generation of a visual field coverage map based on the probe maps. **(C)** FIT: Probe fitting procedure based on the conventional pRF approach [17]. Adapted from [89].

### 8.6.4 Scotoma Projection Zone (SPZ) Definition

The SPZ, i.e. the cortical area corresponding to the scotomatic region of the visual field, for each patient and, ergo, each aged-matched control under AS condition, was defined through two methods: 1) based on the scotoma localizer results and 2) according to the perimetric outcome measures.

#### 8.6.4.1 Definition of the SPZ based on the Scotoma Localizer

The SPZ was defined using the scotoma localizer by contrasting the AS and background stimulation. The two conditions were entered as predictors, after convolution with a HRF, in a standard GLM (see annex II) as implemented in MRvista. The SPZ was defined as the voxels for which the contrast resulted in a $t$ value larger than 4. Figure 8.13 shows the results of the SPZ localizer projected on an inflated brain mesh (blue denotes the SPZ).

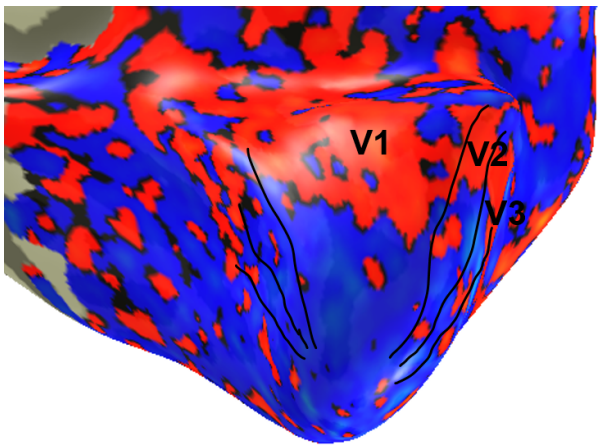


Figure 8.13: **Definition of the SPZ based on the localizer.** Projection on an inflated brain mesh of the scotoma localizer GLM results. Here, blue represents the SPZ. The black lines delineate the visual areas.

#### 8.6.4.2 Definition of the SPZ based on Perimetry

HFA, described in section 8.2, allows the assessment of the visual field measuring the bilateral contrast sensitivity distribution (in dB). The SPZ was defined by taking each ROI's voxels (thresholded to 0.15 of the explained variance) whose pRF was completely contained within the area of the visual field defined by contrast sensitivity values <=-13 dB. This is the approximated value from which an observer is considered unable to perceive a visual stimulus thus assembling to that location an area deprived of input - the scotoma.

The first step towards delineating the SPZ was to obtain a binocular HFA numerical chart. The mean deviation (MD) sensitivity values - depressed vision for each point when compared with aged-matched controls - encompassed in the inner 7 degrees of visual angle (stimulus maximum radius) were retained for each eye. For each location the highest value between left and right eye was selected. The resulting matrix, translating the binocular visual field, was resized to the scale of the visual field coverage map described in the previous section and overlaid on top of it for visualization purpose.

As one can observe from the coverage map of a patient represented in figure 8.14, the top right quadrant of the visual field is assigned with values ranging from -21 dB to -33 dB which are quite low compared to the remaining areas and plus, are below -13 dB. Therefore, for this patient the SPZ was defined by the pRF estimates collapsed into that quadrant. However, defining the SPZ was not straightforward for the whole glaucoma population because first, some patients did not present contrast sensitivity under -13 dB and secondly even if they did the values were scattered across the visual field. For the cases when values equal or under -13 dB were absent, the SPZ was defined by the pRF estimates that fell in the area of the visual field assigned with the minimum contrast

sensitivity value among the grid. When the lowest values were scattered, the SPZ resulted from combining all these regions.

In addition to the SPZ, a 1 degree border surrounding the scotoma was defined and further translated into cortical coordinates. The remaining visual field was labeled as the peripheral area of the scotoma and the voxels whose pRF was located there were grouped to form another cortical region. The described procedure was employed for the age-matched controls taking the same restriction of visual field into scotoma, border and periphery as the assigned patients. The goal was to compare at region-level the pRF dynamics between disease and presence (and absence) of an AS in the control individuals.

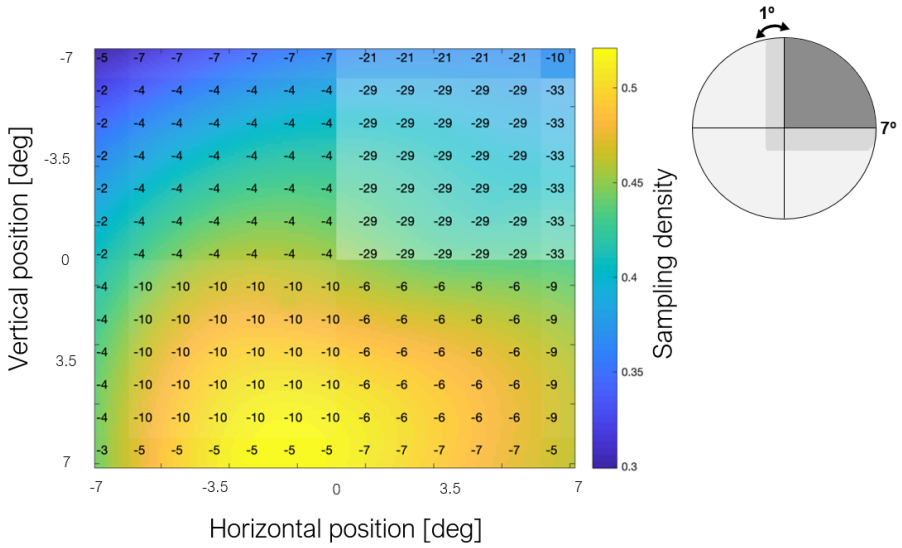


Figure 8.14: **V1 coverage map for a glaucomatous subject with HFA numerical grid overlaid.** The HFA values were assigned to a grayscale in order to create shades on the coverage map that become increasingly opaque with the decrease in contrast sensitivity This is was done for visualization purpose. On the top right of the figure there is a sketch of the visual field indicating the location of the defined artificial scotoma (dark gray), its border (mid gray) and remaining peripheral area (light gray).

### 8.6.5 Statistical Analyses

As in previous work [11, 17] data was thresholded by retaining the pRF models that explained at least 15% of the variance in the BOLD response and that had an eccentricity in the range of 0-7 degrees, for all conditions (i.e., LCR and LCR AS). The pRF estimates maps projected on the inflated meshes were obtained using a explained variance threshold of 0.1.

A two-sample $t$-test was used to evaluate the significance of the difference in pRF size cumulative distributions between the patients and controls under masked visual field that, henceforth will be referred to as AS-controls to distinguish from the unmasked condition. Repeated measures two-way analysis of variance (ANOVA) with ROI and condition (LCR and LCR AS) were performed to determine whether the pRF size inside, in the border,

and in the peripheral area of the scotoma in the patients differed significantly from that of the AS-controls. Ultimately, a two-sample Kolmogorov-Smirnov test was employed to compare the pRF center locations between groups.

All statistical analyses were performed using MATLAB (version 2016b; Mathworks, Natick, MA, USA). A $p$-value of 0.05 or less was considered statistically significant.

Chapter 9

# Results

Cortical responses evoked by luminance-contrast defined stimuli were measured in 20 individuals with glaucoma (see Table 9.1), all diagnosed with POAG, and 6 aged-matched controls with normal (or corrected to normal) vision. Overall the individuals with glaucoma showed reduced VA (glaucoma, mean VA right eye=0.9, left eye=0.8; controls, mean VA right eye=0.93, left eye=0.97) and abnormal visual field scores, as measured by MD using HFA, compared to age-correct normative database (glaucoma, mean MD right eye=-7.4 dB, left eye=-16.4 dB; controls, mean MD right eye=0.3 dB, left eye=-0.2 dB). All participants were under standard medical care for glaucoma to maintain IOP values within normal physiological ranges (< 21 mmHG), except 1 participant (#15) who still had elevated IOP. The RNFL thickness values were, in general, abnormal in comparison to age-corrected normative database (glaucoma, mean RNFL right eye=72.6$\mu$m, left eye=68$\mu$m; controls, mean RNFL right eye=99.2$\mu$m, left eye=93.8$\mu$m).

In order to investigate the functional properties of the early visual cortex (V1-V3) during PM of the scotomas in glaucoma, we first detailed the pRF properties of the visual field maps. Further, we produced coverage maps of the visual field processed by the primary visual cortex (V1), by means of pRF- and MP-based approaches, to topographically depict the visual field defects. These analyses were performed for each of the individuals in the two groups, those with glaucoma (the patient group) and the aged-matched controls (the control group).

Table 9.1: **Summary of glaucoma participants in the study.** VA, IOP, Visual field data, and RNFL thickness are shown for left (oculus sinister) and right (oculus dexter) eyes. VA indicates visual acuity; logMAR, logarithm of the Minimum Angle of Resolution (Scale of vision loss. Normal vision is represented by values <= 0); IOP, intraocular pressure; RNFL, retinal nerve fiber layer; MD, mean deviation. Gray lines highlight the patients whose visual field defects were simulated in an aged-matched control.

| | | | | | | | | Visual Field (dB) | | | |
|---|---|---|---|---|---|---|---|---|---|---|---|
| | | | | VA (logMAR) | | IOP (mmHg) | | OD | OS | RNFL ($\mu$m) | |
| No | Diagnosis | Sex | Age | OD | OS | OD | OS | MD | MD | OD | OS |
| 1 | POAG | F | 73 | 0.2 | 0.2 | 10 | 13 | -21.24 | -16.42 | 120 | 125 |
| 2 | POAG | M | 68 | 0.8 | 0.1 | 14.5 | 16 | -30.54 | -1.12 | 79 | 66 |
| 3 | POAG | M | 71 | 0.6 | 1.2 | 10.3 | 9.7 | -5.01 | -1.11 | 80 | 88 |
| 4 | POAG | F | 76 | 0.6 | 0.6 | 10.3 | 11 | -23.08 | -18.43 | 56 | 58 |
| 5 | POAG | F | 84 | 0.7 | 1 | 12 | 13 | -11 | -7.5 | 54 | 64 |
| 6 | POAG | M | 67 | 1.2 | 1.2 | 16 | 18 | 0.3 | 0.95 | 71 | 73 |
| 7 | POAG | F | 81 | 0.4 | 0.8 | 13.3 | 12.3 | -3.67 | -21 | 91 | 82 |
| 8 | POAG | M | 85 | 0.8 | 1 | 14.3 | 13.7 | -0.09 | -12.11 | 78 | 64 |
| 9 | POAG | F | 65 | 0.9 | 0.5 | 10.7 | 12.3 | -2.56 | -6.14 | 76 | 54 |
| 10 | POAG | M | 69 | 1 | 1.2 | 11.7 | 11.3 | -8.37 | -14.72 | 63 | 66 |
| 11 | POAG | M | 73 | 1 | 0.9 | 14.3 | 15.7 | -2.12 | -2.05 | 59 | 60 |
| 12 | POAG | M | 71 | 1 | 0.7 | 14.7 | 10 | -12.66 | -4.7 | 63 | 49 |
| 13 | POAG | M | 55 | 0.8 | 0.7 | 16 | 16 | -4.24 | -15.29 | 66 | 60 |
| 14 | POAG | F | 77 | 1.2 | 1.2 | 19 | 9.7 | -3.52 | -12.6 | 75 | 72 |
| 15 | POAG | M | 62 | 1.5 | 0.9 | 17.3 | 25.3 | 0.52 | -4.32 | 86 | 63 |
| 16 | POAG | F | 71 | 1 | 0.9 | 14 | 14.7 | -2.25 | -1.1 | 60 | 71 |
| 17 | POAG | F | 63 | 1 | 1.2 | 12 | 8 | -6.36 | -4.56 | 69 | 72 |
| 18 | POAG | F | 59 | 0.9 | 1.0 | 9 | 11.3 | -0.92 | -23.9 | 86 | 56 |
| 19 | POAG | F | 60 | - | - | 13.7 | 11.7 | -9.45 | -6.11 | 50 | 60 |
| 20 | POAG | M | 60 | 2 | 0.6 | 14.7 | 16 | -2.36 | -28.11 | 71 | 57 |

## 9.1 Changes in BOLD signals

Prior to model-based analysis we investigated the differences in the BOLD signal between the two groups in study. In figure 9.1, the average standard deviation of the BOLD signal, here used as a measure of signal modulation, as a function of early visual areas is presented for patients' ($n$=20) and controls' group ($n$=6). Remarkably, the stimulus-induced signal variation (standard deviation) was smaller for the patients but grossly stable over ROIs. The superimposition of an AS onto the visual field of the controls had not largely influenced the signal variation, exhibiting only a slight decrease from that of the unmasked condition (FF). The latter was observed in particular for area V3.

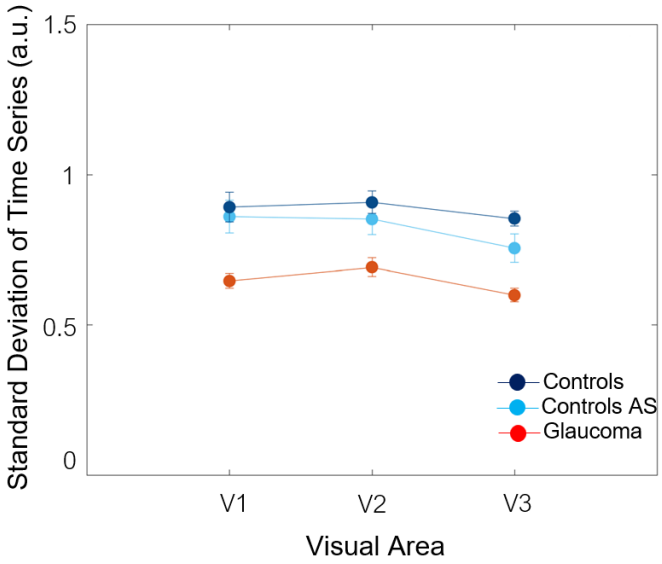


Figure 9.1: **Standard deviation of the mean time series (in arbitrary units) for 3 different ROIs for patients (red) and controls with and without AS (light and dark blue, respectively).** Average results for 20 patients and 6 controls, 2 hemispheres each. Error bars indicate the standard error of the mean over hemispheres.

## 9.2 Visual Field Maps and pRF Properties

Figure 9.2 shows the backprojection of the visual field map properties (eccentricity, polar angle and size) obtained using pRF mapping onto the inflated left hemisphere of a patient (P10) and respective control with FF and AS stimulation. The visualization of the polar angle estimates showed the expected activation patterns with no apparent differences between patient and control. The patient's eccentricity map, by contrast, suggested that a larger portion of the cortex responds to central visual stimulation when compared with the control.

When visual deficits were simulated in the control the response distributions of pRF estimates got altered from what observed in the normal condition (FF). The presence of an AS in the stimulus removed significant responses from the occipital pole and the activated area of the parafovea (blue pixels) was shrunk. Despite such changes, the left hemisphere was represented as an orderly eccentricity and polar angle map.

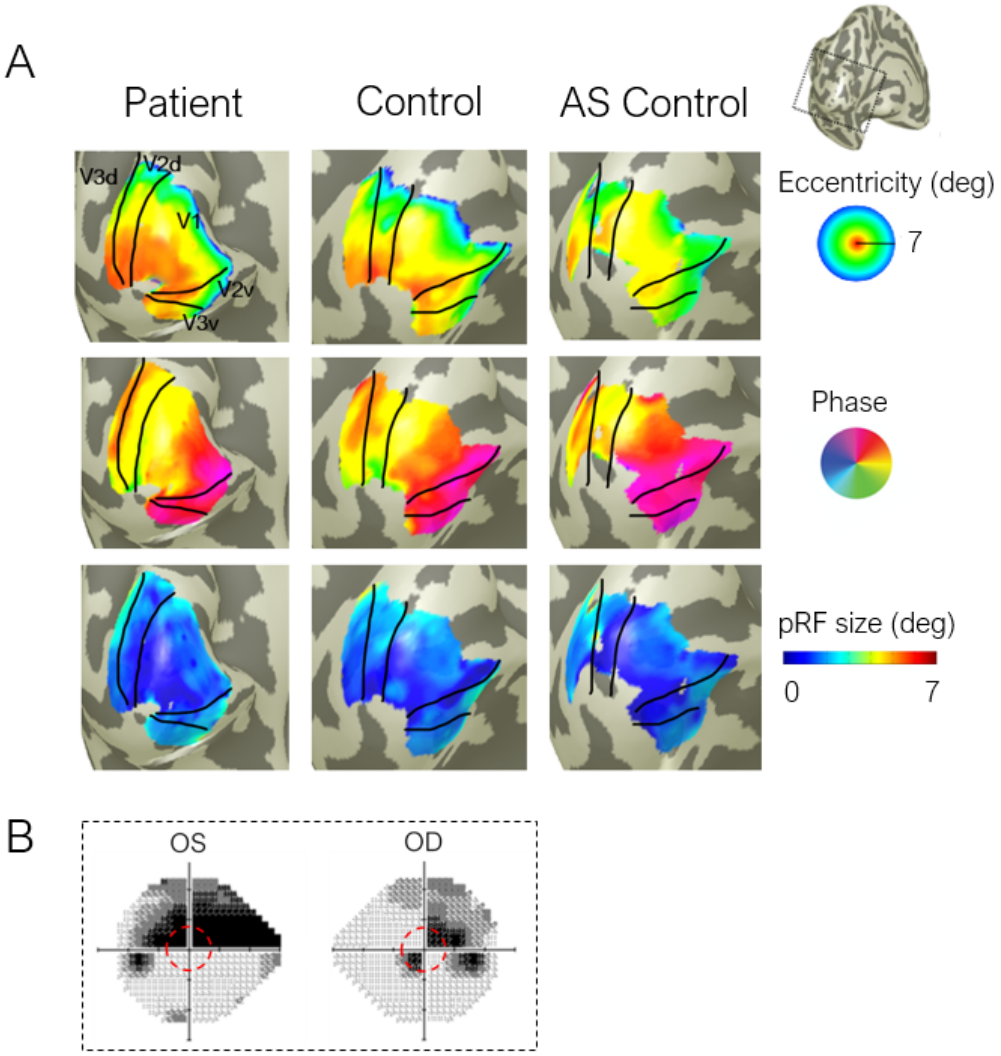


Figure 9.2: **Visualization of VFM based estimates using pRF for a glaucomatous subject and the age-matched control obtained with a luminance-contrast defined stimuli. (A)** Top, middle and lower panels show eccentricity, polar angle and size maps, respectively, superimposed on left inflated occipital poles (cortical location indicated by the black rectangle on the figure's top right) for a P10 and respective control. The displayed pRF maps for the AS condition were obtained by the AS model. In all cases, the explained variance threshold was set to 0.1. The black lines denote the visual areas boundaries. An algorithm was used to restrict the visualization of the pRF estimates to the ROIs. **(B)** Grayscale visualisation graphics of numeric contrast sensitivity (in dB), measured by HFA, for left (oculus sinister) and right (oculus dexter) eyes of patient P10. The insets outline the simulated area of the visual field (7 degrees of visual angle).

The pRF maps presented above consist of a visualization tool of the model parameters' distribution on the cortical surface, from which information can be extracted. However, to compare pRF properties between patients and controls further quantitative analyses need to be employed.

Figure 9.3 depicts the pRF size as a function of eccentricity for patients with glaucoma (binocular and monocular) and aged matched controls (FF and AS stimulation). It is evident that the pRF size increases with eccentricity (table 9.2) and that this relation increases with the visual hierarchy, i.e. from lower to higher visual areas. These features are well known from electrophysiological measurements and have been demonstrated in previous pRF analyzes [14, 91–94]. In general, the pRF sizes determined based on the LCR analyses for the glaucoma group were somewhat larger than those determined for the controls, even in the presence of an AS. There was a significant interaction between condition and eccentricity ($F$=3.07, $P < 0.005$) and condition and ROI ($F$=3.92, $P < 0.05$), indicating the difference in size is larger for higher order areas.

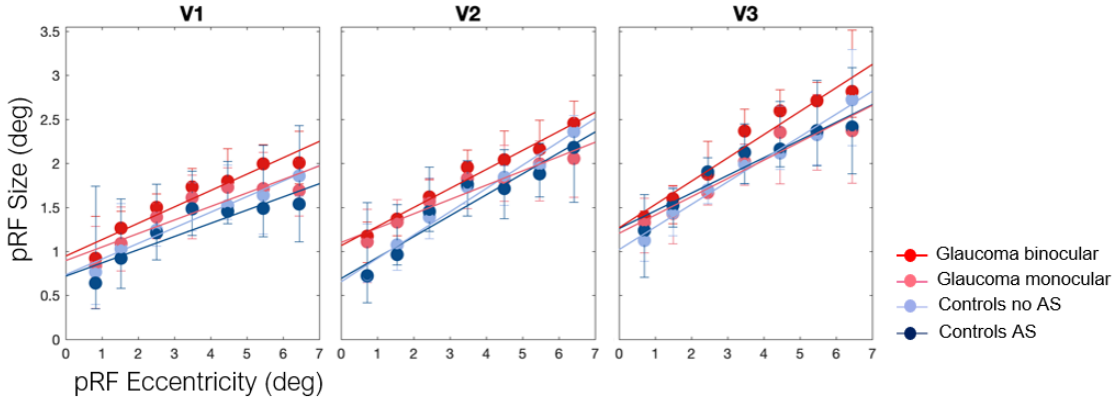


Figure 9.3: **Average voxel-wise pRF size plotted as a function of pRF eccentricity for 3 different ROIs.** Eccentricity was binned in bins of 1 degree of visual angle. Each bin shows the average results for 6 controls for the unmasked and masked conditions (represented in light blue and dark blue, respectively) and 20 glaucoma subjects for both binocular and monocular conditions (represented in red and light pink, respectively), 2 hemispheres each. Error bars indicate the 5% and 95% confidence intervals.

Table 9.2: **Statistical analysis of the relation between pRF size and eccentricity.** The correlation coefficients were computed for all voxels in the ROIs for which the best-fitting pRF models explained more than 15% of the time-series variance.

| | **Glaucoma binocular** | | **Glaucoma monocular** | | **Controls** | | **AS Controls** | |
|---|---|---|---|---|---|---|---|---|
| **ROI** | $r^2$ | $p$–value | $r^2$ | $p$–value | $r^2$ | $p$–value | $r^2$ | $p$–value |
| **V1** | 0.9089 | 0.0411 | 0.8738 | 0.0022 | 0.9617 | 0.00251 | 0.8676 | 0.0229 |
| **V2** | 0.8869 | 0.0185 | 0.8792 | 0.0001 | 0.9886 | 0.0072 | 0.9298 | 0.0367 |
| **V3** | 0.8392 | 0.0489 | 0.8474 | 0.0153 | 0.8973 | 0.0025 | 0.9592 | 0.0332 |

pRF size was plotted as a function of explained variance (EV), as shown in figure 9.4. For the glaucoma population, pRF size was roughly constant across EV, suggesting

an independence on EV. For the controls, however, a potential dependence (increase of the pRF size with EV) on EV was observed for areas V1 and V2 for both masked and unmasked conditions.

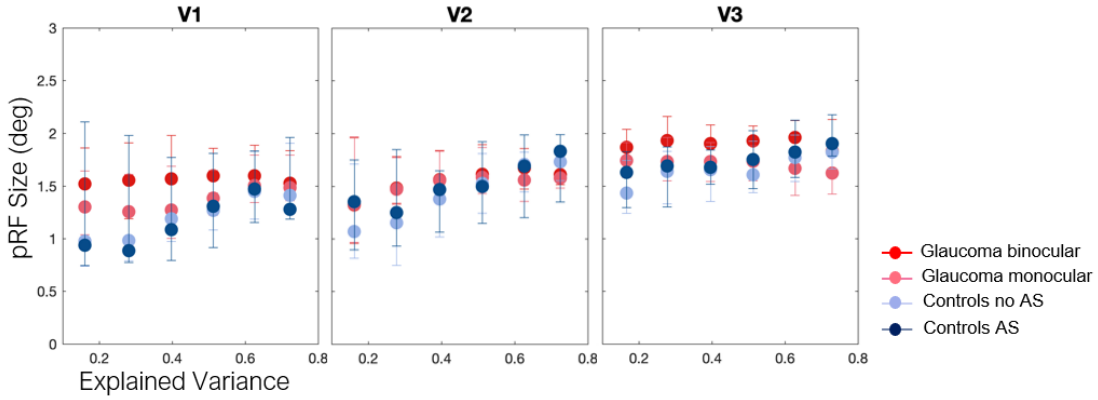


Figure 9.4: **Average voxel-wise pRF size plotted as a function of explained variance (EV) for 3 different ROIs.** EV was binned in bins of size 0.1. Each bin shows the average results for 6 subjects, for the control population, and 20 subjects for the glaucoma population responses, 2 hemispheres each. Error bars indicate the 5% and 95% confidence intervals.

Figure 9.5A shows estimated eccentricity relationship between the pRFs obtained using the unmasked and masked conditions for the control group ($n$=6). There is a good correlation between the pRF locations in both conditions (FF and AS) for all the visual areas tested - eccentricity estimates lie well within the black dotted line of unit slope. This indicates that the presence of the masked stimulus does not result in significant shifts in position of the pRFs. Figure 9.5B shows correlation between the eccentricity properties obtained using the binocular and monocular conditions for the patient group ($n$=20). While for foveal and parafoveal regions there is a good overlap between the location of both conditions, the voxels whose pRFs are located in the peripheral visual field seem to shift their position towards less eccentric locations when the glaucomatous eye perform the task. In visual area V3 this effect is more accentuated compared to V1 and V2.

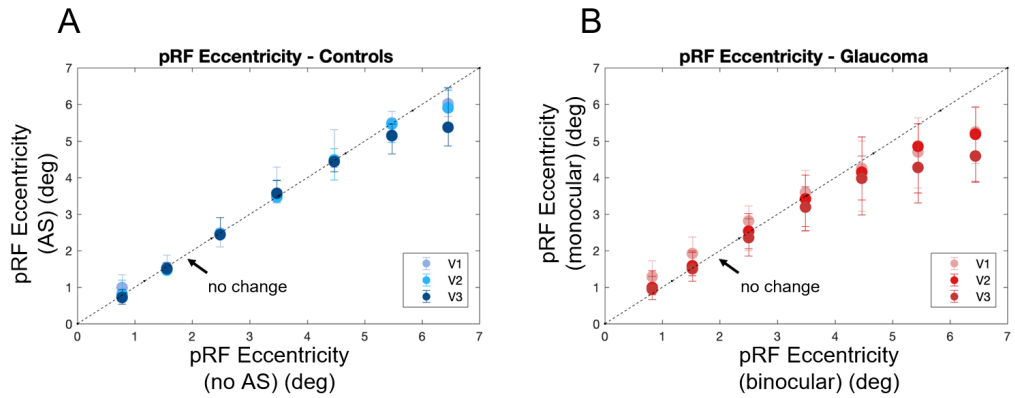


Figure 9.5: **Comparison of voxel-wise eccentricity for masked and unmasked visual field in the control population and, for monocular and binocular performance in the glaucoma population, for 3 different ROIs.** The left plot represents the effect of the AS stimulus on pRF eccentricity of the group of age-matched controls. pRF eccentricity in unmasked condition is given by the x-axis. The panel on the right shows the same type of plot but for the glaucoma population and represents the result on pRFs position when the subjects viewed the visual stimulus monocularly. The binocular retinotopy-assigned pRF eccentricity is given by the x-axis. The dashed black lines indicate the predicted result if voxels responded the same way in both conditions. Average results for 6 aged-matched controls and 20 glaucomatous subjects, 2 hemispheres each. Eccentricity was binned in bins of 1 degree of visual angle. Error-bars represent the 5% and 95% confidence intervals.

### 9.2.1 Enlargement of pRFs in glaucoma

The visual field maps and relationship between size and location of the pRFs reported in the previous section gave a hint that BOLD responses in glaucoma might be driven by neurons with displaced and/or large receptive fields that extend into areas of spared retina. To investigate these potential 'ectopic' neuronal populations, we examined the results further with the AS controls as the baseline measure. Consequently, we had to employ the following described analyses only with 5 patients.

Hence we compared the changes in pRF size between the patients ($n$=5) and AS-controls ($n$=5) by plotting the cumulative distribution of the pRF sizes in the early visual cortex for both groups (figure 9.6). Only the patients whose scotomas were masked onto the visual field of a control were taken into account. We report an overall increase in pRF size with the rise in visual hierarchy which translates into a progressive shift towards the right of the cumulative distribution curves. It is noteworthy that distributions from subjects belonging to the same group remain close to one another and thus, controls and patients are straightforwardly distinguishable. Indeed, the groups' average logistic functions were found to be significantly different at the 80% point (dashed black line figure 9.6) (V1, $t$ = 3.47, $P$ = 0.0528; V2, $t$ = 2.91, $P$ = 0.0490; V3, $t$ = 3.21, $P$ = 0.0314).

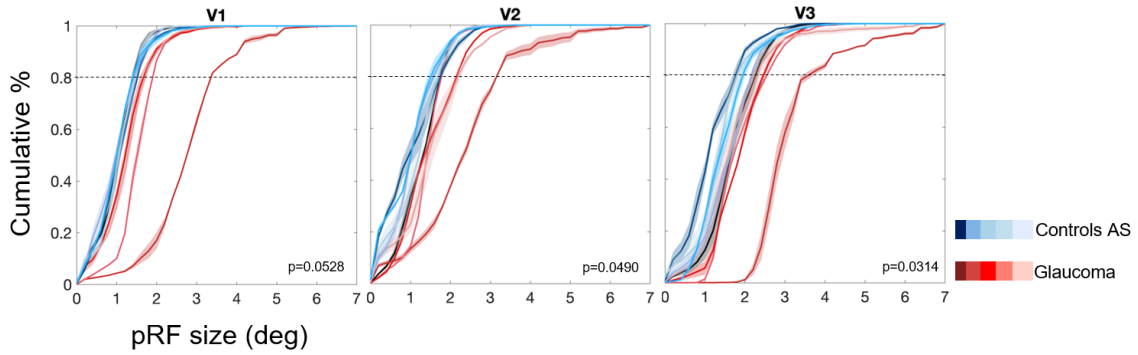


Figure 9.6: **Quantitative comparison of cumulative percentage of pRF size for glaucoma and control groups.** Cumulative percentage of the pRF size for the glaucomatous subjects ($n$=5), represented in different shades of red, and the age-matched controls ($n$=5), represented in different shades of blue. The pRF size changes in the latter are in response to an artificial scotoma. The shaded area of each distribution represents the 5% and 95% confidence interval. The $p$-values on the bottom right of the graph show the significance level between the average fit distribution of each group.

To improve the specificity of our measurements, we then compared the pRF size dynamics between groups - glaucoma and AS-controls - at the region level, that is to evaluate whether the differences were more pronounced inside, on the edge or in the surrounding areas of the scotoma. Taking the voxels whose pRF was located located either inside, on the edge or outside the SPZ, for each observer, ROI and region, pRF size was averaged over the eccentricity bins of 1 degree. Then, for each pair patient-control and bin-wise the average pRF size across hemispheres of the patient was subtracted to the one of the aged-matched control. The differences were subsequently grouped across pairs and are presented in the graphic of figure 9.7A. We report larger pRF sizes in the glaucoma group for the three regions in V1 to V3 (positive differences). Note that except in V2 the larger pRFs differences are found in scotomatic region and the smallest in the periphery. A comparison across visual areas and region of the visual field revealed that the pRF size changes significantly between regions ($F$=5.37, $P$<0.05) and with visual area ($F$=9.76, $P$<0.0001). The interaction between the two factors was not significant ($F$=1.61, $P$=0.17).

The aforementioned analysis was also performed for the control group to determine the effect of AS on pRF size. Thus, pRF size difference between unmasked and masked condition was obtained for the three defined regions and throughout visual hierarchy. The difference was first calculated voxel-by-voxel at region level for each subject and further averaged across subjects. There was no significant difference of pRF sizes for either inside, on edge or outside of the SPZ in V1, V2 and V3 between conditions (figure 9.7B).

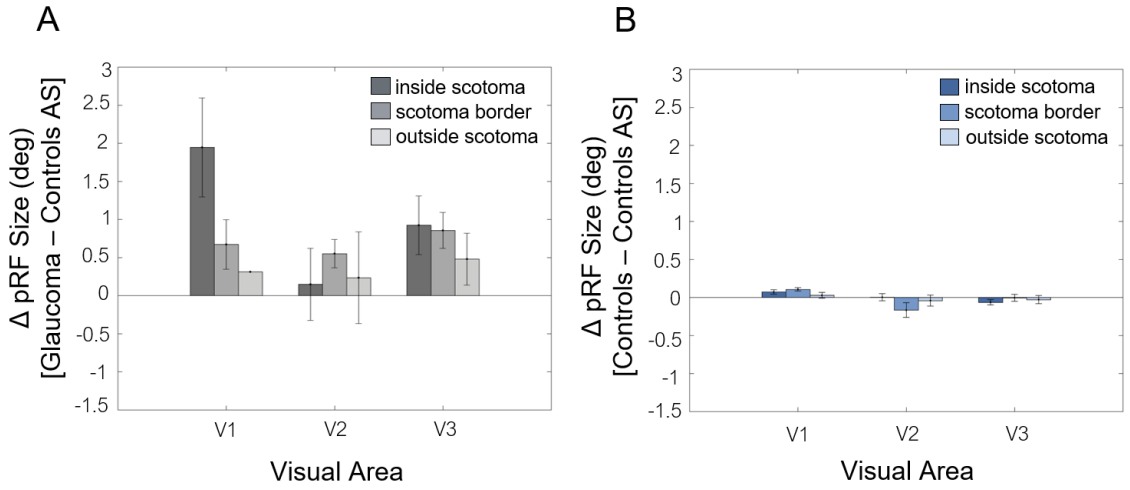


Figure 9.7: **Differences of pRF size across delineated regions of the visual field and visual areas. (A)** The difference of pRF size between between patients ($n$=5) and AS controls ($n$=5). The difference was first calculated in every eccentricity for each pair of participants and subsequently grouped across pairs. The bars represent the mean pRF size difference in each defined region of the visual field: inside (dark gray), edge (mid gray) and outside (light gray) of the scotoma in V1 to V3. The differences in pRF size between the two groups differed significantly inside, on the edge and outside of the scotoma for the early visual areas, in particular for V1. **(B)** The difference of pRF size between unmasked and masked (AS) conditions for the control group ($n$=5). The dark blue, mid blue and light blue bars represent the pRF size difference between the two conditions for pRFs located inside, at the border and outside of the scotoma, respectively. No significant pRF size differences were evident in none of the defined regions. The error bars indicate the standard error of the mean.

### 9.2.2 pRF size as a predictor of disease severity

Due to the increasing evidence of an abnormal enlargement of the pRF size in glaucoma reported in the previous sections, we tried to assess whether or not the size of the pRF could be a measure of the disease severity. Here, severity is described by means of contrast sensitivity loss across the visual field of a given glaucomatous observer. Therefore, the question can be reformulated as an attempt to investigate the dependence of the pRF size with perimetric outcomes, specifically with HFA print out values of contrast sensitivity. To address this, the MD average score was first obtained for each subject in the glaucoma population ($n$=20), that here was the average between the MD values of the left and right eye. The cumulative distribution function of the pRF size was calculated for every subject (as in section 9.2.1, Figure 9.6) and subsequently fit to a logistic function to apply a threshold at the 90% point which, by visual inspection, revealed a good distinction of the distributions. The pRF size values at the 90% point were extracted following the same order as the averaged MD values were listed, and then plotted as a function of the latter (Figure 9.8). A negative relationship between the two parameters was expected, that is higher size values assigned to lower contrast sensitivity values. However, for all the visual

areas tested the pRF size did not strongly correlate with the MD average score (Figure 9.8 and table 9.3).

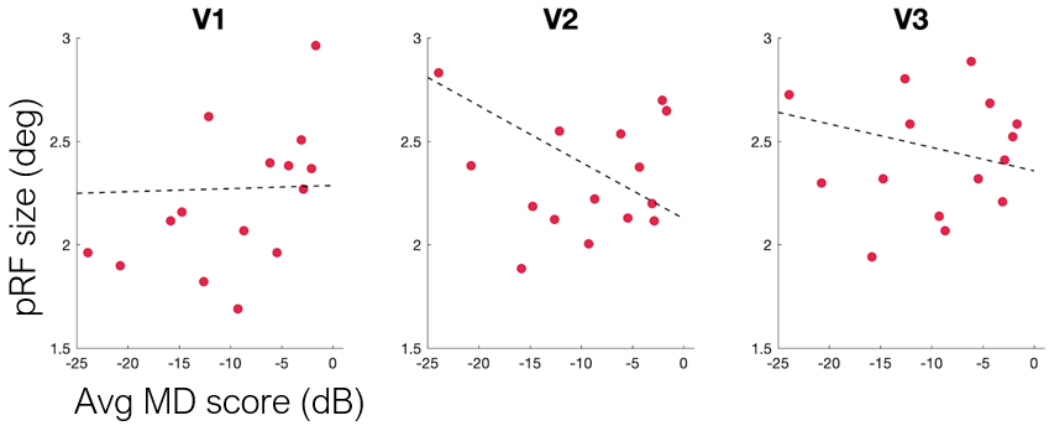


Figure 9.8: **The relationship between pRF size and ophthalmic perimetric evaluation in visual areas V1-V3.** The value of pRF size at the 90% point of the fit cumulative distribution was obtained for 20 glaucomatous subjects and subsequently plotted as a function of the subjects' mean deviation (MD) average score, measured by HFA. The latter results from averaging the MD values of the two eyes. Despite the apparent negative correlation between the two parameters in areas V1 and V2 it was neither strong nor significant (Table 9.3). The black dashed lines represent the Pearson's fit to the dots.

Table 9.3: **Statistical analysis of the relationship between pRF size and average mean deviation (MD) score in visual areas V1-V3.**

| ROI | Pearson's correlation coefficient (r) | $p$–value |
|---|---|---|
| V1 | 0.03 | 0.92 |
| V2 | -0.49 | 0.57 |
| V3 | -0.28 | 0.29 |

### 9.2.3 Position reconfiguration of pRFs in glaucoma

To test whether larger pRFs were accompanied by shifts in position, we compared the pRF center distribution as a function of distance from the fovea between patients and AS-controls across area V1. In glaucoma, the scotoma is grossly located somewhere in the peripheral visual field, due to a loss of peripheral vision. Additionally, the lesion extent varies across glaucomatous observers. Taken together, the peripheral and heterogeneous location of the scotoma among the study population, we assumed the distance of the pRF center from the fovea as a way of evaluating the displacement of the pRFs of voxels representing both the scotomatic area and neighboring regions. We employed the present described analysis case-by-case, i.e. pair-wise, to evaluate whether differences in pRF position between patients and AS controls arise from remapping as opposed to partial deafferentation.

Other than P17, the patients exhibited different distribution trends when compared to the AS-controls. However, only for P4, P10, and P12 these differences were found to be significant (two sample Kolmogorov-Smirnov test; P4: $P$=0.0466; P10: $P$=0.0011; P12: $P$=0.0168). P4 and P12 showed a trend toward clustering of pRF centers near the fovea (Figure 9.9B), which suggests reorganization. This clustering was observed within 0-2º. On the other hand, in P10 this effect was not seen as the distribution of spared V1 voxels was roughly constant across sections of the central visual field, increasing approximately around 3-4º (Figure 9.9B).

Patient P17 had fewer voxels inside and within the surroundings of the scotoma but, the overall distribution followed a similar trend to the one of the AS control (P17: $P$=0.5987). The resemblance of distributions between patient and control is probably associated with the fact that the scotoma was not captured by the stimulated area of the visual field, as one can observe in the perimetric charts on top of the respective histogram in figure 9.9B. The distribution of the pRFs in V1 of patient P18 showed a clustering near the fovea compared with AS control, but this did not reach significant level (P18: $P$=0.5886). The observed differences between these patients and the AS controls are likely related to partial deafferentation of the analysis' included voxels.

Note that even in the presence of an AS, the controls' distributions still followed a similar trend to the one in unmasked condition and, hence, to the average group distribution represented in figure 9.9A.

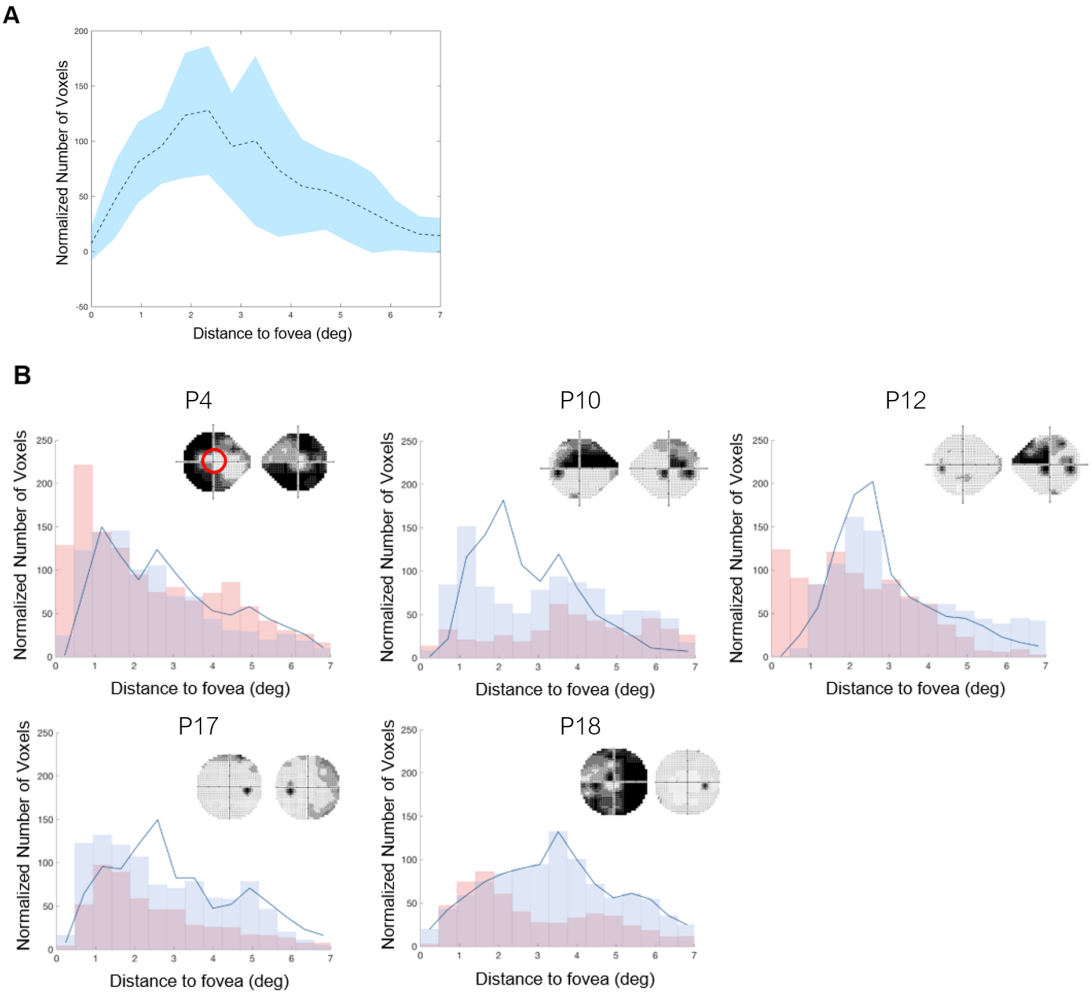


Figure 9.9: **pRF center distribution as a function of distance from the fovea. (A)** Mean distribution of the voxels as a function of the pRF center distance from the fovea in the control subjects in normal condition, i.e. without AS (represented by the black dashed line). Units are degrees of visual angle. The shaded blue area represents the standard error of the mean for the control group ($n$=5). **(B)** Histograms showing the number of voxels as a function of the pRF center distance from the fovea for patients P4, P10, P12, P17 and P18 (pink bars) and the corresponding AS-controls (blue bars). The dark blue line represents the distribution of the voxels in the control subject under full-field stimulation (i.e., without the AS). The red inset on the left perimetric grayscale plot of P4 delineates the 7-degree stimulus space. In order to adjust for V1 size, we scaled these distributions by the ratio of voxels in V1 of each patient and AS control divided by the number of V1 voxels of the controls during full-field stimulation.

## 9.3 Correspondence between visual field coverage maps and perimetric scotomas

To estimate how the visual field is represented in the primary visual cortex we used pRF- and MP-based approaches to derive visual field coverage maps (section 8.6.3). Because perimetric maps indicate the perceptual scotoma of a given glaucomatous patient,

it is of interest to determine the degree to which the visual field coverage map match perimetry outcomes, in other words if what the brains sees matched what the eyes see. The backprojections were based on V1, given that it receives the information directly from the visual pathways and processes visual information from the entire stimulus space (a hemifield per hemisphere). This way, we ensured the scotoma to be captured. The coverage maps were also produced to assess the effect of an AS in the controls. This served two goals: 1) to ensure that the patients' coverage maps were reliable and accurate (do not arise from artifacts due to pRF biases resulting from the presence of scotomas) and 2) to access neuroplasticity - differences in the backprojection maps that cannot be explained based on the incomplete visual input.

The AS controls establish the "ground truth", i.e. the backprojections of these participants should reflect the AS. Indeed, this was met because, as expected, the visual field coverage maps of V1 in AS controls grossly reveal the simulated visual field defects. Such can be observed from figure 9.10A where, based on the bilateral perimetric scores, it is suggested the dense scotoma to occupy the upper right quadrant. Accordingly, the AS control showed low sampling density in that same section of the visual field. This could be seen from the results of both pRF- and MP-based methodologies. However, MP revealed to better estimate the visual field defects, as the lowest derived activity is grossly restricted to the areas associated with the lowest sensitivity contrast (Figure 9.10C). In contrast, the visual field coverage maps of the patient revealed the presence of probes that extend well beyond the border of the scotoma, revealing a quite high sampling density inside the lesioned area (Figure 9.10C).

Figure 9.11 shows the coverage maps of P4 and respective AS control. From the perimetric measurements, represented in panel A, it is observable that the lowest sensivity values are roughly concentrated at the lower left quadrant. Accordingly, the MP coverage map revealed reduced cortical responsiveness to that same area (panel C). On the other hand, The pRF-based map showed no significant activity in approximately the entire visual field (panel B). Regarding the patient, the coverage maps (resulting from both methodologies) overlapped with the perimetric scotoma, thereby differentiating from what observed for the AS control.

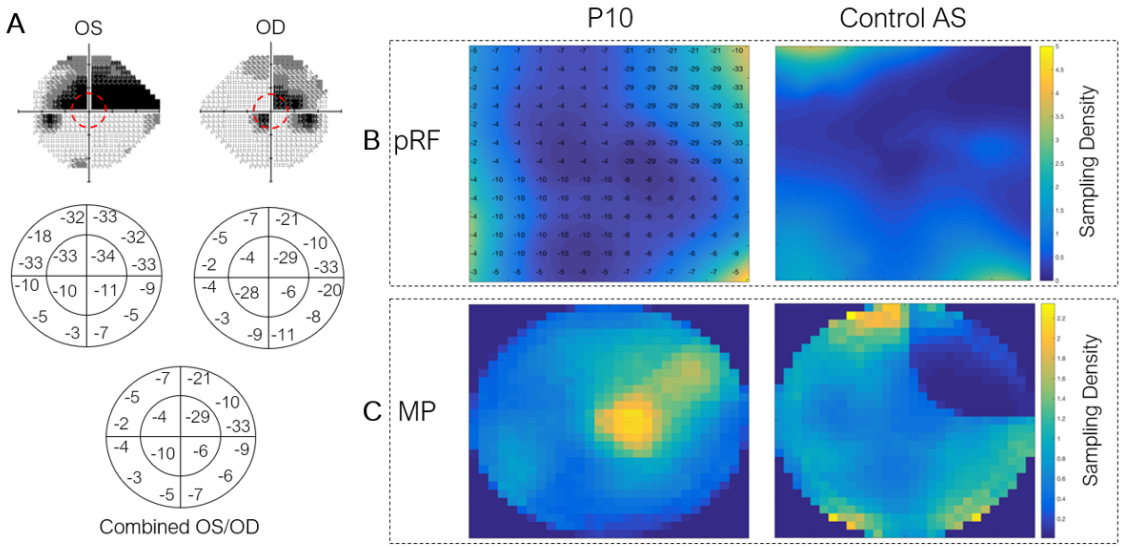


Figure 9.10: **Comparison between perimetric outcome measures and visual field coverage maps. (A)** The top panel presents the grayscale visualisation graphics of numeric contrast sensitivity (in dB), measured by HFA, of P10. Mean deviation (MD) scores of each eye are represented in the middle panel for the stimulated space of visual field (delineated on the top panel by the red insets). The inner and outer circle comprise 6 and 7 degrees of visual angle, respectively. The bottom panel gives the combined MD of the 2 eyes calculated by taking the higher contrast sensitivity value per location of the visual field. The resulted visual field coverage maps of area V1 from the pRF-based **(B)** and MP-based **(C)** methods shown for P10 and the AS-control.

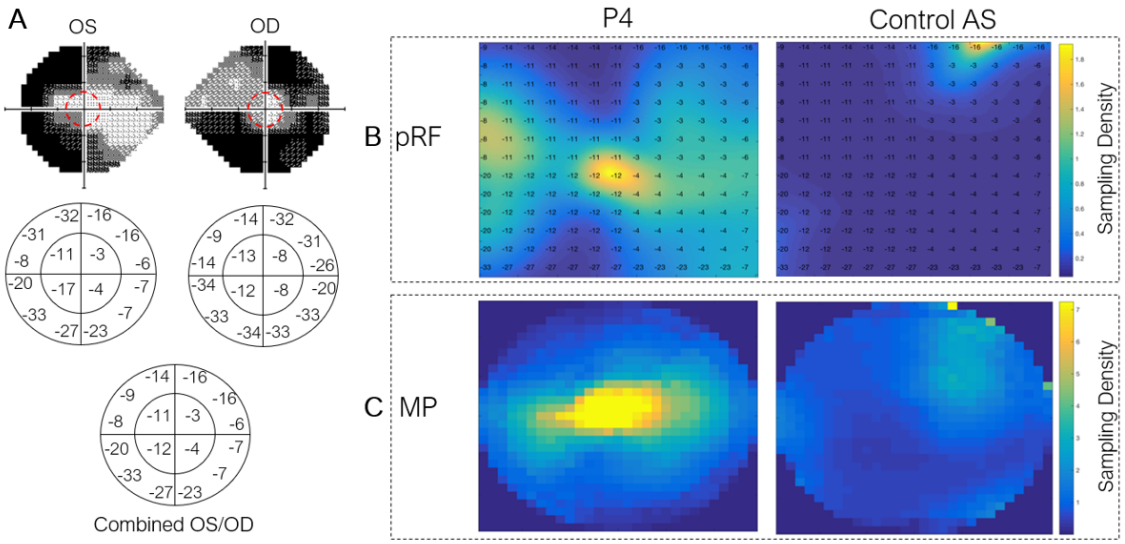


Figure 9.11: **Comparison between perimetric outcome measures and visual field coverage maps. (A)** The top panel presents the grayscale visualisation graphics of numeric contrast sensitivity (in dB), measured by HFA, of P4. Mean deviation (MD) scores of each eye are represented in the middle panel for the stimulated space of visual field (delineated on the top panel by the red insets). The inner and outer circle comprise 6 and 7 degrees of visual angle, respectively. The bottom panel gives the combined MD of the 2 eyes calculated by taking the higher contrast sensitivity value per location of the visual field. **(B)** The projection of the pRF parameters onto visual space are represented on the top panel whereas **(C)** the sampling microprobes are represented below.

Chapter 10

# Discussion

The PM of scotomas, resulting from optic neuropathy glaucoma, is of utmost clinical relevance as it may delay timely detection of the defects and thus increase chances of blindness. This perceptual phenomenon is suggested to be explained by RFs' dynamics of visual neurons, however such is rather modest and has been called into question [95]. Moreover, the precise neural basis of PM remains unknown and, furthermore, the plasticity of the visual cortex during PM has not been studied in particular. In our study we, therefore, sought to determine whether or not PM of the scotomas in glaucomatous patients provide evidence of functional reorganization of the cortex.

In summary, we used quantitative pRF analysis to study the early visual cortex of patients afflicted with POAG. We derived detailed retinotopic maps and coverage maps of the visual field for each patient and normally sighted control. The major findings are: at the vicinity of the SPZ, (i) pRFs reconfigured their preferred spatial location and (ii) exhibited an increase in size as a way to reach spared sections of the visual field. These results support the hypothesis that are functional alterations and remapping of the early visual cortex in patients with POAG, and that such changes result in the masking of the scotoma. Below we discuss our findings and interpretation in detail.

## 10.1 Overall decreased neural activity in the visual cortex of glaucoma patients

Evident from the standard deviation of the raw BOLD signal (presented as a plot in figure 9.1), the patients showed overall attenuated visual-evoked signals compared to the controls for V1-3. One could argue that the change in the magnitude of the response can be explained by reduced visual acuity. Thus, the lower signal amplitude may be an indication of a particular deficit in the parvocellular pathway as a reflection of P-cells

saturating at high-contrast levels [96]. This finding corroborates previous studies that reported a reduction in the BOLD signal in the visual cortex in glaucoma patients [2, 97].

These considerations suggest fMRI of visual brain areas, in particular changes in the BOLD signal, as a potential means for quantifying glaucomatous changes.

## 10.2 Retinotopic Remapping in the visual cortex in glaucoma

We used pRF-mapping to detail the cortical organization in V1, V2, and V3. In section 9.2 we evaluated the pRF maps of a patient. The patient's polar angle maps were normal (comparable with aged matched controls), as were the pRF size maps in the early visual area V1-3. However, the eccentricity maps of the patient showed a marked expansion of the representation of the very central visual field. Strikingly, the clinical measurements of this patient revealed visual deficits in central vision (figure 9.2). This suggests that even though the eye is apparently affected, the visual cortex is able to reallocate higher responsiveness to central vision in order to take over the defects, hence enabling perception. Moreover, the pRF maps of the control resulting from superimposition of a AS showed a loss of activity within the occipital pole when compared to normal condition, reinforcing that the abnormal patient's pRF maps cannot be explained based on the lack of visual input.

Variations of pRF size, as estimated using fMRI, are consensual to share similar trends with the RF estimates from electrophysiological studies [17, 98, 99]. Namely, RFs are known to increase as a function of eccentricity between visual field maps, but also within each visual field map. In accordance with this, we demonstrated that our quantitative pRF size estimates positively correlate with the pRF eccentricity estimates within and throughout ROIs (Figure 9.3). This was observable for both groups in every experimental condition. Therefore, we believe that the derived visual field maps, using both FF and AS stimulation, are biologically meaningful.

### 10.2.1 Rescaling and displacement of neuronal populations underly PM of scotomas in glaucoma

pRF measurements in early visual areas in the patients group exhibited unusually large pRF size estimates. When we compared the patients with a new baseline - the controls with simulated visual field defects - we found a sharper shift to the right of the cumulative percentage of pRF size across ROIs (Figure 9.6). Furthermore, such expansion effect was found to occur prominently for pRFs encompassed by the scotomatic area, decreasing as one moves towards the far periphery of the lesion (Figure 9.7B). Through size increase, pRFs located in the lesion projection zone are more likely to reach intact portions of the visual field and thus allow the scotoma to be masked with the visual features of those same portions. This is line with extrapolations mechanisms of PM.

The possibility that fixation instability would be the source of the abnormal pRF size estimates can be ruled out. Eye movements are known to be a potential source of bias to pRF estimates which may, in turn, result in increased pRF sizes [100–102]. Although eye movements were not recorded due to experimental constraints, the performed attentional task during scanning revealed that all observers were able to maintain fixation. We also discard the presence of model biases as the source for the re-scaling of the pRFs in glaucoma since the effect was not equal for inside and outside of the lesion nor across visual areas (Figure 9.7B). Furthermore, the markedly expansion of pRFs within the SPZ cannot arise from higher SNR, as the AS (gap in stimulation resulting in noisier neural signals from the artificial SPZ) revealed to have no significant impact in the controls' pRF size (Figure 9.7A). Hence, it appears that the enlargement of the neuronal populations in glaucoma is genuinely abnormal.

Alike previous studies using retinal [53] and cortical [7] scotomas, our observed pRF enlargement in V1 was accompanied by shifts in center position of neuronal populations. For 3 out of the 5 analyzed patients, pRF center distributions as a function of distance from the fovea differed significantly from that of the AS controls (Figure 9.9B). Note that the patients who shown displaced pRFs compared to the controls were the ones with larger visual field defects. Two of these patients showed a clustering of the V1 voxels along the foveal region that is in agreement to what was revealed by the cortical representations. This suggests that the presence of a scotoma results in a reweighting of the spatial response selectivity towards the scotoma neighboring areas. Thus, following the shift, pRFs are more likely to be activated by spared portions of the visual field, and can hence contribute to the spatial masking of the scotoma. The reconfiguration of the pRFs center position cannot be explained on the basis of eye movements, as fixation instability adds noise but no bias to the pRF eccentricity estimates [102].

Our explanation for the abnormal pRF estimates of size and position is that long-term reorganization of the early visual cortex has occurred in the glaucomatous patients. Literature on functional reorganization on the basis of ectopic RFs is controversial and, to the best of our knowledge, sparse in glaucoma. The study of the cortical SPZs is highly challenging in human studies because of the heterogeneity of the scotomas among individuals, e.g. variability in regard to cortical location, extension and time of onset. The question that prompts is whether the RFs changes result from an immediate response (adaptation) to the lack of visual input or are a reflection of permanent remapping. Previous electrophysiological measurements in visually deprived animals have often reported the expansion and shifts of V1 RFs within the SPZ and claimed such evidence as a manifest of cortical reorganization [7, 53, 103–106]. However, because these studies usually measure the neuronal responses only immediately after lesion and long-term (weeks to months), it is not possible to discern short- from long-term changes within the SPZ. In humans, similar findings have been found in retinal lesions, such as macular degeneration, but these are controversial. While some argue in favor of an extensive recovery within V1 SPZ, others do not [11, 107, 108]. Thus, the measures of the effects of pRFs as a result

of remapping must surpass the expected ones from short-term adaptation. The fact that the pRF enlargements and position shifts were significantly different between glaucoma patients and controls with AS simulated (thus inducing short-term adaptation) supports the view that there is a long-term reorganization in glaucoma.

Previous work in V1 injury, using fMRI and retinotopic mapping similar to our own, found larger and displaced pRFs near the border of the scotoma in the patients when compared to controls with simulated visual field defects [70]. The authors proposed the pRF changes as a way to coverage the visual field defect resulting from reorganization, which is in general agreement with our results. Individuals with macular degeneration revealed ectopic RFs, as well [11]. However, as comparable patterns were found for controls in whom lesions were mimicked, remapping was not invoked to explain the changes in the patients. The differences in the used methodologies likely contributed to the inconsistency of the results. Both we and [70] used a bar stimulus rather than rotating wedges and expanding rings, as done in [11]. In fact, it has been suggested that the bar stimuli elicits greater PM [6] which would alternatively explain the changes in pRF as a form of short-term plasticity possibly caused by various sources including feedback from higher order areas [109] and lateral connections [110]. However, this could only be the case if the pRF dynamics were the same for the controls. As such was not observed in this study, the used visual paradigm is not the origin of the unconformity of results. Additionally, how the AS was designed might also be a source of divergence. The patients studied in [11] were affected with macular degeneration, which is characterized by a loss of central vision. Thereby, a central disk was created to cover the center of the visual field of the controls. Ectopic shifts have been previously reported in artificial SPZ using these type of well-defined masks [11–13, 73]. On the other hand, the design of the AS in our study was based on the contrast sensitivity loss, measured by automated perimetry, of the patients and thus each control was presented with a different stimulus. Therefore, this might be an explanation for the lack of pRF rearrangement in the control group. However, because there is no evidence in literature of a similar induced AS, the results are not directly comparable.

### 10.2.2 Does pRF size correlate with glaucoma severity?

With regard to our results pointing to an abnormal expation of the pRFs in the patients, we then expected to find a relationship between pRF size and glaucoma severity, namely to observe an increase in pRF size as the disease stage progresses. For the sake of clarity, the term severity in the present study is defined as the extent of contrast sensitivity loss. However, there was no correlation between the pRF parameter and the visual functions measured through perimetry (Figure 9.8). Here, the focus was not on quantifying visual field severity in glaucoma and so the hypothesis was not tested further. Nevertheless, we propose that by using perimetric pattern standard deviation (SD) measures, instead of those from mean deviation, the results might yield more robust information as they

quantify irregularities in visual field defects, a desirable measure for the non-uniform vision loss in glaucoma. In fact, a previous study reported a correlation between SD scores and glaucoma severity through %BOLD changes that they found to be more attenuated at advanced stages [111]. Our results are therefore likely link to the fact that pRF estimates are mostly invariant to BOLD amplitude, thus not capturing the effect of the visual field defect. Another explanation may be that indices like SD and MD do not reflect spatial information and hence may fail to detect small and localized defects [112].

## 10.3 Visual Field Coverage Maps versus Clinical Measures

In this study, we derived visual field coverage maps of area V1 for both patients and AS-controls using pRF and MP estimates. Both approaches revealed, for the patients, an overlap of the coverage maps with the locations of the perimetric scotoma while the respective controls with simulated AS did not. This suggests that these individuals are able to fill-in the visual field defects and thus elicit a percept. In fact, to our knowledge, this is the first evidence that the visual cortex has the capability to process information that corresponds to the scotomatic region. This finding has important application for visual restoration and rehabilitation. Therefore, the use of retinotopic mapping and in particular MP reveals important characteristics of the functioning of the visual system that cannot be accessed based on the standard ophthalmic examinations tests.

To our knowledge there is no previous work describing the link between visual function measured clinically with automated perimetry and the MP approach, likely because of its novelty. Thus the performance of our method cannot be directly compared to any method rather than the other applied (pRF). The backprojection based on pRFs estimates showed not to be very precise and it is unable to map small deficits, i.e. regions assigned with low contrast sensitivity values. The steep transitions between healthy and damaged retina are known to be easily identified by pRF [12, 72], thereby contributing to its more accurate performance in these occasions. This is shown for the AS control of P10, where a whole quarter field is impaired, as described by a visual sensitivity <-20 dB which is considered an absolute scotoma [113] (figure 9.10). As such, the pRF methodology may be less suited for detection of early-stage disease in patients with slow retinal or cortical degeneration. Previous work where pRF was used for the same purpose as ours in cortical lesions [70] and in patients with choroideremia [114] reported these same pros and cons about the methodology. Here we have implemented a more advance retinotopic mapping approach, MP. Applied to the Controls AS where we know the exact extent of the scotomas (based on simulations), MP mapped with higher accuracy the functional visual field and the scotomatic region. Additional MP can also capture a decrease of contrast sensitivity rather than just functional and non-functional (blind and non-blind) visual field. These factors are easily observed in figures 9.10 and 9.11. We therefore recommend the use of MP to accurately detail the visual field coverage maps.

The neuronal responses evoked by an AS serve as a baseline to distinguish pRF changes as a result of reorganization from the ones arising from simple stimulus deprivation. However, given that partial deafferentation of the visual pathways may occur following optic nerve damage and hence, may affect pRFs corresponding to areas of the visual field other than those belonging to the scotoma, the AS control might not always be adequate. As already mentioned there is evidence that these type of stimulus manipulations might alter pRF estimates in normally sighted controls, resulting in similar changes for both patients and controls questioning whether these changes necessarily imply plasticity [12, 13, 73]. For this reason and because our results show that the visual cortex in glaucoma reconfigures the properties of neural populations in a different way than that in response to masked visual input, we assume that the patients are capable of adapting to injury through cortical reorganization.

Chapter 11

# Conclusions and Future Work

The exploratory research outlined in this thesis, in search of neuronal populations' dynamics, tried to investigate the retinotopic visual function in the early visual cortex of individuals diagnosed with glaucoma. To do this, we used luminance-contrast defined retinotopy and posterior model-based analysis by means of the pRF approach. We concluded that the glaucomatous visual system undergoes long-lasting neuroplastic changes that may not be explained by the neural circuitry operations present in healthy observers.

We measured and investigated in detail the pRF properties of location and scaled size. Results demonstrate that pRFs of voxels representing both the scotomatic area and neighboring regions are displaced and increased in size. This position shift and enlargement allows the neurons (located in the SPZ) to process information from the spared visual field, thus resulting in spatial masking of the scotoma. By means of pRF and MP measurements we also produce coverage maps of the stimulus space to put into perspective what ophthalmic examinations reveal of visual function against what the brain actually "sees" from a visual scene. Importantly, the maps in glaucomatous patients yield information on the functional properties of the visual cortex that complements the information provided by standard perimetric measurements.

Glaucoma is a disease of progressive nature which reflects on a slow loss of visual function among affected individuals. Our results are in agreement with this notion, as we demonstrate that due to functional compensation, in the form of PM, visual field defects are coverage allowing grossly normal perception in glaucomatous individuals. Nevertheless, the most striking aspect is that such a process seems to be carried by enduring changes in visual brain organization translated in the aforementioned abnormal pRFs. These observations lend support for the hypothesis that neural dysfunction is involved in glaucoma pathogenesis, contradicting the "just an eye disease" label. Thus, retinotopic fMRI combined with pRF-analysis has the potential to improve the understanding of the

pathogenesis of the disease beyond the eye and at the individual level.

In terms of clinical approaches, currently treatments that aim to lower IOP are the most common on treating the eye to prevent blindness, such as through medication or laser. However, the potential involvement of the brain and its plastic mechanisms in glaucoma suggests that rehabilitation - intensive training programs that are aimed at restoring vision - would provide a suitable strategy to complement the already existing treatments, as structural and functional changes happen at different paces. An expansion of the focus treatment would also come with tools that are able to support the diagnosis and the monitoring of the disease effects throughout the visual pathway. We have shown that MP is a promising approach to help in complementing clinical output of vision in glaucomatous patients. Combining functional brain imaging with posterior MP detailed measures would be a starting point for more robust clinical trial not only in glaucoma but in other diseases of the visual forum, as well.

## 11.1 Limitations

- **Limited number of aged-matched controls**

  First, the analyses described throughout this document included a limited number of aged-matched controls and consequently a modest population of patients for the sake of comparisons. As a result, the current findings should be considered preliminary only. The initial plan was to work with fMRI data from 20-25 individuals affected with glaucoma and that from the same (or approximate) number of well-sighted controls to form the baseline. Quite a large group of patients was formed (made of 20 individuals) however, we were unable to collect data from more than 6 controls until the end of the research internship. In addition to this, a patient had to be excluded because during the preprocessing stage we discovered that the data was distorted and could no longer be used. Although we compensated for movement artifacts during scanning due to poor results it was not possible to perform adequate alignment of functional onto anatomical data. Unfortunately, the visual field defects of this same patient were simulated on one of the controls and thus we could not perform comparison analyses taken this pair. As such, the number of individuals included was cut down to 5 on each group.

  We must then consider alternative explanations for the found ectopic pRFs rather than a long-term neuroplastic mechanism. Previous studies found that cortical feedback to superficial layers of V1 provides neurons with contextual information when not available via feedforward input [115]. Therefore, we consider plausible that the measured pRF scaling changes in areas V1 to V3 may alternatively be driven from feedback activity from extrastriate cortex. Additionally, the observed changes can also be explained by a reduction in lateral inhibition [116], i.e. depletion of the

activity of a neuron by the activity of other neurons in its vicinity, to neurons that have been silenced by the scotoma.

- **Eye movements were not recorded**

  As previously mentioned, eye movements may bias pRF estimates, commonly resulting in increased pRF sizes [100, 101]. Fixation ability is usually controlled by means of eye-tracking which was not done in the present study due to experimental constraints. Instead, eye movements were minimized by having observers performing an attention task to assure central fixation. We did find significant changes in pRF size for the patients group, however such changes were not similar between ROIs nor in- and outside of the analysed SPZ, that is an additional reason to believe that eye-movements were not an issue. However, we cannot completely exclude the possibility of eye movements as a contribution for such observations.

- **Limited visual field coverage with MRI**

  Another constraint to our results was the narrow-view stimuli. 7 degrees of visual angle (radius) were the maximum stimulated during scanning which is lower than the typical used in visual stimulation fMRI studies ($15 \times 15$ degrees). This corresponds to paracentral vision (see section 3.1) which is not enough to capture more peripheral sections of the visual field, setting a huge drawback given the notion of peripheral vision being affected first and more extensively compared to central vision in glaucoma [115, 117]. Although some of the studied patients had central scotomas, the majority presented larger visual deficits outside the stimulus space.

- **Definition of the SPZ**

  The most demanding tasks consisted of the AS design and posterior definition of the SPZ. Glaucoma is a challenging pathology to address this procedures because the visual deficits are widely variable among affected individuals. Unlike other diseases where the retinal lesions are grossly located at the same portions of the visual field, it is not straightforward to delineate a mask to mimic the defects. As a result, the posterior definition of the SPZ becomes struggling as well. The scotoma localizer experiment (section 8.3.2.3) was unable to reveal the cortical location of the scotoma. The alternative applied method - translation of perimetric dense scotoma (visual sensitivity <-13 dB) into cortical coordinates - is not the most reliable and leaves room to be improved. Indeed, by taking the pRFs that are located within these regions of the visual field, we are not defining the true SPZs as those rely on predictions that may be skewed.

- **Monocular data lacks analysis**

  In glaucoma there is usually one eye more damaged than the other. To better unravel the visual defects that are often obscured by the fellow eye, fMRI scans of monocular visual activity were acquired from patients. Due to experimental constraints it was

not possible to acquire this data from the controls and therefore make comparisons at this level which could yield significant information.

## 11.2 Future Research and Applications

Now that we have made cautious steps towards showing that retinotopic organization in the visual cortex might not be intact in glaucoma, future studies are needed to confirm the effect of this pathology in (p)RFs dynamics.

- **Complete analysis**

  First and foremost it would be ideal to complete the employed analyses for the initial 20 patients. By increasing the sample of aged-matched controls the results would achieve a statistical meaning and one could likely formulate more general findings.

- **Investigate other glaucoma typologies**

  Research on brain involvement in glaucoma has been tended to focus in high-pressure typologies of the disease, like the one we investigated - POAG. This limits the knowledge and understanding about glaucoma in general as other types, such as Normal Tension Glaucoma (NTG), may reveal different mechanisms than those unraveled so far [43]. Hereupon, it would be worth to further investigate other types of glaucoma in order to demystify whether the hint given by this study that the visual cortex reconfigures may be a commonplace feature of the disease.

- **Incorporate cortico-cortical models**

  In the previous section we suggested alternative explanations for our findings, namely the potential involvement of feedback mechanisms from extrastriate visual areas. Cortical circuitry models would be suitable to address this query. For instance connective field modeling [74] represents a solid departure as it emphasizes the spatial profile of the functional connectivity between visual areas and gives insight about information flow. Moreover, as it is a stimulus-independent analysis, it avoids complications associated with stimulus-driven pRF approach.

- **Layer-specific plasticity**

  Measuring cortical reorganization at a finer scale might reveal changes that, at a coarser scale, are masked. With the advances in ultra-high field functional MRI, we now have the tool to examine the human brain at a mesoscale *in-vivo*. This enable us to assess potential cortical reorganization across cortical depth, to measure the flow of information across different cortical laminae. Therefore, it would be of interest to repeat the present study using 7T- or higher field-fMRI to investigate the proposed plasticity in area V1 at the level of its feedforward/input layers. In other words,

to test whether following the visual field defect, the ability of V1 to reorganize is layer-specific.

- **Incorporate effect size to coverage maps**

  Regarding the methodologies used in the presented research, in section 8.6.3 we presented visual field coverage maps that enable the access to what the brain "sees". By incorporating effect size to the back projection of the pRF/MP estimates could upgrade the methodology as to statistically quantify the differences between the map of a patient and that of a healthy control.

- **Explore relationship between ophthalmic examinations and pRF characteristics**

  In section 9.2.2 we showed that we did not find a correlation between pRF size and disease severity inferred from perimetry outcome values, however, the pitfalls of such analysis were not investigated in detail nor improved as it was out of the scope of our research question. Therefore, it would be of interest to explore deeper the relationship between pRF and clinical measurements, not only perimetry but the whole battery of ophthalmic tests collected (e.g., OCT and IOP) thereby testing whether pRF is able to guess disease progression.

- **Apply more advanced pRF methodologies**

  Finally, future studies could apply more advanced pRF based models to improve the reliability of the estimates. The Bayesian pRF, for example, gives for each characteristic of the model not only the best fitting value but a full posterior distribution as well [90]. This serves several needs: a) it indicates the uncertainty associated with each estimate, which is of great importance when a visual field defect is present, as higher uncertainty will most likely be associated with model biases; b) it facilitates the statistical analysis, and c) it allows one to incorporate additional biological knowledge by providing prior information, e.g., that density of cortical neurons is higher in the fovea than in the periphery . In combination, the above referred three factors improve the interpretability of pRF.

# Bibliography


[1] Y.-C. Tham, X. Li, T.-Y. Wong, H. Quigley, T. Aung, and C.-y. Cheng. "Global Prevalence of Glaucoma and Projections of Glaucoma Burden through 2040 A Systematic Review and Meta-Analysis." In: *Ophthalmology* 121 (June 2014). DOI: 10.1016/j.ophtha.2014.05.013.

[2] V. Borges, H. V Danesh-Meyer, J. Black, and B. Thompson. "Functional effects of unilateral open-angle glaucoma on the primary and extrastriate visual cortex." In: *Journal of vision* 15 (Nov. 2015), p. 9. DOI: 10.1167/15.15.9.

[3] C. Li, P. Cai, L. Shi, Y. Lin, J. Zhang, S. Liu, B. Xie, Y. Shi, H. Yang, S. Li, H. Du, and J. Wang. "Voxel-based Morphometry of the Visual-related Cortex in Primary Open Angle Glaucoma." In: *Current eye research* 37 (May 2012), pp. 794–802. DOI: 10.3109/02713683.2012.683506.

[4] L. Yu, B. Xie, X. Yin, M. Liang, A. Evans, J. Wang, and C. Dai. "Reduced Cortical Thickness in Primary Open-Angle Glaucoma and Its Relationship to the Retinal Nerve Fiber Layer Thickness." In: *PloS one* 8 (Sept. 2013), e73208. DOI: 10.1371/journal.pone.0073208.

[5] W. Chen-Wei, N. Wang, S. Cai, Z. Fang, M. Yu, Q. Wu, L. Tang, B. Guo, Y. Feng, J. Jonas, X. Chen, X. Liu, and Q. Gong. "Structural Brain Abnormalities in Patients with Primary Open-Angle Glaucoma: A Study with 3T MR Imaging." In: *Investigative ophthalmology visual science* 54 (Dec. 2012). DOI: 10.1167/iovs.12-9893.

[6] H. Komatsu. "The neural mechanisms of perceptual filling-in." In: *Nature reviews. Neuroscience* 7 (Apr. 2006), pp. 220–31. DOI: 10.1038/nrn1869.

[7] M Pettet and C. Gilbert. "Dynamic changes in receptive-field size in cat primary visual cortex." In: *Proceedings of the National Academy of Sciences of the United States of America* 89 (Oct. 1992), pp. 8366–70. DOI: 10.1073/pnas.89.17.8366.

[8] E. Schumacher, J. Jacko, S. Primo, K. Main, K. Moloney, E. Kinzel, and J. Ginn. "Reorganization of visual processing is related to eccentric viewing in patients with macular degeneration." In: *Restorative neurology and neuroscience* 26 (Feb. 2008), pp. 391–402.

[9] C. Gilbert and T. Wiesel. "Receptive field dynamics in adult primary cortex." In: *Nature* 356 (Apr. 1992), pp. 150–2. DOI: 10.1038/356150a0.

[10] D. Dilks, C. Baker, E. Peli, and N. Kanwisher. "Reorganization of Visual Processing in Macular Degeneration Is Not Specific to the "Preferred Retinal Locus"." In: *The Journal of neuroscience : the official journal of the Society for Neuroscience* 29 (Apr. 2009), pp. 2768–73. DOI: 10.1523/JNEUROSCI.5258-08.2009.

[11] H. Baseler, A. Gouws, K. Haak, C. Racey, M. D Crossland, A. Tufail, G. Rubin, F. Cornelissen, and A. Morland. "Large-scale remapping of visual cortex is absent in adult humans with macular degeneration." In: *Nature neuroscience* 14 (Mar. 2011), pp. 649–55. DOI: 10.1038/nn.2793.

[12] K. Haak, F. Cornelissen, and A. Morland. "Population Receptive Field Dynamics in Human Visual Cortex." In: *PloS one* 7 (May 2012), e37686. DOI: 10.1371/journal.pone.0037686.

[13] A. Papanikolaou, G. Keliris, S. Lee, N. Logothetis, and S. Smirnakis. "Nonlinear population receptive field changes in human area V5/MT+ of healthy subjects with simulated visual field scotomas." In: *NeuroImage* 120 (July 2015). DOI: 10.1016/j.neuroimage.2015.06.085.

[14] A. Smith. "Estimating Receptive Field Size from fMRI Data in Human Striate and Extrastriate Visual Cortex." In: *Cerebral Cortex* 11 (Dec. 2001), pp. 1182–1190. DOI: 10.1093/cercor/11.12.1182.

[15] S. Engel, G. Glover, and B. Wandell. "Retinotopic organization in human visual cortex and the spatial precision of functional MRI." In: *Cerebral cortex (New York, N.Y. : 1991)* 7 (Apr. 1997), pp. 181–92. DOI: 10.1093/cercor/7.2.181.

[16] M Sereno, A. Dale, J Reppas, K Kwong, J Belliveau, T. Brady, B. Rosen, and R. Tootell. "Borders of multiple visual areas in humans revealed by functional magnetic resonance imaging." In: *Science (New York, N.Y.)* 268 (June 1995), pp. 889–93. DOI: 10.1126/science.7754376.

[17] S. Dumoulin and B. Wandell. "Population receptive field estimates in human visual cortex." In: *NeuroImage* 39 (Feb. 2008), pp. 647–60. DOI: 10.1016/j.neuroimage.2007.09.034.

[18] S. Ferreira, A. Pereira, B. Quendera, A. Reis, E. Silva, and M. Castelo-Branco. "Primary visual cortical remapping in patients with inherited peripheral retinal degeneration." In: *NeuroImage: Clinical* 13 (Dec. 2016), 428–438. DOI: 10.1016/j.nicl.2016.12.013.

[19] L. Levin, S. Nilsson, J. Hoeve, S. Wu, P. Kaufman, and A. Alm. *Adler's Physiology of the Eye: Expert Consult - Online and Print*. Adler's Physiology of the Eye. Elsevier Health Sciences, 2011. ISBN: 9780323057141. URL: https://books.google.pt/books?id=1oIlvnXnJvEC.

[20] M. J. Tovée. "The organisation of the visual system." In: *An Introduction to the Visual System*. 2nd ed. Cambridge University Press, 2008, 62–77. DOI: 10.1017/CBO9780511801556.004.

[21] F. Gaillard. *Globe (illustration)*. URL: http://radiopaedia.org/cases/globe-illustration.

[22] J. Zhu, E. Zhang, and K. Rio-Tsonis. "Eye Anatomy." In: Nov. 2012. ISBN: 0470016175. DOI: 10.1002/9780470015902.a0000108.pub2.

[23] E. Callaway. "Structure and function of parallel pathways in the primate early visual system." In: *The Journal of physiology* 566 (Aug. 2005), pp. 13–9. DOI: 10.1113/jphysiol.2005.088047.

[24] V. Ramachandran. "Filling in Gaps in Perception: Part I." In: *Current Directions in Psychological Science - CURR DIRECTIONS PSYCHOL SCI* 1 (Dec. 1992), pp. 199–205. DOI: 10.1111/1467-9566.ep10770411.

[25] S. Hofer, A. Karaus, and J. Frahm. "Reconstruction and Dissection of the Entire Human Visual Pathway Using Diffusion Tensor MRI." In: *Frontiers in neuroanatomy* 4 (Apr. 2010), p. 15. DOI: 10.3389/fnana.2010.00015.

[26] E. Kandel, J. Schwartz, T. Jessell, S. Siegelbaum, and A Hudspeth. *Principles of Neural Science, Fifth Edition*. Jan. 2013. ISBN: 9780071390118.

[27] B. Wandell, S. Dumoulin, and A. Brewer. "Visual Field Maps in Human Cortex." In: *Neuron* 56 (Nov. 2007), pp. 366–83. DOI: 10.1016/j.neuron.2007.10.012.

[28] B. Wandell and S. Smirnakis. "Plasticity and stability of visual field maps in adult primary visual cortex." In: *Nature reviews. Neuroscience* 10 (Nov. 2009), pp. 873–84. DOI: 10.1038/nrn2741.

[29] D. Essen, C. Anderson, and D. Felleman. "Information processing in the primate visual system: An integrated systems perspective." In: *Science (New York, N.Y.)* 255 (Feb. 1992), pp. 419–23. DOI: 10.1126/science.1734518.

[30] R. Tootell, J. Mendola, N. Hadjikhani, P. J. Ledden, A. K. Liu, J. B. Reppas, M. I. Sereno, and A. Dale. "Functional Analysis of V3A and Related Areas in Human Visual Cortex." In: *The Journal of neuroscience : the official journal of the Society for Neuroscience* 17 (Oct. 1997), pp. 7060–78. DOI: 10.1523/JNEUROSCI.17-18-07060.1997.

[31] D. Perrett, M. Oram, M Harries, R Bevan, J. Hietanen, P Benson, and S Thomas. "Viewer-centred and object-centred coding of heads in the macaque temporal cortex." In: *Experimental brain research. Experimentelle Hirnforschung. Expérimentation cérébrale* 86 (Feb. 1991), pp. 159–73. DOI: 10.1007/BF00231050.

[32] H. Kafaligonul. "Vision: A Systems Neuroscience Perspective." In: *The Journal of Neurobehavioral Sciences* 2 (Jan. 2014), p. 1. DOI: 10.5455/JNBS.1395935766.

[33] D. Hubel and T. Wiesel. "Receptive fields of cells in striate cortex of very young, visually inexperienced kittens." In: *Journal of neurophysiology* 26 (Dec. 1963), pp. 994–1002. DOI: 10.1152/jn.1963.26.6.994.

[34] D. Whitteridge and P. Daniel. "The Representation of the Visual Field on the Calcarine Cortex." In: Jan. 1961, pp. 222–228. ISBN: 978-3-662-22222-5. DOI: 10.1007/978-3-662-22221-8_29.

[35] S. Dumoulin. "Functional MRI of the Visual System." In: Sept. 2015, pp. 429–471. DOI: 10.1007/978-1-4899-7591-1_15.

[36] J. Ma, N. Fan, and N. Wang. "Normal Visual Field." In: Jan. 2019, pp. 43–48. ISBN: 978-981-13-2501-4. DOI: 10.1007/978-981-13-2502-1_9.

[37] *Category:Visual fields - Wikimedia Commons*. URL: https://commons.wikimedia.org/wiki/Category:Visual_fields.

[38] R. Weinreb, T. Aung, and F. Medeiros. "The Pathophysiology and Treatment of Glaucoma A Review." In: *JAMA : the journal of the American Medical Association* 311 (May 2014), pp. 1901–11. DOI: 10.1001/jama.2014.3192.

[39] M. Emanuel. *Types of Glaucoma*. URL: http://www.glaucomaassociates.com/glaucoma/types-of-glaucoma/.

[40] R. Weinreb, C. Leung, J. Crowston, F. Medeiros, D. Friedman, J. Wiggs, and K. Martin. "Primary open-angle glaucoma." In: *Nature reviews. Disease primers* 2 (Sept. 2016), p. 16067. DOI: 10.1038/nrdp.2016.67.

[41] *Eye Disease Simulations*. URL: https://nei.nih.gov/health/examples.

[42] D. Prins, S. Hanekamp, and F. Cornelissen. "Structural brain MRI studies in eye diseases: Are they clinically relevant? A review of current findings." In: *Acta Ophthalmologica* 94 (Sept. 2015). DOI: 10.1111/aos.12825.

[43] C. Boucard, S. Hanekamp, B. Curcic-Blake, M. Ida, M. Yoshida, and F. Cornelissen. "Neurodegeneration beyond the primary visual pathways in a population with a high incidence of normal-pressure glaucoma." In: *Ophthalmic and Physiological Optics* 36 (May 2016), pp. 344–353. DOI: 10.1111/opo.12297.

[44] A. Zikou, G Kitsos, L. Tzarouchi, L. Astrakas, G. Alexiou, and M Argyropoulou. "Voxel-Based Morphometry and Diffusion Tensor Imaging of the Optic Pathway in Primary Open-Angle Glaucoma: A Preliminary Study." In: *AJNR. American journal of neuroradiology* 33 (Nov. 2011), pp. 128–34. DOI: 10.3174/ajnr.A2714.

[45] H. Brown, R. Woodall, R. Kitching, H. Baseler, and A. Morland. "Using magnetic resonance imaging to assess visual deficits." In: *Ophthalmic and physiological optics* (May 2016).

[46] R. Nuzzi, L. Dallorto, and T. Rolle. "Changes of Visual Pathway and Brain Connectivity in Glaucoma: A Systematic Review." In: *Frontiers in Neuroscience* 12 (May 2018), p. 363. DOI: 10.3389/fnins.2018.00363.

[47] R. Mastropasqua, L. Agnifili, P. Mattei, M. Caulo, V. Fasanella, R. Navarra, L. Mastropasqua, and G. Marchini. "Advanced Morphological and Functional Magnetic Resonance Techniques in Glaucoma." In: *BioMed Research International* 2015 (July 2015), pp. 1–7. DOI: 10.1155/2015/160454.

[48] N. Gupta and Y. Yucel. "What Changes Can We Expect in the Brain of Glaucoma Patients?" In: *Survey of ophthalmology* 52 Suppl 2 (Dec. 2007), S122–6. DOI: 10.1016/j.survophthal.2007.08.006.

[49] P. Frezzotti, A. Giorgio, I. Motolese, A. De Leucio, M. Iester, E. Motolese, A. Federico, and N. De Stefano. "Structural and Functional Brain Changes beyond Visual System in Patients with Advanced Glaucoma." In: *PloS one* 9 (Aug. 2014), e105931. DOI: 10.1371/journal.pone.0105931.

[50] A. Pascual-Leone, A. Amedi, F. Fregni, and L. Merabet. "The plastic human brain." In: *Annual review of neuroscience* 28 (Feb. 2005), pp. 377–401. DOI: 10.1146/annurev.neuro.27.070203.144216.

[51] D. Buonomano and M. Merzenich. "Cortical Plasticity: From Synapses to Maps." In: *Annual review of neuroscience* 21 (Mar. 1998), pp. 149–86. DOI: 10.1146/annurev.neuro.21.1.149.

[52] J Sebastian Espinosa and M. Stryker. "Development and Plasticity of the Primary Visual Cortex." In: *Neuron* 75 (July 2012), pp. 230–49. DOI: 10.1016/j.neuron.2012.06.009.

[53] C. Gilbert and T. N. Wiesel. "Receptive field dynamics in adult primary cortex." In: *Nature* 356 (Apr. 1992), pp. 150–2. DOI: 10.1038/356150a0.

[54] Y. Chino. "Adult plasticity in the visual system." In: *Canadian journal of physiology and pharmacology* 73 (Oct. 1995), pp. 1323–38. DOI: 10.1139/y95-187.

[55] J H Kaas, L. Krubitzer, Y. Chino, A. Langston, E H Polley, and N Blair. "Reorganization of Retinotopic Cortical Maps in Adult Mammals After Lesions of the Retina." In: *Science (New York, N.Y.)* 248 (May 1990), pp. 229–31. DOI: 10.1126/science.2326637.

[56] K. Haak, A. Morland, and S. Engel. "Plasticity, and Its Limits, in Adult Human Primary Visual Cortex." In: *Multisensory research* 28 (Apr. 2015), pp. 297–307. DOI: 10.1163/22134808-00002496.

[57] B. Wandell and S. Smirnakis. "Plasticity and stability of visual field maps in adult primary visual cortex." In: *Nature reviews. Neuroscience* 10 (Nov. 2009), pp. 873–84. DOI: 10.1038/nrn2741.

[58] R. Weil and G. Rees. "A new taxonomy for perceptual filling-in." In: *Brain research reviews* 67 (Nov. 2010), pp. 40–55. DOI: 10.1016/j.brainresrev.2010.10.004.

[59] F. Kingdom and B. Moulden. "Border effects on brightness: A review of findings, models and issues." In: *Spatial vision* 3 (Feb. 1988), pp. 225–62. DOI: 10.1163/156856888X00140.

[60] P. De Weerd, R. Gattass, R. Desimone, and L. G. Ungerleider. "Responses of cells in monkey visual cortex during perceptual filling-in of an artificial scotoma." In: *Nature* 377 (Nov. 1995), pp. 731–4. DOI: 10.1038/377731a0.

[61] M. Meng, D. Remus, and F. Tong. "Filling-in of Visual Phantoms in the Human Brain." In: *Nature neuroscience* 8 (Oct. 2005), pp. 1248–54. DOI: 10.1038/nn1518.

[62] Y. Sasaki and T. Watanabe. "The primary visual cortex fills in color." In: *Proceedings of the National Academy of Sciences of the United States of America* 101 (Sept. 2005), pp. 18251–6. DOI: 10.1073/pnas.0406293102.

[63] E. Amaro and G. Barker. "Study design in MRI: Basic principles." In: *Brain and Cognition* 60 (May 2006), pp. 220 –232. DOI: 10.1016/j.bandc.2005.11.009.

[64] A.-L Lin and H.-Y Way. "Functional Magnetic Resonance Imaging." In: Dec. 2014, pp. 4005–4018. ISBN: 9780123864574. DOI: 10.1016/B978-0-12-386456-7.07610-3.

[65] M. Cohen. "Parametric Analysis of fMRI Data Using Linear Systems Methods." In: *NeuroImage* 6 (Sept. 1997), pp. 93–103. DOI: 10.1006/nimg.1997.0278.

[66] G. Boynton, S. Engel, G. Glover, and D. Heeger. "Linear Systems Analysis of Functional Magnetic Resonance Imaging in Human V1." In: *J. Neurosci.* 16 (Jan. 1998). DOI: 10.1523/JNEUROSCI.16-13-04207.1996.

[67] S. Dumoulin. "Functional MRI of the Visual System." In: Sept. 2015, pp. 429–471. DOI: 10.1007/978-1-4899-7591-1_15.

[68] S. Engel, D. E. Rumelhart, B. Wandell, A. T. Lee, G. H. Glover, E. Chichilnisky, and M. Shadlen. "FMRI of human visual cortex." In: *Nature* 369 (July 1994), p. 525. DOI: 10.1038/369525a0.

[69] A. Brewer and B. Barton. "Visual Field Map Organization in Human Visual Cortex." In: Sept. 2012, pp. 29–60. ISBN: 978-953-51-0760-6. DOI: 10.5772/51914.

[70] A. Papanikolaou, G. Keliris, D. Papageorgiou, Y. Shao, E. Krapp, E. Papageorgiou, K. Štingl, A. Bruckmann, U. Schiefer, N. Logothetis, and S. Smirnakis. "Population receptive field analysis of the primary visual cortex complements perimetry in patients with homonymous visual field defects." In: *Proceedings of the National Academy of Sciences of the United States of America* 111 (Apr. 2014). DOI: 10.1073/pnas.1317074111.

[71] B. Barton and A. Brewer. "fMRI of the rod scotoma elucidates cortical rod pathways and implications for lesion measurements." In: *Proceedings of the National Academy of Sciences* early online edition (Apr. 2015). DOI: 10.1073/pnas.1423673112.

[72] M. Senden. "Real Time pRF Mapping Real Time Estimation of Population Receptive Fields Using Gradient Descent 2." In: (Sept. 2017). DOI: 10.1101/194621.

[73] P. Binda, J. Thomas, G. Boynton, and I. Fine. "Minimizing biases in estimating the reorganization of human visual areas with BOLD retinotopic mapping." In: *Journal of vision* 13 (June 2013). DOI: 10.1167/13.7.13.

[74] K. Haak, J. Winawer, B. M Harvey, R. Renken, S. Dumoulin, B. Wandell, and F. Cornelissen. "Connective Field Modeling." In: *NeuroImage* 66 (Oct. 2012). DOI: 10.1016/j.neuroimage.2012.10.037.

[75] M. Hoffmann, F. Kaule, N. Levin, Y. Masuda, A. Kumar, I. Gottlob, H. Horiguchi, R. Dougherty, J. Stadler, B. Wolynski, O. Speck, M. Kanowski, Y. Liao, B. Wandell, and S. Dumoulin. "Plasticity and Stability of the Visual System in Human Achiasma." In: *Neuron* 75 (Aug. 2012), pp. 393–401. DOI: 10.1016/j.neuron.2012.05.026.

[76] A. Fracasso, Y. Koenraads, G. Porro, and S. Dumoulin. "Bilateral population receptive fields in congenital hemihydranencephaly." In: *Ophthalmic and Physiological Optics* 36 (May 2016), pp. 324–334. DOI: 10.1111/opo.12294.

[77] K. Ahmadi, A. Fracasso, J. van Dijk, C. Kruijt, M. Genderen, S. Dumoulin, and M. Hoffmann. "Altered organization of the visual cortex in FHONDA syndrome." In: *NeuroImage* 190 (Mar. 2018). DOI: 10.1016/j.neuroimage.2018.02.053.

[78] S. Clavagnier, S. Dumoulin, and R. Hess. "Is the Cortical Deficit in Amblyopia Due to Reduced Cortical Magnification, Loss of Neural Resolution, or Neural Disorganization?" In: *Journal of Neuroscience* 35 (Nov. 2015), pp. 14740–14755. DOI: 10.1523/JNEUROSCI.1101-15.2015.

[79] D Schwarzkopf, E. Anderson, B. Haas, S. White, and G. Rees. "Larger Extrastriate Population Receptive Fields in Autism Spectrum Disorders." In: *The Journal of neuroscience : the official journal of the Society for Neuroscience* 34 (Feb. 2014), pp. 2713–24. DOI: 10.1523/JNEUROSCI.4416-13.2014.

[80] E. Anderson, M. Tibber, D. Schwarzkopf, S. Shergill, E. Fernandez-Egea, G. Rees, and S. Dakin. "Visual Population Receptive Fields in People with Schizophrenia Have Reduced Inhibitory Surrounds." In: *The Journal of Neuroscience* 37 (Dec. 2016), pp. 3620–15. DOI: 10.1523/JNEUROSCI.3620-15.2016.

[81] In: *Terminology and guidelines for glaucoma*. PubliComm, 2014.

[82] D. Pelli. "The VideoToolbox software for visual psychophysics: Transforming numbers into movies." In: *Spatial Vision* 10 (Feb. 1997), pp. 437–442. DOI: 10.1163/156856897X00366.

[83] D. Brainard. "The Psychophyics Toolbox." In: *Spatial vision* 10 (Feb. 1997), pp. 433–6. DOI: 10.1163/156856897X00357.

[84] J Talairach and G Szikla. "Application of Stereotactic Concepts to the Surgery of Epilepsy." In: *Acta neurochirurgica. Supplementum* 30 (Feb. 1980), pp. 35–54. DOI: 10.1007/978-3-7091-8592-6_5.

[85] A. Dale, B. Fischl, and M. Sereno. "Cortical surface-based analysis: I. Segmentation and surface reconstruction." In: *NeuroImage* 9 (Mar. 1999), pp. 179–94. DOI: 10.1006/nimg.1998.0395.

[86] P. Yushkevich, J. Piven, H. Cody, R. Smith, S. Ho, J. Gee, and G. Gerig. "Yushkevich PA, Piven J, Hazlett HC, Smith RG, Ho S, Gee JC, Gerig GUser-guided 3D active contour segmentation of anatomical structures: significantly improved efficiency and reliability. Neuroimage 31:1116-1128." In: *NeuroImage* 31 (Aug. 2006), pp. 1116–28. DOI: 10.1016/j.neuroimage.2006.01.015.

[87] B. Wandell, S. Chial, and B. Backus. "Visualization and Measurement of the Cortical Surface." In: *Journal of cognitive neuroscience* 12 (Oct. 2000), pp. 739–52. DOI: 10.1162/089892900562561.

[88] O. Nestares and D Heeger. "Robust multiresolution alignment of MRI brain volumes." In: *Magnetic resonance in medicine : official journal of the Society of Magnetic Resonance in Medicine / Society of Magnetic Resonance in Medicine* 43 (June 2000), pp. 705–15.

[89] J. Carvalho, A. Invernizzi, K. Ahmadi, M. Hoffmann, R. Renken, and F. Cornelissen. "Micro-probing enables high-resolution mapping of neuronal subpopulations using fMRI." In: (July 2019). DOI: 10.1101/709006.

[90] P. Zeidman, E. Silson, D. Schwarzkopf, C. Baker, and W. Penny. "Bayesian Population Receptive Field Modelling." In: *NeuroImage* 180 (Dec. 2016). DOI: 10.1016/j.neuroimage.2017.09.008.

[91] B. Dow, A. Snyder, R. Vautin, and R Bauer. "Magnification factor and receptive field size in foveal striate cortex of monkey." In: *Experimental brain research. Experimentelle Hirnforschung. Expérimentation cérébrale* 44 (Feb. 1981), pp. 213–28. DOI: 10.1007/BF00237343.

[92] R. Duncan and G. Boynton. "Cortical Magnification within Human Primary Visual Cortex Correlates with Acuity Thresholds." In: *Neuron* 38 (June 2003), pp. 659–71. DOI: 10.1016/S0896-6273(03)00265-4.

[93] B. Harvey and S. Dumoulin. "The Relationship between Cortical Magnification Factor and Population Receptive Field Size in Human Visual Cortex: Constancies in Cortical Architecture." In: *The Journal of neuroscience : the official journal of the Society for Neuroscience* 31 (Sept. 2011), pp. 13604–12. DOI: 10.1523/JNEUROSCI.2572-11.2011.

[94] D. Hubel and T. Wiesel. "Uniformity of monkey striate cortex: A parallel relationship between field size, scatter, and magnification factor." In: *The Journal of Comparative Neurology* 158 (Dec. 1974), pp. 295 –305. DOI: 10.1002/cne.901580305.

[95] B. Wandell. "Plasticity and stability of visual field maps in adult primary visual cortex." In: (Feb. 2013).

[96] R. Hess, X. Li, G. Lu, B. Thompson, and B. Hansen. "The contrast dependence of the cortical fMRI deficit in amblyopia; a selective loss at higher contrasts." In: *Human brain mapping* 31 (Jan. 2009), pp. 1233–48. DOI: 10.1002/hbm.20931.

[97] R. Duncan, P. Sample, R. Weinreb, C. Bowd, and L. Zangwill. "Retinotopic Organization of Primary Visual Cortex in Glaucoma: Comparing fMRI Measurements of Cortical Function with Visual Field Loss." In: *Progress in retinal and eye research* 26 (Feb. 2007), pp. 38–56. DOI: 10.1016/j.preteyeres.2006.10.001.

[98] K. Kay, T. Naselaris, R. J Prenger, and J. Gallant. "Identifying natural images from human brain activity." In: *Nature* 452 (Apr. 2008), pp. 352–5. DOI: 10.1038/nature06713.

[99] A. Fracasso, N. Petridou, and S. Dumoulin. "Systematic variation of population receptive field properties across cortical depth in human visual cortex." In: *NeuroImage* 139 (July 2016). DOI: 10.1016/j.neuroimage.2016.06.048.

[100] B. Klein, B. Harvey, and S. Dumoulin. "Attraction of Position Preference by Spatial Attention throughout Human Visual Cortex." In: *Neuron* 84 (Sept. 2014). DOI: 10.1016/j.neuron.2014.08.047.

[101] A. Hummer, M. Ritter, M. Tik, A. Ledolter, M. Woletz, G. Holder, S. Dumoulin, U. Schmidt-Erfurth, and C. Windischberger. "Eyetracker-based gaze correction for robust mapping of population receptive fields." In: *NeuroImage* 142 (July 2016). DOI: 10.1016/j.neuroimage.2016.07.003.

[102] N. Levin, S. Dumoulin, J. Winawer, R. Dougherty, and B. Wandell. "Cortical Maps and White Matter Tracts following Long Period of Visual Deprivation and Retinal Image Restoration." In: *Neuron* 65 (Jan. 2010), pp. 21–31. DOI: 10.1016/j.neuron.2009.12.006.

[103] M. Calford, Y. Chino, A. Das, U. Eysel, C. Gilbert, S. Heinen, J. Kaas, and S. Ullman. "Neuroscience - Rewiring the adult brain." In: *Nature* 438 (Dec. 2005), E3; discussion E3–4. DOI: 10.1038/nature04359.

[104] S. Heinen and A. Skavenski. "Recovery of visual responses in foveal V1 neurons following bilateral foveal lesions in adult monkey." In: *Experimental brain research. Experimentelle Hirnforschung. Expérimentation cérébrale* 83 (Feb. 1991), pp. 670–4. DOI: 10.1007/BF00229845.

[105] C. Darian-Smith and C. Gilbert. "Axonal sprouting accompanies functional reorganization in adult cat striate cortex." In: *Nature* 368 (May 1994), pp. 737–40. DOI: 10.1038/368737a0.

[106] D. Giannikopoulos and U. Eysel. "Dynamics and specificity of cortical map reorganization after retinal lesions." In: *Proceedings of the National Academy of Sciences of the United States of America* 103 (Aug. 2006), pp. 10805–10. DOI: 10.1073/pnas.0604539103.

[107] C. Baker, E. Peli, N. Knouf, and N. Kanwisher. "Reorganization of Visual Processing in Macular Degeneration." In: *The Journal of neuroscience : the official journal of the Society for Neuroscience* 25 (Feb. 2005), pp. 614–8. DOI: 10.1523/JNEUROSCI.3476-04.2005.

[108] H. Baseler, A. Brewer, L. Sharpe, A. Morland, H. Jägle, and B. Wandell. "Reorganization of human cortical maps caused by inherited photoreceptor abnormalities." In: *Nature neuroscience* 5 (May 2002), pp. 364–70. DOI: 10.1038/nn817.

[109] M. Williams, C. Baker, H. Op de Beeck, W. Shim, T. Dang, and N. Kanwisher. "Feedback of visual object information to foveal retinotopic cortex. Nature Neuroscience, 11, 1439-1445." In: *Nature Neuroscience* (Jan. 2008).

[110] J Lund. "Anatomical Organization Of Macaque Monkey Striate Visual Cortex." In: *Annual review of neuroscience* 11 (Feb. 1988), pp. 253–88. DOI: 10.1146/annurev.ne.11.030188.001345.

[111] W. Zhou, E. Muir, K. Nagi, S. Chalfin, P. Rodriguez, and T. Duong. "Retinotopic fMRI Reveals Visual Dysfunction and Functional Reorganization in the Visual Cortex of Mild to Moderate Glaucoma Patients." In: *Journal of Glaucoma* 26 (Feb. 2017), p. 1. DOI: 10.1097/IJG.0000000000000641.

[112] Kucur, G. Holló, and R. Sznitman. "A deep learning approach to automatic detection of early glaucoma from visual fields." In: *PLOS ONE* 13 (Nov. 2018), e0206081. DOI: 10.1371/journal.pone.0206081.

[113] E. Vesti. "Essential Perimetry. The Field Analyzer Primer." In: *Acta Ophthalmologica Scandinavica* 81 (Mar. 2003), pp. 98 –98. DOI: 10.1034/j.1600-0420.2003.00011.x.

[114] E. Silson, T. Aleman, A. Willett, L. Serrano, D. Pearson, A. Rauschecker, A. Maguire, C. Baker, J. Bennett, and M. Ashtari. "Comparing Clinical Perimetry and Population Receptive Field Measures in Patients with Choroideremia." In: *Investigative Opthalmology Visual Science* 59 (July 2018), p. 3249. DOI: 10.1167/iovs.18-23929.

[115] A. Morgan, L. Petro, and L. Muckli. "Cortical feedback to superficial layers of V1 contains predictive scene information." In: Jan. 2018. DOI: 10.32470/CCN.2018.1083-0.

[116] C. Gilbert and T. Wiesel. "Morphology and intracortical projections of functionally identified neurons in cat visual cortex." In: *Nature* 280 (Jan. 1979).

[117] S Laquis, P. Chaudhary, and S. Sharma. "The patterns of retinal ganglion cell death in hypertensive eyes." In: *Brain research* 784 (Mar. 1998), pp. 100–4. DOI: 10.1016/S0006-8993(97)01189-X.

[118] N. Bolas. "Basic MRI principles." In: Sept. 2016, pp. 1–37. DOI: 10.1002/9781118786574.ch1.

[119] M. Puddephat. *3 Magnetic Resonance Imaging | PhD | Mike Puddephat*. URL: https://www.mikepuddephat.com/pages/149/3-magnetic-resonance-imaging.

[120] P. Jezzard, P. Matthews, and S. Smith. *Functional magnetic resonance imaging: An introduction to methods*. Jan. 2012, pp. 1–426. DOI: 10.1093/acprof:oso/9780192630711.001.0001.

[121] W. Hendee and C. Morgan. "Magnetic resonance imaging. Part I: Physical principles." In: *The Western journal of medicine* 141 (Nov. 1984), pp. 491–500.

[122] *T1 differences*. URL: http://www.revisemri.com/images/t1differences.gif.

[123] *T2 differences*. URL: http://www.revisemri.com/images/t2differences.gif.

[124] M. Monti. "Statistical Analysis of fMRI Time-Series: A Critical Review of the GLM Approach." In: *Frontiers in human neuroscience* 5 (Mar. 2011), p. 28. DOI: 10.3389/fnhum.2011.00028.

Appendix A

# Supplementary Material

This appendix contains the derived retinotopic- and coverage maps of the visual field that are not presented in the main document.

## A.1 Visual Field Maps

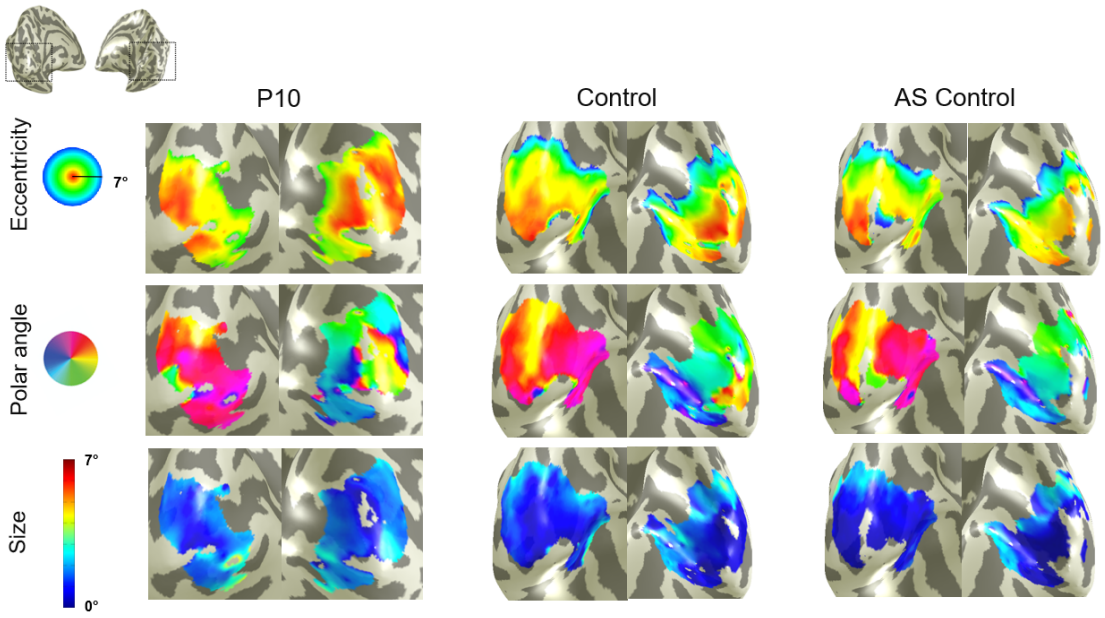


Figure A.1: **Visualization of VFM based estimates using pRF for a P10 and the age-matched control obtained with a luminance-contrast defined stimuli.**

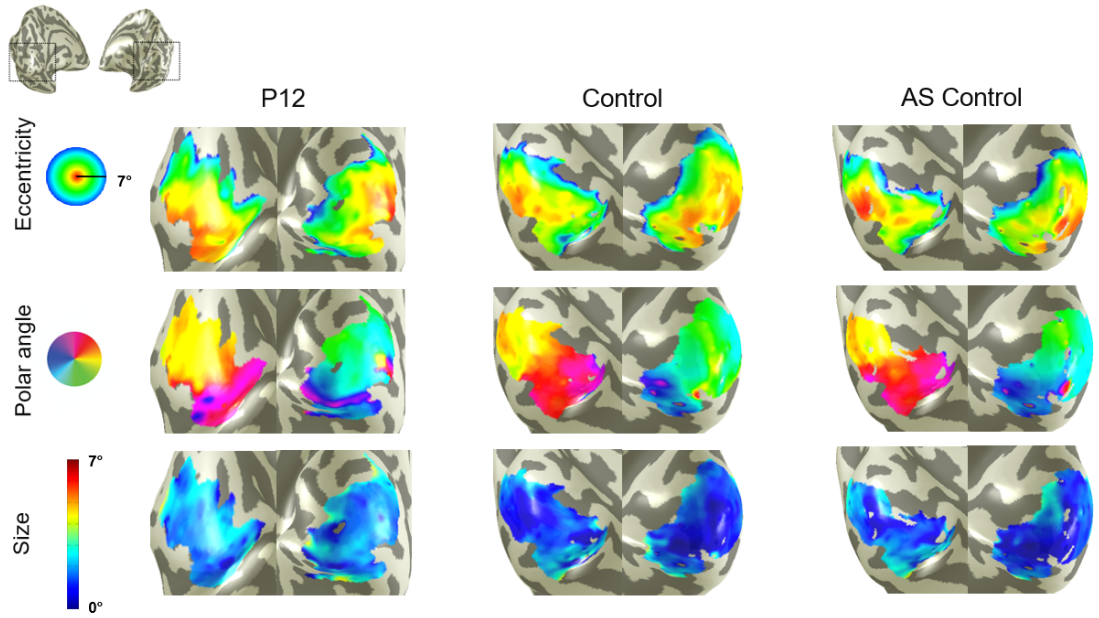


Figure A.2: **Visualization of VFM based estimates using pRF for a P12 and the age-matched control obtained with a luminance-contrast defined stimuli.**

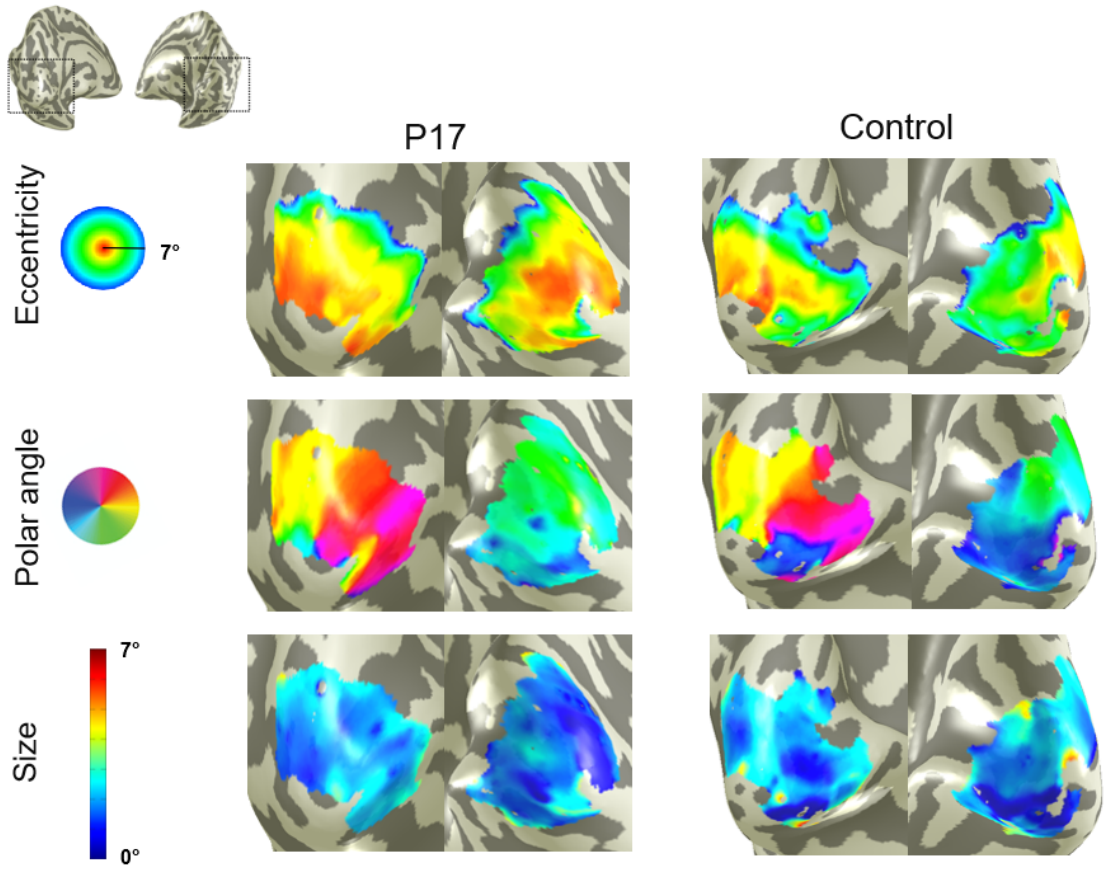


Figure A.3: **Visualization of VFM based estimates using pRF for a P17 and the age-matched control obtained with a luminance-contrast defined stimuli.**

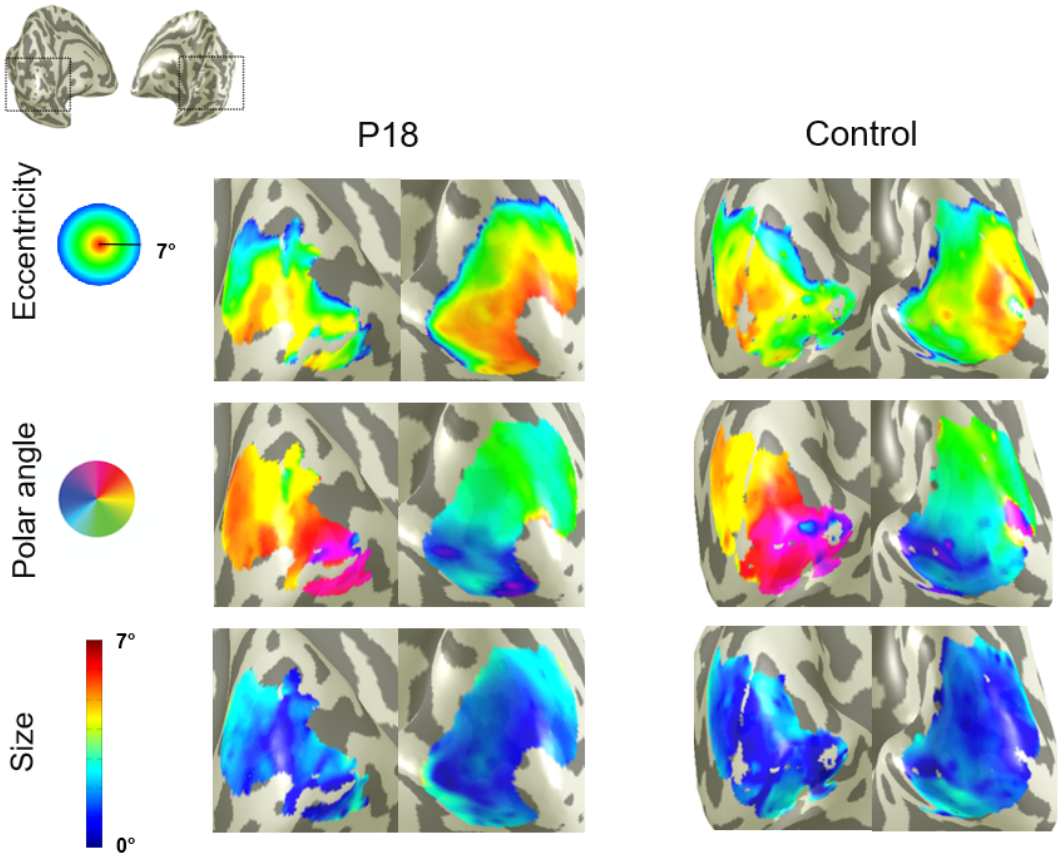


Figure A.4: **Visualization of VFM based estimates using pRF for a P18 and the age-matched control obtained with a luminance-contrast defined stimuli.**

## A.2 Visual Field Coverage Maps

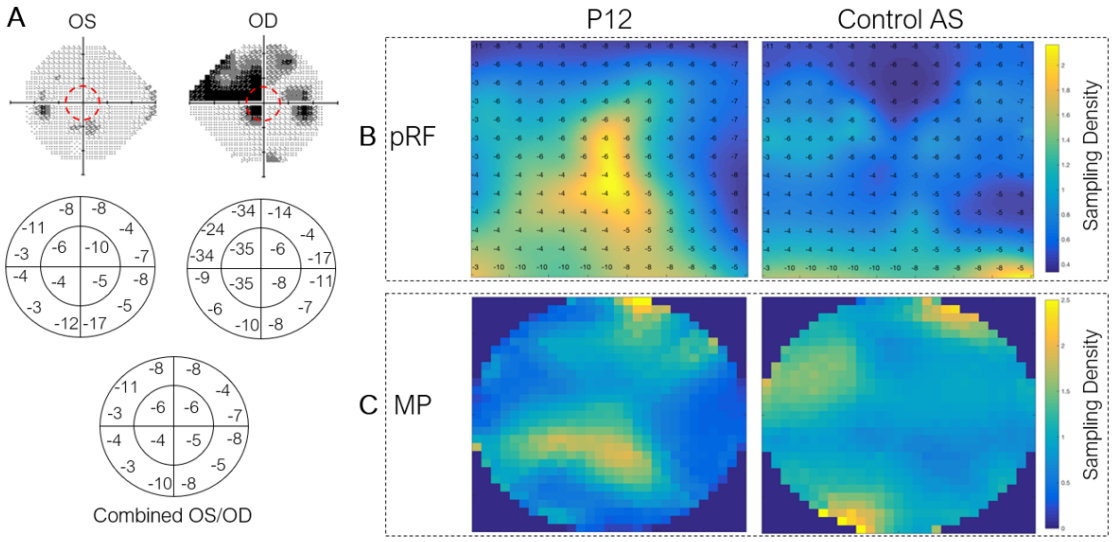


Figure A.5: **Comparison between perimetric outcome measures and visual field coverage maps of P12 and aged-matched control.**

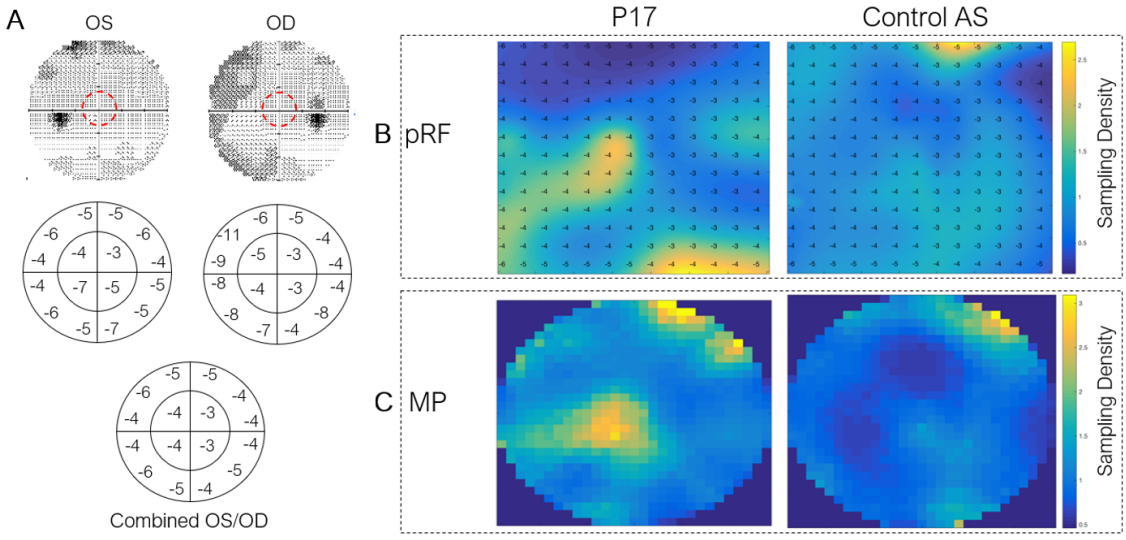


Figure A.6: **Comparison between perimetric outcome measures and visual field coverage maps of P17 and aged-matched control.**

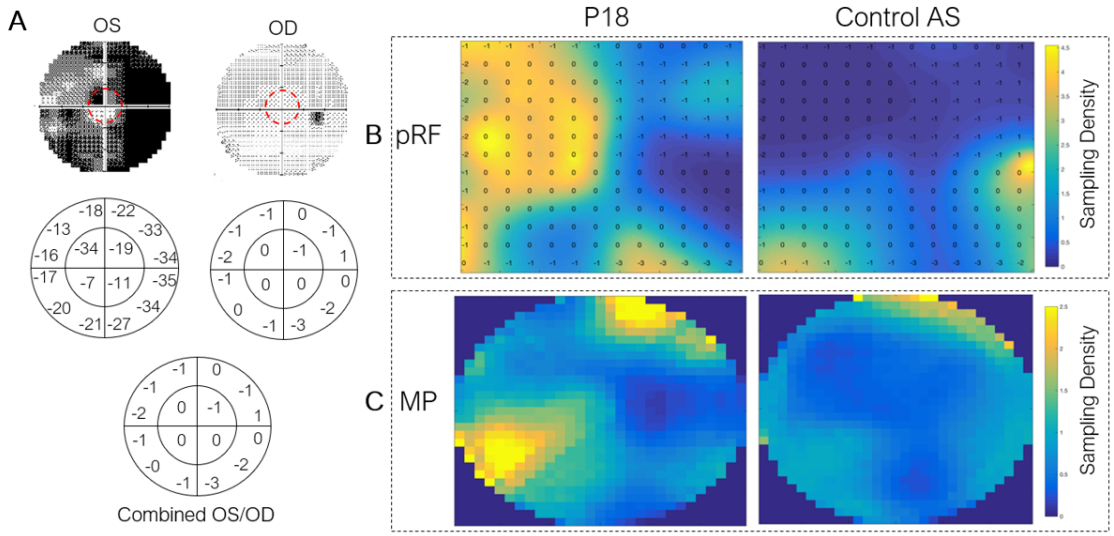


Figure A.7: **Comparison between perimetric outcome measures and visual field coverage maps of P18 and aged-matched control.**

ANNEX I

# Magnetic Resonance Imaging Principles

MRI is a non-invasive technique primarily used in medical imaging that provides the access to the anatomy and physiological processes of the human body. It enables detailed images of the inside of the body with a high spatial resolution and excellent contrast of the soft tissues.

When certain nuclei, such as protons, are subjected to an external magnetic field, $B_0$, due to their intrinsic magnetic moment, $\mu$, they rotate at a specific frequency, proportional to the field strength, which results in an angular momentum, the spin. This phenomenon establishes the key focus of MRI. Hydrogen is the most commonly used nuclei for this purpose due to high sensitivity and presence in water and fat, both of which are very abundant in biological tissues. In MRI systems, $B_0$ is produced by the presence of a superconductive magnet inside the scanner where the subject to be imaged is positioned [118].

In the absence of an external magnetic field protons rotate randomly, and so the net value of the magnetization is null (Figure I.1A.1). However, when a magnetic field is applied, there is a tendency for protons to align either parallel or antiparallel to the direction of the field - polarization (Figure I.1A.2). Because hydrogen nuclei are composed by a single proton which, in turn, has spin ½, spins can occupy two distinct energy levels, high and low. The division of the degenerate energy level is responsible for the two possible directions of alignment, due to the Zeeman effect. Nuclei in the high-energy level align antiparallel to $B_0$ whereas nuclei in the low-energy level align parallelly to $B_0$. Based on the Boltzmann distribution, a larger population of protons occupy the lower state and, therefore, the resulting net magnetization vector, $M$, points towards the direction of the field (Figure I.1C) [118]. *M precesses* around the field axis with a specific frequency, $\omega_0$, known as *Larmor Frequency*, which is directly proportional to the strength of $B_0$ (Figure I.1B). The basis of magnetic resonance (MR) is then described by

the following equation:

$$\omega_0 = \gamma B_0 \tag{I.1}$$

where $\gamma$ is a constant called the gyromagnetic ratio which differs among nuclei and is commonly expressed in units of megahertz per tesla. For hydrogen the gyromagnetic ratio is $42.58 MHz/T$ [118]. It tells how fast a particular nucleus will precess when a determined magnetic field is applied.

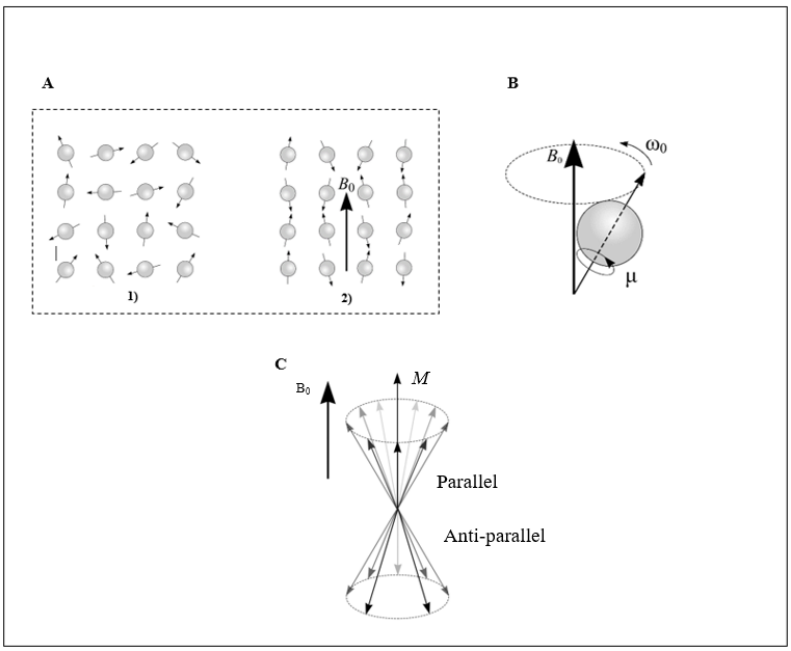


Figure I.1: **MRI physics. (A)** (1) In the absence of an external magnetic field the magnetic moments (solid arrows) of the protons are randomly organized. (2) Following the application of a strong external magnetic field ($B_0$), the magnetic moments orient themselves either parallel or antiparallel to the direction of the field. **(B)** The magnetic moment of each proton, $\mu$, precess around $B_0$ at a specific frequency proportional to the field, $\omega_0$, known as Larmor Frequency. The movement of precession describes a cone surface. **(C)** The summing over the magnetic moments gives a bulk magnetization vector, $M$, that points towards the direction of $B_0$ due to a larger proportion of protons aligned parallel to the field. Adapted from. Adapted from [119].

In order to acquire a signal, nuclei must transit between the high- and low-energy states. This is induced by an external source of energy, a radio frequency (RF) pulse which must be applied orthogonally to $B_0$ and at a frequency matching $\omega_0$ for resonance to occur [120].

At equilibrium, $M$ only has $z$ component as it lies along the direction of the main magnetic field, this is called the equilibrium magnetization ($M_0$) (Figure I.2A). In this configuration, there is no transverse magnetization, i.e. component of magnetization in the $xy$ plane. When applying the RF pulse, the equilibrium magnetization is disturbed, the longitudinal component, $M_z$, is reduced from its original value $M_0$ and the transversal

component, $M_{xy}$, becomes nonzero (Figure I.2A). When this is done, all the individual nuclei become synchronized, precessing together at a given angle that depends on the duration and intensity of the pulse. When the RF pulse ceases, the nuclei slowly return to the original state, i.e. relax, and $M$ is realigned with the main magnetic field.

The change rate of $M$ with time is described by a set of equations known as the Bloch equations. During the return to equilibrium, upon application of a 90º RF pulse, these equations become,

$$M_z(t) = M_0(1 - e^{-\frac{t}{T_1}}) \tag{I.2}$$

$$M_{xy}(t) = M_{xy}(0)(e^{-\frac{t}{T_2}}) \tag{I.3}$$

where $t$ is the time following the RF pulse and $T_1$ and $T_2$ correspond to the longitudinal and transverse relaxation times, respectively. $T_1$, also known as spin-lattice relaxation time, governs the rate of recovery of the magnetization along the direction of $B_0$ that reflects on the time required for $M_z$ to recover 63% of the thermal equilibrium value ($M_0$) (Figure I.2B.1). $T_2$, or spin-spin relaxation time, represents the relaxation along the plane orthogonal to $B_0$, which is defined by the time taken for $M_{xy}$ to decay down to 37% of its initial value, $M_{xy}(0)$ (Figure I.2B.2). Both relaxation processes occur simultaneously with the restriction being that $T_2$ is always less or equal to $T_1$.

The transverse relaxation results from a loss of synchronization of the nuclei after the RF pulse stops and is attributed to two factors. First, it relates to the transfer of energy from one nucleus to another, leading the concerned spins to dephase from the remainings in the system. This makes the main contribution to $T_2$, reason why this time constant is often called spin-spin relaxation time as mentioned previously. Second, it arises from variations in the strength of the magnetic field that can be due to hardware limitations (e.g., imperfect uniformity of the main magnet) and differences in magnetic susceptibility between different tissues. The combination of both causes promote a faster dephasing of the spins, with a rate of $T_2^*$ (pronounced T-two-star). The relationship between $T_2$ from spins interactions and that from field inhomogeneities, $T_2'$, is described as follows

$$\frac{1}{T_2^*} = \frac{1}{T_2} + \frac{1}{T_2'} \tag{I.4}$$

Faraday's Law of Induction states that a changing magnetic field induces an electric current in a conductor. Based on this principle, the magnetization oscillating in the transverse plane ($M_{xy}$), that follows the application of the 90º pulse, can then be detected in the presence of a coil in the MRI scanner. The induced voltage in the coil, the magnetic resonance (MR) signal, is known as the free induction decay (FID). FID, as the name suggests, does not persist throughout time. Due to the dephasing of the transverse components of magnetization, that results from both field inhomogeneities and $T_2$ intrinsic

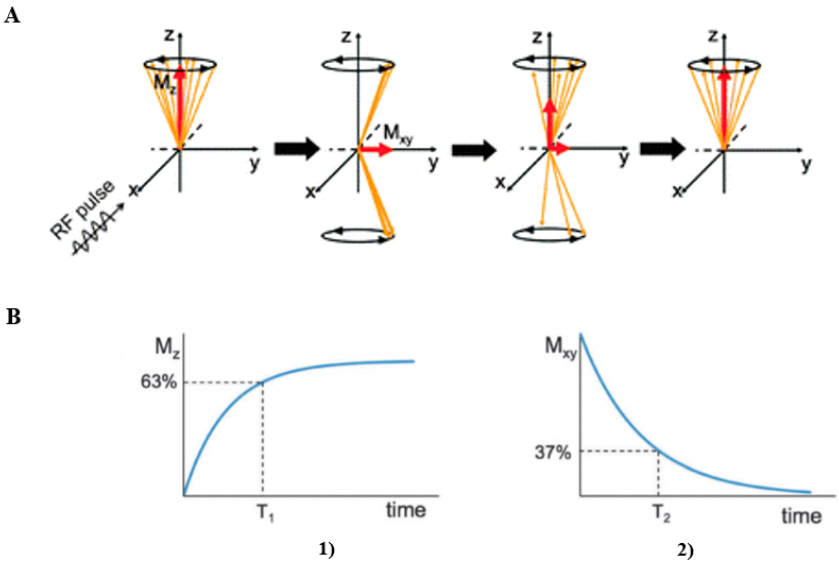


Figure I.2: **Application of radio frequency pulse (RF) and relaxation times. (A)** Under the influence of a RF pulse, the net magnetization is projected to the transverse place, resulting in a decrease of the longitudinal magnetization ($M_z$) and thereby generation of transverse magnetization ($M_{xy}$). After cessation of the RF pulse, the nuclear spins return to their original state, a process referred to as relaxation. **(B)** Longitudinal and transverse relaxation are described by $T_1$ and $T_2$ respectively. 1) $T_1$ refers to the time necessary for $M_z$ to recover 63% of its initial value. 2) T2 is the time required for $M_{xy}$ to drop 37% of its original magnitude. Note that the $x$ axis for the plots 1) and 2) are not the same because $T_1$ is longer than $T_2$. Adapted from [3].

mechanisms, FID decays with $T_2^*$ characteristics. Pulse sequences have been devised to refocus the detectable magnetization created by the 90º RF pulse and measure the resulting signal.

## I.1 Pulse sequence

MRI is a versatile imaging technique in the sense that different types of images can be obtained depending on what one desires to see. To this end, there are a variety of used schemes in which the excitation of the tissue and the reading of the signal are specifically programmed. This assembly is described in the so-called *pulse sequence*. Pulse sequences are then differentiated regarding the number, strength and timing of the pulses [121].

The main parameters of a given pulse sequence are the repetition time (TR) and the echo time (TE). TR corresponds to the time between two consecutive RF pulses. For a given nucleus in a given environment, TR determines how much of the longitudinal magnetization is recovered and hence controls the amount of $T_1$ relaxation. TE refers to the time that elapses since an RF pulse is applied until a signal, an "echo", is detected. It determines to what extent the transverse magnetization decays. Therefore, TE controls the amount of $T_2$ relaxation.

## I.2 Image Contrast

The timing parameters that characterize a pulse sequence, TR and TE, are adjustable and provide the main means whereby the contrast on the MR image can be manipulated to emphasize certain tissues.

The contrast mechanisms in MRI are based on three different tissue-specific properties: $T_1$, $T_2$ and Proton Density (PD).

When the image contrast depends on $T_1$ it is said to be $T_1$ weighted ($T_1$w). T1w images are obtained by controlling the interplay between TR and T1. By selecting a long TR, tissues with different T1 values have enough time to recover their net magnetization vector and consequently their signals are not dramatically different, which means low contrast (Figure I.3A). On the other hand, a short TR allows less time for the magnetization to recover and hence signal difference between two tissues become more noticeable (Figure I.3A).

To obtain $T_2$ weighted ($T_2$w) images, TE is the parameter to take into consideration. When TE is made short, the transverse magnetization of the tissues has not enough time to recover, resulting in poor differentiation of the tissues (Figure I.3B). However, by setting a long TE value, the complete transverse relaxation is enabled and thus, the relative difference between the $T_2$-decay of each tissue is more discernible (Figure I.3B).

Lastly, PD weighted (PDw) images result from a mixture of $T_1$- and $T_2$-weighting mechanisms. If TR is long and TE is short both $T_1$ and $T_2$ effects are cut down. When this combination of parameters is set, quantifying the density of protons present in a specific tissue becomes the dominant weighting for image contrast.

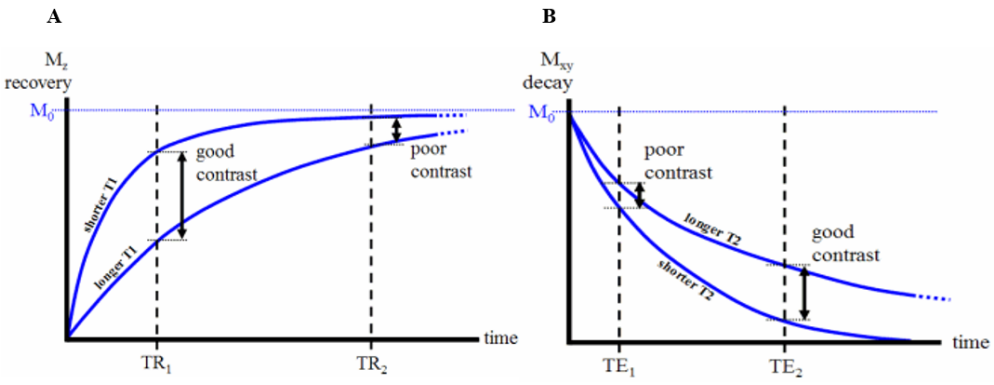


Figure I.3: **The importance of correctly setting repetition time and echo time to obtain T1 and T2 weighted images. (A)** $T_1$ weighted tissues with different $T_1$ relaxation times. **(B)** $T_2$ weighted tissues with different $T_2$ relaxation times. Adapted from [122, 123]

ANNEX II

# The General Linear Model

The conventional goal of fMRI data analysis is to determine which voxels have a time course that changes following experimental manipulation. In task-based fMRI this is usually done by applying the General Linear Model, or GLM, the most widely used technique for fMRI data analysis.

At its core, the GLM approach is a way of modelling a given data set in terms of one or more *predictor variables*, also called *regressors*. The predictor variables consist of a series of values assumed to be known, representing patterns that are expected to be found in the data. Being fundamentally a linear model, the GLM scales all regressors and add them together in order to compute the "best fitting" for the data. The weighted sum of regressors (or fitted model) is assigned with an error term that basically reflects how "far" it is from the measured signal. This difference is known as the *residual error* and is assumed to be independent and random, following a Gaussian distribution with null mean. In equation form the GLM can be expressed as:

$$Y = X\beta + \epsilon \tag{II.1}$$

where $Y$ is the data, or dependent variable, $X$ is the so-called *design matrix* which collects all the regressors together, $\beta$ reflects the relative contribution of each regressor and $\epsilon$ features the residual errors.

In fMRI the GLM analysis is performed on a voxel-by-voxel basis, which means that for each separate analysis, the dependent variable is the series of acquisition values from a different voxel. Additionally, the spatial covariance between neighboring voxels is ignored, i.e., the signals from one voxel are assumed to be independent of one another [124]. The data to be modelled is typically the BOLD time series and the regressors are usually a set of predicted responses patterns to manipulations or experimental conditions. This analysis also includes regressors of non-interest, or nuisance regressors, which arise

from experimental factors such as motion and signals drifts. The aim of the analysis is to estimate if, and to what extent, each regressor contributes to the variability observed on the voxel's time series. The amplitude of the BOLD signal at each observation ($y_i$) can then be expressed as the sum of one or more known predictors ($x_1 \cdots x_p$) each multiplied by an unknown weighting factor ($\beta_1 \cdots \beta_p$), plus error term ($\epsilon_i$). Hence, a set of equations is produced:

$$\begin{aligned} y_1 &= x_{1,1}\beta_1 + x_{1,2}\beta_2 + \cdots + x_{1,p}\beta_p + \epsilon_1 \\ y_2 &= x_{2,1}\beta_1 + x_{2,2}\beta_2 + \cdots + x_{2,p}\beta_p + \epsilon_2 \\ &\cdots \\ y_n &= x_{n,1}\beta_1 + x_{n,2}\beta_2 + \cdots + x_{n,p}\beta_p + \epsilon_n \end{aligned} \tag{II.2}$$

Using matrix notation, the GLM can be condensed into its simplest formulation (see equation II.1) in which $Y$ and $\epsilon$ are $n \times 1$ column vectors, $X$ is the design matrix of dimension $n_p$, and $\beta$ is a $1 \times p$ vector.